

2. EXPLANATORY NOTES¹

Shipboard Scientific Party²

INTRODUCTION

In this chapter we describe the shipboard procedures used during Leg 197. This information concerns only shipboard operations and analyses described in the site chapters of the *Initial Reports* volume of the Leg 197 *Proceedings of the Ocean Drilling Program*. Methods used by various investigators for shore-based analyses of Leg 197 data will be described in the individual scientific contributions to be published in the Leg 197 *Scientific Results* volume and elsewhere.

Authorship

The leg summary chapter and separate sections of the site chapters were written by the following shipboard scientists (authors are listed in alphabetical order; no seniority is implied).

Leg Summary: Bob Duncan, John Tarduno

Background and Objectives: Bob Duncan, Dave Scholl, John Tarduno

Operations: Ron Grout

Lithostratigraphy: Rosalba Bonaccorsi, Sten Lindblom

Biostratigraphy: Bill Siesser, Fabrizio Tremolada

Igneous Petrology: Fred Frey, Jill Gudding, Schichun Huang, Randy Keller, Clive Neal, Marcel Regelous, Sidonie Revillon, Pat Thompson, Thor Thordarson

Alteration and Weathering: Sidonie Revillon

Paleomagnetism: Claire Carvallo, Rory Cottrell, Masayuki Torii

Physical Properties: Sarah Haggas, Bryan Kerr, Bernhard Steinberger

Downhole Measurements: Arno Buysch, Florence Einaudi, Johannes Stoll

Underway and Site Geophysics: Bryan Kerr, Dave Scholl

¹Examples of how to reference the whole or part of this volume.

²Shipboard Scientific Party addresses.

The “Core Descriptions” directories for each site include summary core descriptions (“barrel sheets”), core photographs, and thin section descriptions (see the “Core Descriptions” contents list.)

Shipboard Scientific Procedures

Numbering of Sites, Holes, Cores, and Samples

Ocean Drilling Program (ODP) drill sites are numbered consecutively, and each site consists of one or more holes drilled while the ship was positioned over one acoustic beacon. For all ODP drill sites, a letter suffix distinguishes individual holes drilled at the same site. The first hole drilled is assigned the site number modified by the suffix A, the second hole takes the site number and suffix B, and so forth. Note that this procedure differs slightly from that used by the Deep Sea Drilling Project (Sites 1 through 624) but prevents ambiguity between site- and hole-number designations. It is important to distinguish among holes drilled at a site because sediment or rocks recovered from different holes usually do not come from exactly equivalent positions in the stratigraphic column.

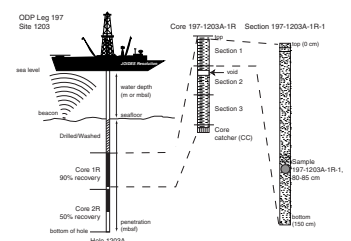
The cored interval is measured in meters below seafloor. The depth interval assigned to an individual core begins with the depth below the seafloor at which the coring began and extends to the depth that the coring ended. Each coring interval is generally ≤ 9.5 m, which is the length of a core barrel. Coring intervals may be shorter and may not necessarily be adjacent if separated by drilled intervals that are not cored. A center bit may replace the core barrel if it is decided to drill without coring.

Cores taken from a hole are numbered sequentially from the top of the hole downward. Core numbers and their associated cored intervals in meters below seafloor are unique in a given hole. Normally, maximum recovery for a single core is 9.5 m of rock or sediment contained in a plastic liner (6.6 cm internal diameter) plus ~ 0.2 m (without a plastic liner) in the core catcher (Fig. F1). The core catcher is a device at the bottom of the core barrel that prevents the core from falling out when the barrel is being retrieved from the hole. In certain situations recovery may exceed the 9.5-m maximum. In hard rock cores, this probably happens when a pedestal of rock fails to break off and thus is not caught by the core catcher. When a subsequent core barrel is deployed, this pedestal enters the core barrel and, because it is from the previous cored interval, it can lead to >9.5 m of recovery for the next 9.5-m cored interval.

A recovered core is divided into 1.5-m sections that are numbered serially from the top (Fig. F1). When full recovery is obtained, the sections are numbered from 1 through 7, with the last section possibly being shorter than 1.5 m (rarely, an unusually long core may require more than seven sections). When less than full recovery is obtained, as many sections as are needed to accommodate the length of the core are used; for example, 4 m of core would be divided into two 1.5-m sections and a 1-m section. If cores are fragmented and recovery $<100\%$, sections are numbered serially and the rest of the drilled interval is regarded as void, whether or not shipboard scientists think that the fragments were contiguous when in situ. In rare situations, a section <1.5 m may be cut to preserve features of interest (e.g., lithologic contacts).

By convention, material recovered from the core catcher is placed below the last section when the core is described and is labeled “core

F1. Examples of numbered core sections, p. 46.



catcher" (CC); in sedimentary cores, this is treated as a separate section. The core catcher is placed at the top of the cored interval in situations where material is recovered only in the core catcher. However, information supplied by the drillers or by logging may allow for more precise interpretation of the correct position of core catcher material within an incompletely recovered cored interval. By convention, when the recovered core is shorter than the cored interval, the top of the core is equated with the top of the cored interval. Samples taken from the cores are designated by distance measured in centimeters from the top of the section to the top and bottom of each sample.

A complete identification number for a sample consists of the following information: leg, site, hole, core number, core type, section number, piece number (for hard rock), and interval in centimeters measured from the top of the section. For example, a sample identification of "197-1203A-25R-1, 10–12 cm" indicates a 2-cm sample removed from the interval between 10 and 12 cm below the top of Section 1, Core 25 ("R" designates that this core was taken during rotary drilling) of Hole 1203A during Leg 197.

Core Handling

Sediment

As soon as a core is retrieved on deck, a sample is taken from the core catcher and taken to the paleontology laboratory for an initial age assessment. The core is then laid out on a long horizontal rack on the catwalk adjacent to the drilling floor. Next, the core is marked into section lengths, each section is labeled, and the core is cut into sections. The plastic core liner containing each section is then sealed at the top and bottom by gluing on color-coded plastic caps; blue to identify the top of a section and clear to identify the bottom. Caps are usually attached to the liner by coating the end of the liner and the inside rim of the cap with acetone.

Next, the sections of core are carried into the laboratory and each is labeled again using an engraver to permanently mark the full designation of the section onto the plastic core liner. The length of the core in each section and the core catcher sample are measured to the nearest centimeter; this information is logged into the shipboard CORELOG database program. After cores have equilibrated to room temperature (~3 hr), they are run through the multisensor track (MST), probes are inserted through holes drilled through the liner to measure thermal conductivity on relatively soft sediment, and the cores are split.

Cores of soft material are split lengthwise into working and archive halves. The softer cores are split with a wire or saw, depending on the degree of induration. Harder cores are split with a band saw or diamond saw. During Leg 197, the wire-cut cores were split from the bottom to top; thus, investigators should be aware that older material may have been transported up the core on the split face of each section.

The working half of the core is sampled for both shipboard and shore-based laboratory studies. Each extracted sample is logged into the sampling computer database program by the location and the name of the investigator receiving the sample. Records of all removed samples are kept by the curator at ODP. The extracted samples are sealed in plastic vials or bags and labeled. Samples are routinely taken for shipboard physical properties measurements and for calcium carbonate (coulometric) analysis.

The archive half is described visually. Smear slides are made from sediment samples taken from the archive half. Most archive sections are run through the cryogenic magnetometer. The archive half is then photographed using both black-and-white and color film, a whole core at a time. Close-up photographs (color and black and white) are taken of particular features for illustrations in the summary of each site, as requested by individual scientists. Both halves of the core are then placed into labeled plastic tubes, sealed, and transferred to cold-storage space aboard the drilling vessel. At the end of the leg, the cores are transferred from the ship in refrigerated airfreight containers to cold storage at the Gulf Coast Repository of the Ocean Drilling Program at Texas A&M University.

Igneous and Metamorphic Rocks

Igneous rock cores are handled differently from sedimentary cores. Once on deck, the core catcher sample is placed at the bottom of the core liner and total core recovery is calculated by shunting the rock pieces together and measuring the total length to the nearest centimeter. This information is logged into the shipboard CORELOG database program. The core is then cut into 1.5-m-long sections and transferred into the laboratory.

The contents of each section are transferred into 1.5-m-long sections of split core liner, where the bottom of oriented pieces (i.e., pieces that clearly could not have rotated top to bottom about a horizontal axis in the liner) are marked with a red wax pencil. This is to ensure that orientation is not lost during splitting and labeling. Important primary features of the cores also are recorded at this time. Core pieces are then photographed digitally while being rotated to acquire a full, circumferential image for later correlation with the Formation MicroScanner (FMS) logs. The core is then split into archive and working halves. A plastic spacer is used to separate individual pieces and/or reconstructed groups of pieces in the core liner. These spacers may represent a substantial interval of no recovery. Each piece is numbered sequentially from the top of each section, beginning with number 1; reconstructed pieces are all assigned the same number, but with a consecutive suffix letter (e.g., Piece 1A, 1B, etc.). Pieces are labeled only on the outer cylindrical surfaces of the core. If the piece is oriented, an arrow is added to the label pointing to the top of the section. Because pieces are free to rotate about a vertical axis during drilling, azimuthal orientation during Leg 197 was possible only by using paleomagnetic data.

In splitting the core, every effort is made to ensure that important features are represented in both halves. The archive half is described visually, then photographed with both black-and-white and color film, one core at a time. Nondestructive physical properties measurements, such as magnetic susceptibility, are performed on the archive half of the core. The working half is sampled for shipboard physical properties measurements, paleomagnetic studies, inductively coupled plasma-atomic emission spectroscopy (ICP-AES), X-ray diffraction (XRD), and thin section studies. The working half of the hard rock core is then sampled for shore-based laboratory studies. Records of all samples are kept by the curator at ODP. Both halves of the core are then shrink-wrapped in plastic to prevent rock pieces from vibrating out of sequence during transit, placed into labeled plastic tubes, sealed, and transferred to cold-storage space aboard the drilling vessel. As with the other Leg 197 cores,

they are housed at the Gulf Coast Repository of the Ocean Drilling Program at Texas A&M University.

LITHOSTRATIGRAPHY

Description of sedimentary deposits recovered during Leg 197 generally followed standard ODP methodology. The visual description of sedimentary units encountered during Leg 197 was made on split cores and includes documentation of (1) sediment composition based on visual inspection, smear slides, thin sections, and carbonate content and (2) degree of consolidation and presence of sedimentary and deformational structures (i.e., drilling-induced disturbance and bioturbation).

Barrel Sheet Data

Barrel sheets (Fig. F2) provide a summary of the most relevant information on the entire core and are presented with core photographs in the “Core Descriptions” for each site chapter (see the “Core Descriptions” contents list). Observations are first recorded on visual core description (VCD) forms and then summarized for entry into AppleCORE (version 8.1m) software, which generates a one-page graphical log of each core (“barrel sheet”). More specifically, the barrel sheets contain a wide variety of information such as graphic representation of lithology (Fig. F3), evidence of drilling disturbance and sedimentary structures, sample type (i.e., smear slide, thin section, whole-core sample, and X-ray diffraction), and lithologic description including texture and structure of sediment and sedimentary rocks and their color. In the graphic log, the symbols for sedimentary structures (e.g., bed thickness, bioturbation intensity, soft-sediment deformation) and structural and diagenetic features (Fig. F4) of soft and consolidated sediment are indicated either by patterns and symbols or by arrows placed as close as possible to their proper stratigraphic position. Copies of the detailed section-by-section VCD forms for each site can be accessed from the “Core Descriptions” contents list. Barrel sheets include the following information.

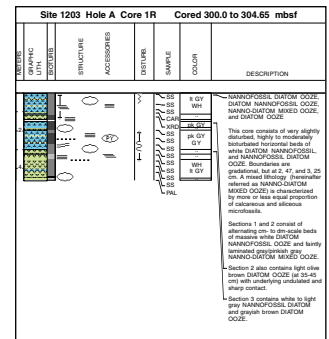
Lithology

Sediment lithology is represented by patterns in the “Graphic Lithology” column. This column may consist of one or as many as three vertical strips, depending on the number of the major end-member constituents (see “Classification of Sediment and Sedimentary Rocks,” p. 7) for mixed sediment. However, for Leg 197, only the pattern for the dominant lithologic component was entered. Because of the limitations of the AppleCORE software, thin intervals of interbedded lithologies cannot be adequately displayed at the scale used for the barrel sheets, but they are described in the “Description” column on the barrel sheet, where appropriate.

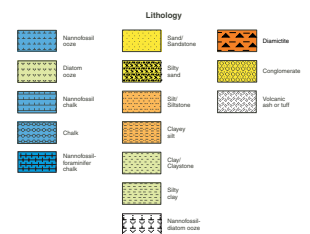
Drilling Disturbance and Sedimentary Structures

Natural structures (physical or biological) can be difficult to distinguish from disturbances created by the coring process. Deformation and disturbance of sediment that resulted from the coring process are illustrated in the “Drilling Disturbance” column (Fig. F2), using sym-

F2. Example barrel sheet, p. 47.



F3. Lithology/lithologic component symbols, p. 48.



F4. Sedimentary structure and disturbance symbols, p. 49.



bols shown in Figure F4. Blank regions indicate the absence of drilling disturbance. The degree of drilling disturbance for soft sediment was described using the following categories:

Slightly disturbed= bedding contacts slightly bent.

Moderately disturbed = bedding contacts bowed.

Highly disturbed = bedding hardly discernible, commonly showing sediment flow or fluidized structures.

Standard ODP categories exist for describing fragmentation in indurated sediment and rocks, but the only one appropriate to Leg 197 hard rock material is “highly fragmented,” which means pieces from the cored interval are probably in correct stratigraphic sequence (although they may not represent the entire section), but are not in their original position or coring orientation.

The “Bioturbation” column of the barrel sheet shows four levels of intensity:

Homogeneous = trace fossils are either absent or invisible because they occur in a completely biogenic fabric.

Low = rare, discrete burrows.

Moderate = burrows are generally isolated but locally overlap.

Intense = abundant, overlapping burrows, resulting in a nearly total disruption of sedimentary structures.

Stratification thickness was characterized as follows (McKee and Weir, 1953; Ingram, 1954):

Very thick bedded = >1 m thick.

Thick bedded = 30–100 cm thick.

Medium bedded = 10–30 cm thick.

Thin bedded = 3–10 cm thick.

Very thin bedded = 1–3 cm thick.

Thickly laminated = 10 mm thick.

Thinly laminated = 1–3 mm thick.

Very thinly laminated = <1 mm thick.

Sample Type

The stratigraphic position of samples taken for shipboard analysis is indicated in the “Samples” column of the barrel sheet according to the following codes:

PAL = biostratigraphy.

SS = smear slide.

TSB = thin section.

CAR = carbonate.

XRD = X-ray diffraction.

Owing to instrumental problems, the XRD data were not used except for general identification of dolomite. The XRD data provided should be used with caution. The low-angle data are not reliable.

Lithologic Description

A summary of the lithologic observations is given in the “Description” column of the barrel sheets. It consists of three parts: (1) a denomination in capital letters listing only the dominant sediment lithologies (major and minor lithology) observed in the core (e.g., CLAY and CALCAREOUS CLAY with FORAMINIFERAL OOZE and VOLCANIC ASH layers); (2) a general description of the core, including composition, color, sedimentary structures, bed thickness, and drilling disturbance, as well as any other general features in the core; and (3) descriptions and locations of thin, interbedded, or minor lithologies (e.g., normally graded FORAMINIFERAL OOZE, at Section 2, 45–80 cm).

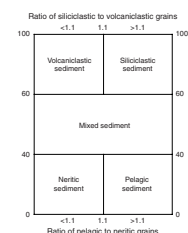
Color

Sediment color was determined visually by comparison with standard color charts (Munsell Color Company, Inc., 1975; Rock Color Chart Committee, 1991) and is reported in the VCD “Color” column and the “Description” column of the barrel sheet. In addition to determining color visually, select cores were scanned at 2- to 5-cm intervals using a Minolta CM-2002 spectrophotometer mounted on the archive multisensor track (AMST). The spectrophotometer measures reflectance in thirty-one 10-nm-wide bands of the visible spectrum (400–700 nm) on the archive half of each core section. Spectrophotometer readings were taken after cleaning the surface of each core section and covering it with clear plastic film. Calibration of the color scanner did not include a correction for the plastic film because it only had minor effects even with very bright-colored lithologies. The measurements were taken automatically and recorded by the AMST at evenly spaced intervals along each section. The area measured is a 8-mm-diameter circle, and the spectrophotometer integrates the sensed color over this area. It was not possible to program the AMST software to avoid measurements in intervals with a depressed core surface or in disturbed areas of core containing drilling slurry or biscuits. The color data are recorded in the Janus database and can be obtained from ODP. Additional detailed information about measurement and interpretation of spectral data with the Minolta spectrophotometer can be found in Balsam et al. (1997, 1998; Balsam and Damuth, 2000).

Classification of Sediment and Sedimentary Rocks

Primary and secondary sedimentary structures were described from observations of the archive cores. For granular sediment classification, we used the lithologic names according to the ODP sediment classification scheme (Mazzullo et al., 1988), which is shown in Figure F5. These naming conventions consist of a principal name based on depositional depth or environment (i.e., pelagic or neritic), degree of lithification (i.e., ooze, chalk, or chert), and texture (silt, sand, or clay). Sediment names for Leg 197 sites consist of a principal name identifying the dominant composition of the sediment (e.g., clay, diatom ooze, or radiolarian ooze [where any one of these three is >50%, but together they are]), and a modifier that precedes the principal name. A component with 10%–25% abundance is termed component-bearing, and one with 25%–50% abundance is termed component-rich (e.g., ash-rich clay- or radiolarian-rich diatom ooze). For a mixture of components, the principal

F5. Classes of granular sediment, p. 50.



name is preceded by major modifiers (in order of increasing abundance) that refer to components making up >25% of the sediment. Minor components that represent between 10% and 25% of the sediment follow the principal name in order of increasing abundance. As an example, an unconsolidated sediment that contains 30% nannofossils, 25% clay minerals, 20% foraminifers, 15% feldspar silt, and 10% manganese nodules would be described as a clayey nannofossil ooze with manganese nodules, feldspar silt, and foraminifers. Granular sediment is subdivided on the basis of composition and abundance of different grain types estimated from visual examination of the core, smear slides, thin sections, and by shipboard measurements of carbonate content. For naming the siliciclastic sediment we used the Udden-Wentworth grain-size classification scheme (Wentworth, 1922) (Fig. F6) and the ternary diagram (silt-sand-clay) (Fig. F7).

We used “volcaniclastic” as a nongenetic term, as described in “**Volcaniclastic Deposits,**” p. 15, in “Physical Volcanology.” In volcaniclastic sediment, the term ash (or tuff, if lithified) is used for sand-sized fractions, whereas lapilli is used for granule and cobble size categories. Terms that describe lithification vary depending on the dominant composition (i.e., calcareous pelagic organisms, siliceous microfossils, and siliciclastic/volcaniclastic material). In particular, we have the following:

1. Sediment derived predominantly from calcareous pelagic organisms (e.g., calcareous nannofossils and foraminifers): the lithification terms ooze, chalk, and limestone reflect whether the sediment can be deformed with a finger (ooze), can be scratched easily by a fingernail (chalk), or cannot be scratched easily (limestone).
2. Sediment derived predominantly from siliceous microfossils (diatoms, radiolarians, and siliceous sponge spicules): the lithification terms ooze, porcellanite, and chert reflect whether the sediment can be deformed with a finger (ooze), cannot be easily deformed manually (porcellanite), or displays a glassy luster (chert).
3. Sediment derived predominantly from siliciclastic material: if the sediment can be deformed easily with a finger, no lithification term is added and the sediment is named for the dominant grain size; for more consolidated material the lithification suffix “-stone” is appended to the dominant size classification (e.g., clay vs. claystone).
4. Sediment composed of sand-sized volcaniclastic grains: if the sediment can be deformed easily with a finger, the interval is described as volcaniclastic sediment; more consolidated material can be called a volcaniclastic sandstone or siltstone or tuff.

Grain shapes of coarse-grained components such as lithics in the gravel/pebble fraction are described using the major modifiers “rounded,” “subrounded,” “subangular,” and “angular” (Fig. F8).

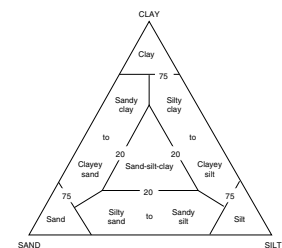
Smear Slides and Thin Sections

We determined grain size and composition of sediment using smear slides and thin sections. Smear slide samples were prepared according to the procedures described in the handbook for shipboard sedimentologists (Mazzullo et al., 1988). Identification of mineral and biogenic

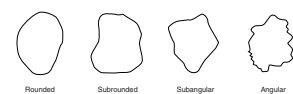
F6. Grain-size scale for siliciclastic sediment, p. 51.

Millimeters	µm	Phi (φ)	Wentworth size class
4096		20	
1024		12	Boulder (4 to 126)
256		10	
64		8	Pebble (2 to 64)
16		4	
3.36		-1.75	
2.81		-1.25	Clay
2.38		-1.25	
2.00		-1.00	
1.68		-0.75	
1.41		-0.50	Very coarse sand
1.06		-0.25	
0.84		0.00	
0.68		0.25	Coarse sand
0.54		0.50	
0.43		0.75	
0.36		1.00	
0.30		1.25	Medium sand
0.25		1.50	
0.20		1.75	
0.16		2.00	
0.13		2.25	
0.11		2.50	Fine sand
0.09		2.75	
0.07		3.00	
0.06		3.25	
0.05		3.50	Very fine sand
0.04		3.75	
0.03		4.00	
0.02		4.25	
0.01		4.50	Coarse silt
0.0075		4.75	
0.006		5.00	
0.005		5.25	
0.004		5.50	
0.003		5.75	
0.0025		6.00	Medium silt
0.002		6.25	
0.0015		6.50	Fine silt
0.001		6.75	Very fine silt
0.00075		7.00	
0.0006		7.25	
0.0005		7.50	Clay

F7. Diagram for naming siliciclastic sediment, p. 52.



F8. Grain shape comparator, p. 53.



components was carried out in accordance with Rothwell (1989). Sediment texture and mineral/biogenic components were estimated visually using the comparison chart shown in Figure F9. Tables summarizing data from thin sections and smear slides are included in the “Core Descriptions” for each site (see the “Core Descriptions” contents list). These tables include information about the sample location, whether the sample represents a dominant (D) or a minor (M) lithology, and the estimated abundance of different grain sizes and different grain types (percentages of sand, silt, and clay size fractions), together with all of the identified components.

We must emphasize that smear slide analysis provides only rough estimates of the relative abundances of detrital constituents. This circumstance reflects the fact that (1) mineral identification of fine silt to clay particles is difficult using only a petrographic microscope and (2) sand-sized grains tend to be underestimated because they cannot be incorporated into the smear. Accuracy of the carbonate content, estimated from smear slides and thin sections, was confirmed by chemical carbonate analyses performed according to standard shipboard procedures by the coulometer method (see Rea, Basov, Janecek, Palmer-Julson, et al., 1993).

Thin section analysis of microfacies followed the textural classification scheme of Dunham (1962). Matrix-supported rocks are classified as mudstone if they contain <10% and wackestone if they contain >10% grains.

For some samples, sieving for foraminifers was performed to improve smear slide estimation of this component.

BIOSTRATIGRAPHY

Initial biostratigraphic determinations for calcareous nannofossils were performed on core catcher samples. Additional samples were subsequently investigated from selected core sections to refine the biostratigraphic zonal assignments. Slides for nannofossil investigations were prepared by smearing sediment across a glass slide and attaching a cover glass. Taxa identifications were made under plane-polarized and cross-polarized light using a Zeiss Axioscope microscope.

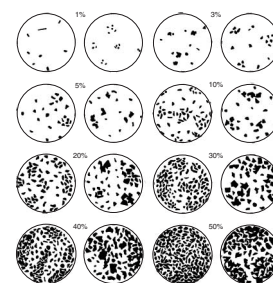
Relative abundance estimates for individual nannofossil species were made using a magnification of 1000×; abundances were estimated as follows:

- D = dominant (>100 specimens of a species per field of view).
- A = abundant (>10–100 specimens of a species per field of view).
- C = common (>1–10 specimens per field of view).
- F = few (1 specimen per 10 fields of view).
- R = rare (<1 specimen per 10 fields of view).
- B = barren (no nannofossils found).

Preservation of nannofossil specimens was characterized as follows:

- VG = very good (no dissolution or secondary overgrowths of calcite).
All specimens can be identified with certainty.
- G = good (little dissolution or secondary overgrowths). Essentially all specimens can be identified at the species level.

F9. Visual percentage estimation, p. 54.



ogy,” “Downhole Measurements,” and “Alteration and Weathering” sections of each site chapter were important in producing the final interpretation.

Methodology

The physical description of volcanic rocks and deposits recovered during Leg 197 was a multistage process. The first step involved defining boundaries of lithologic units by either visual identification of contacts or by inference from changes in igneous or volcanoclastic textures. This was followed by general description of the characteristic igneous textures, including macroscopic flow textures and structures and petrography (Fig. F11).

Our initial justification for placing unit boundaries changed as our understanding of the site improved, especially in light of data obtained from chemical analysis of identified lithologies and from physical properties and downhole measurements, which reflected major physical changes in the core (e.g., fragmental vs. coherent). Internal unit contacts (i.e., lava lobe boundaries or obvious bedding planes in volcanoclastic units) were documented wherever discernible, but more subtle boundaries, such as those between individual lava lobes, were usually not broken out despite their possible significance to the volcanological interpretation.

We examined individual lithologic units in more detail to determine their characteristic volcanological architecture (i.e., types and number of lithofacies as well as the processes responsible for their formation) (Figs. F12, F13). The observed lithofacies associations laid the foundation for a genetic volcanological interpretation of each lithologic unit (i.e., types and number of lava flows/lobes or depositional subunits). We also attempted to synthesize the observations from the different units, combining the data from the “Physical Volcanology and Igneous Petrology” and “Downhole Measurements” sections of each site chapter. This examination was particularly useful for comparing different sites.

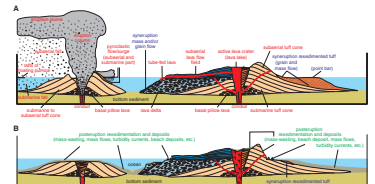
In the site chapters we use nongenetic terminology in the description of each unit unless the origin of a particular unit is known beyond a doubt. Consequently, genetic phrases such as “chill zone,” “pillowed,” “hyaloclastite,” or “flow-top breccia” are only used after proper lithologic identification was achieved. A unit-by-unit description and interpretation with explanations of the criteria used to separate the different units follows.

Lava Flows

Background

Traditionally, mafic lava flows have been divided into pillow, pahoehoe, and a’a flows (Macdonald, 1953, 1967) (Table T2). This morphological division is important because (1) the mode of lava emplacement for a’a and pahoehoe flows is fundamentally different and (2) despite similar emplacement mechanisms for pahoehoe and pillow lavas, they form in vastly different environments. A’a flows move like the treads on a bulldozer and are typified by a thermally inefficient mode of emplacement in open channels where they disrupt and mix their upper crusts. Pahoehoe and pillow lava flows, on the other hand, are characterized by insulating transport and growth by sequential lobe-by-lobe emplacement. The lava is transported in internal pathways (or lava tubes) to the

F13. Drawing illustrating eruption processes, p. 61.



T2. Characteristics of basalt lava types, p. 78.

active flow fronts, where they advance by inflating a lobe with a continuous crust, much like filling a rubber balloon with water (Walker, 1991; Hon et al., 1994).

A wide range of intermediate flow types occur between these two end-member types. Most subaerial transitional flow types have “pahoehoe” in their names: for example rubbly pahoehoe, slab pahoehoe, and toothpaste pahoehoe (Macdonald, 1953, 1967; Rowland and Walker, 1987; Keszthelyi and Thordarson, 2000; Keszthelyi et al., 2000), but some are closer in character to a’ā than to pahoehoe (Table T2).

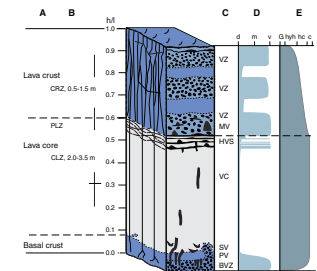
Determining lava type is relatively straightforward if centimeter-scale morphologic features of the flow tops and bottoms are recovered and well preserved. A’ā flows are characterized by angular, spinose clinker at both the flow tops and bottoms, whereas pahoehoe and pillow flows are characterized by smooth tops and bottoms (Figs. F14, F15). Transitional flows show some of the characteristics of both a’ā and pahoehoe lava flows (Table T2; Fig. F16). However, these features are most susceptible to erosion and alteration and are often not recovered in drill core.

Most subaerial lava flows are vesicular, although their porosity as well as vesicle shapes and size distributions vary widely. However, the vesiculation patterns (i.e., vesicle abundance, shape, and size distribution) vary systematically between flow types and typically exhibit enough constancy within each type that it is possible to use this property in conjunction with changes in petrographic textures and flow structures to make a positive identification (Table T2).

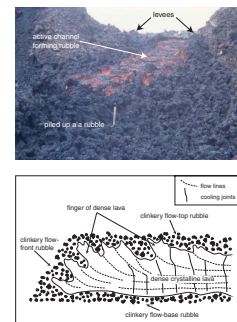
A’ā clinker primarily forms by the rupture of molten lava at the flow surface (Fig. F15). This can happen only where strain rates are high and/or the viscosity of the fluid lava is high (Peterson and Tilling, 1980). This tearing is a result of the non-Newtonian behavior of lava under these conditions. Large (10–200 cm wide) “arms” or “fingers” of lava from the massive interior of the flow commonly extend into the breccia, especially along well-defined shear zones (Lockwood and Lipman, 1980). The vesicle abundance in a’ā flows is typically low (<20 vol%), and the vesicles tend to be distorted, drawn out into elongate shapes by stretching or viscous deformation (Macdonald, 1953, 1967). A’ā flows also commonly contain partially resorbed pieces of entrained crust within the massive lava interior of the flow. These typically appear as fist-sized clots of small, highly distorted vesicles within the nonvesicular part of the flow. Entrainment of the breccia clasts into the interior of the flow is a powerful heat loss mechanism for a’ā flows (Crisp and Baloga, 1994), driving more rapid crystallization of the flow interior (Crisp et al., 1994) and leading to more efficient degassing.

Pahoehoe lavas are usually highly vesicular, with bulk porosity in excess of 20 vol% (range = 20–60 vol%) (Fig. F14). Thin pahoehoe lobes are often vesicular throughout and exhibit a gradual coarsening in vesicle size from lobe margins to the interior (Wilmoth and Walker, 1993). Thicker pahoehoe lobes are typically characterized by the threefold structure of vesicular upper crust, a dense core, and a thinner vesicular lower crust (Aubele et al., 1988; Thordarson and Self, 1998). To avoid confusion with the drilled core, we use the term massive lava interior instead of core throughout this volume. For other key structures of pahoehoe lavas we use the terminology from Thordarson and Self (1998) (Tables T3, T4). Key vesicle features are horizontal vesicular zones in the upper crust, horizontal vesicle sheets defining the boundary between the upper crust and the massive interior of the flow, vesicle cylinders, and pipe vesicles at the base (Fig. F14). The vesicles in the uppermost 1–10 cm (i.e., top of the upper crust) and lowermost 10–50 cm (i.e., the

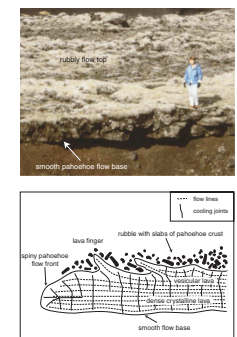
F14. Structure of pahoehoe sheet lobes, p. 62.



F15. Structure of a’ā flow, p. 63.



F16. Structure of rubbly pahoehoe flow, p. 64.



T3. General terminology for lavas, p. 79.

T4. Lobe structures, p. 80.

lower crust) of a pahoehoe flow are usually relatively small (0.1–3.0 mm in diameter) and highly spherical. However, the vesicular zones in the upper crust can vary in thickness from 0.5 to 200 cm and typically contain spherical vesicles 2–50 mm in size (Fig. F14). Commonly, they are marked by relatively sharp upper boundaries and grade downward into a zone of relatively low vesicularity. Vesicle sizes usually coarsen downward across each zone. The vesicles in the upper crust are thought to represent bubbles formed during lava emplacement caused by periodic drops in the internal hydrostatic pressure, which are due to sequential surface breakouts at the active lava front.

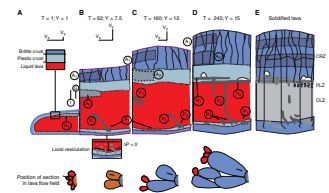
Pipe vesicles, vesicle cylinders, and horizontal vesicle sheets represent structures produced during lava emplacement by gas-driven melt segregation from the viscous part of the basal crust after 35%–50% crystallization (Thordarson and Self, 1998; T. Thordarson, unpubl. data). These features represent a population of vesiculation structures that are very different from the vesicular zones of the upper crust of pahoehoe flows (Fig. F17). Pipe vesicles are typically 0.3–0.7 cm in diameter, 3–15 cm in height, most commonly occur at the base of lobes, and are reliable indicators of flow margin. Pipe vesicles may grade into vesicle cylinders, which in turn lead to 1- to 20-cm-thick horizontal vesicle sheets at the base of the upper vesicular crust (Thordarson and Self, 1998). Vesicle cylinders and horizontal vesicle sheets typically contain vesicular segregated differentiates that can have micropegmatite textures and are synonymous with segregation veins (e.g., Goff, 1996). The vesicles in these segregation structures are usually 1–5 mm in size with highly irregular outlines and commonly exhibit evidence of growth by coalescence. We paid special attention to occurrences of segregated melt structures because their more evolved composition (richer in K than host lava) and feldspar-dominated mineralogy makes them ideal targets for ^{40}Ar - ^{39}Ar dating.

We can use the thickness of the upper crust of an inflated pahoehoe lobe to calculate the duration of active flow. The thickness of the upper vesicular crust is interpreted as a direct measurement of the amount of lava that solidified while new lava was being injected into the flow. A cooling model allows the translation of this thickness into time. We estimate the duration of active flow using the Hon et al. (1994) empirical cooling model as adapted by Thordarson (1995). This technique and its limitations and errors are described in more detail in Self et al. (1997, 1998) and Thordarson and Self (1998).

Transitional lavas fall into three broad categories:

1. Lavas such as toothpaste or “sharkskin” pahoehoe involve emplacement of highly viscous lavas at very low strain rates (Rowland and Walker, 1987). These flows do not form brecciated tops.
2. The second category of transitional lava is slab pahoehoe, which involves emplacement of relatively low-viscosity lava under very high strain rates (Peterson and Tilling, 1980). Such high strain rates are usually not sustained and are, instead, associated with pulses of higher volumetric flux.
3. High strain rates are also associated with surges through the molten interior of larger sheet lobes and result in the formation of rubbly pahoehoe lava. Such surges disrupt the stationary pahoehoe crust, and the coherent slabs are carried along by the moving lava and piled up into rubbly mounds and flow ridges (Thordarson and Self, 1993; Keszthelyi and Thordarson, 2000;

F17. Growth stages of a pahoehoe sheet lobe, p. 65.



Keszthelyi et al., 2000). The individual clasts usually demonstrate the full range of brittle to ductile deformation as the upper chilled portion cracks and the lower hotter portion deforms plastically to the disruption.

Lava flows that entered water or erupted subaqueously may form pillow basalt, hyaloclastites, or peperites. The latter two are volcanoclastic sediments that form by quenched fragmentation. Pillow basalt formed in deep water (1000 m depth) can usually be distinguished from pahoehoe flows by the thicker glass rinds, significantly lower vesicularity (<5 vol%), and the presence of marine sediment between the pillows. However, pillow basalt formed in the upper 1000 m of the water column often consists of moderately to highly vesicular lava, and thus care needs to be taken to differentiate it from compound pahoehoe lavas constructed from decimeter- to meter-sized lobes. Larger subaqueous flows may form sheetlike flows (Ballard and van Andel, 1979), and their morphology is controlled by local flow rate, which is primarily a function of slope and eruption rate (Gregg and Fink, 1995).

Logging Procedures

After defining the main lava sequences, we examined each unit in more detail to record its internal architecture. Although we made every effort to have unit boundaries reflect individual lava packages, the term “unit” should not be considered synonymous with “lava flow” in this volume.

We made general observations during the initial lithologic description of the rocks, such as intervals of coherent and fragmental lava facies along with gross changes in vesicularity and crystallinity (Fig. F11). Often, time did not permit detailed examination of all the lobes and we subjected only a subset to full scrutiny. This was followed by more systematic description of units concentrated on documenting vertical changes in crystallinity and vesicularity as well as occurrence and orientation of macroscopic vesiculation structures. Definitions and abbreviations of the categories used in reporting the type, size, and abundance of these properties are given in Table T5.

We paid special attention to vesiculation features by recording (1) volume percentage, (2) average size range, (3) shape, and (4) grading (fining upward or coarsening upward) of the vesicles at intervals appropriate for the variability shown in the core (typically across 10- to 100-cm intervals). The volume fraction of vesicles was estimated using visual percentage estimate charts and was grouped into four categories: nonvesicular (<1%), sparsely vesicular (1%–5%), moderately vesicular (5%–20%), and highly vesicular (>20%). The average vesicle size is a measure of what appeared to be a typical vesicle size. Special attention was paid to gradual changes in vesicle size because such size grading when coupled with changes in groundmass texture (i.e., fining of grain size and appearance of feathery or dendritic crystal forms) was very helpful in locating lobe boundaries when quenched glassy lobe margins were not recovered. We estimated vesicle sphericity using the charts produced for describing sedimentary rocks. During these measurements, we also noted evidence of growth by coalescence, occurrence, and orientation of elongated vesicles.

Finally, during the synthesis of the various data sets, we estimated the thickness of the various units and flows. It is very important to note that ODP curation procedures assume that the top of recovered material is from the top of the cored interval. This can lead to large (up to 9 m)

T5. Igneous texture/structure,
p. 81.

differences between the curated depth and the actual depth. Downhole logging measurements were required to produce more accurate estimates of flow thicknesses.

In fragmental lava facies we documented volcanoclastic textures using standard sedimentological techniques (i.e., clast vs. matrix modal proportions, clast size, shape, sorting, and lithology) (Fig. F11). Of particular interest was the presence (or absence) of features diagnostic of viscous or quenched fragmentation while the lava was hot. These include clasts engulfing fragments of other (earlier) clasts, welding, glassy margins surrounding the clasts, extensions of the interior of the flow into the breccia, entrained clasts within the interior of the flow, and the presence of a basal breccia. We used changes in clast morphology and crystallinity as well as changes in vesicle abundance and shape to identify clast types within the breccia.

Our identification and interpretation of the lava types involved three basic steps: (1) we initially tied the observed lava facies associations and structures to physical processes, (2) the emplacement style of individual flows was then inferred, and (3) the environmental setting (e.g., subaerial or submarine) for the whole sequence was assessed. The lava flow types and the criteria for their identification is listed in Tables T3 and T4. Our interpretations relied most heavily on observations from active volcanism in Hawaii and on studies of the physical volcanology of subaerial and subaqueous lava flows in Iceland and the Columbia River Basalt Group in the United States (e.g., Swanson, 1973; Walker, 1991; Mattox et al., 1993; Hon et al., 1994; Keszthelyi and Self, 1998; Keszthelyi et al., 2000; Thordarson, 2000; Thordarson and Self, 1998).

Volcanoclastic Deposits

We used “volcanoclastic” as a nongenetic term for any fragmental aggregate of volcanic parentage containing >60% volcanoclastic grains and <40% other types of clastic and/or biogenic material. This definition is broader than that for pyroclastic deposits because the term “pyroclastic” strictly applies only to products of explosive volcanic activity and includes hydrovolcanic deposits formed by explosive interaction between magma and water and nonexplosive quenched fragmentation (i.e., hyaloclastite and peperite). This definition also includes epiclastic sediment (the volcanic detritus produced by erosion of volcanic rocks); the term “volcanoclastic” does not imply any active volcanism at the time of deposition.

The subclassification of volcanoclastic sediment followed here differs from the standard ODP classification (Mazzullo et al., 1988) in that we adopt a descriptive (nongenetic) terminology similar to that employed during ODP Leg 183 (Coffin, Frey, Wallace, et al., 2000). Unless a pyroclastic origin for sediment could be defined, we described deposits of volcanic provenance (volcanoclastic) according to the classification scheme for clastic sediment, noting the dominance of volcanic grains. We followed the clastic textural classification of Wentworth (1922) to separate the various volcanic sediment types and sedimentary rocks (according to grain size) into volcanic gravel (>2 mm), volcanic sand (2–0.0625 mm), volcanic silt (0.0625–0.0039 mm), and volcanic clay (<0.0039 mm). For coarse-grained and poorly sorted consolidated volcanoclastic sediment such as those produced by gravity currents, we applied the terms volcanic breccia (angular clasts) or volcanic conglomerate (rounded clasts) and used lithologic or structural modifiers for further description.

We classified volcanic sediment by designating a principal name and major and minor modifiers. The principal name defines its grain-size class (e.g., gravel, sand, silt, or clay). Relative proportions of the vitric (glass), crystal (mineral), and lithic (rock fragment) components of the sediment are used to determine additional modifiers in the name and are placed before the principal name. For example, volcanic sand composed of 75% glass, 5% feldspar crystals, and 20% lithic fragments is named vitric-lithic volcanic sand. Volcanological features were recorded on both volcanoclastic sediment and igneous rock VCD forms (see the “Core Descriptions” contents list). We adopted the classification scheme of Fisher and Schmincke (1984) where the evidence for a pyroclastic origin was unequivocal. In these instances we used the grain-size terms volcanic breccia (>64 mm), lapilli (lapillistone [2–64 mm]), and ash (tuff [<2 mm]). Sedimentary structures included graded bedding, cross-bedding, planar laminations, foreset bedding, dune forms, and ripples.

Igneous Petrology

Core Curation and Shipboard Sampling

To describe important mineralogic and structural features in both the archive and working halves, we examined core sections containing igneous rocks prior to cutting with a diamond-impregnated saw. Each piece was numbered sequentially from the top of the core section and labeled on the outside surface. Pieces that could be fitted together were assigned the same number and were lettered consecutively (e.g., 1A, 1B, 1C, etc.). Plastic spacers were placed between pieces with different numbers. The presence of a spacer may represent a substantial interval of no recovery. If it was evident that an individual piece had not rotated about a horizontal axis during drilling, an arrow was added pointing to the top of the section.

Nondestructive physical properties measurements, such as color, imaging, and natural gamma ray emission were made on the core before it was split (see “Physical Properties,” p. 27). After the core was split, lithologic descriptions were made of the archive half and the working half was sampled for shipboard physical properties measurements (see “Physical Properties,” p. 27), magnetic studies (see “Paleomagnetism and Rock Magnetism,” p. 23), thin sections, and XRD and ICP-AES instrumental analyses. The archive half was described on the VCD form and was photographed. To minimize contamination of the core with platinum-group elements and gold, scientists and technicians removed jewelry from hands and wrists prior to handling.

Visual Core Descriptions

We used VCD forms to document each section of the igneous rock cores. The left column on the form, adjacent to the core photograph, represents the archive half. A horizontal line across the entire width of the column denotes a plastic spacer. Oriented pieces are indicated on the form by an upward-pointing arrow to the right of the piece. The key to the symbols, colors, and other notations used on the VCDs can be seen in Figure F18.

Locations of samples selected for shipboard studies are indicated in the column headed “Shipboard Studies,” with the following notations:

F18. Igneous texture/structure definitions, p. 66.

Phenocryst	a Aphitic (<1%)	s Sparsely phyric (1%-2%)	m Moderately phyric (2%-10%)	h Highly phyric (>10%)
Groundmass/ Grain size	g Glass	a Aphantic (<1 mm)	f Fine grained (1-2 mm)	m Medium grained (2-5 mm)
Vein Structure	d Pipe vein (radial)	v Vesicle cylinder (flow)	h Horizontal vein (+ segregation vein)	m Mega- vein
Volcanicity	n Nonvesicular (<1%)	s Sparsely vesicular (1%-5%)	m Moderately vesicular (5%-20%)	h Highly vesicular (>20%)
Vein		v		
		V Vein ground		

- XRD = X-ray diffraction analysis.
- ICP = inductively coupled plasma–atomic emission spectrometry analysis.
- TSB = petrographic thin section.
- PP = physical properties measurements.
- PMAG = paleomagnetic measurements.

Structural features are noted in the “Volcanic Structures” column and include vesicularity (based on vesicle content):

- NV = nonvesicular (<1%).
- SV = sparsely vesicular (1%–5%).
- MV = moderately vesicular (5%–20%).
- HV = highly vesicular (>20%).
- X = location of xenoliths.

The nature of the groundmass is broadly represented in the “Groundmass Grain Size Crystallinity” column on the VCD to indicate the presence of different lava lobes in a given core section. The following notation is used for crystallinity:

- C = holocrystalline (90%–100% crystals).
- hc = hypocrySTALLine (50%–90% crystals).
- hyh = hypohyaline (10%–50% crystals).
- G = hyaline (glass) (0%–10% crystals).

The following notation is used for grain size:

- pc = phanerocrystalline (phaneritic).
- cg = coarse grained (>5 mm).
- mg = medium grained (2–5 mm).
- fg = fine grained (1–2 mm).
- ap = aphanitic (<1 mm).
- mc = microcrystalline (<0.5 mm).
- cc = cryptocrystalline (not visible under binocular microscope).

The column “Phenocryst %” is used to represent a visual estimation of abundance and variation throughout the core section using the following notations (based on phenocryst content):

- A = aphyric (<1%).
- Sp = sparsely phyric (1%–2%).
- Mp = moderately phyric (2%–10%).
- Hp = highly phyric (>10%).

The “Alteration” column is used to denote the presence of veins by “V” and gives an estimate of the degree of alteration as follows (based on the percent of rock formed by alteration products):

- f = unaltered (<2%).
- s = slight (2%–10%).
- m = moderate (10%–40%).
- h = high (40%–80%).
- vh = very high (80%–95%).
- c = complete (95%–100%).

Further details can be found in [“Alteration and Weathering,”](#) p. 22.

We subdivided the core into consecutively numbered lithologic units (denoted in the “Lithologic Unit” column on the VCD) on the basis of changes in color, structure, brecciation, grain size, vesicle abundance, mineral occurrence and abundance, and the presence of sedimentary interbeds. Intercalated sediment horizons and volcanic breccias were often designated as “a” and the underlying volcanic rock as “b” within the same unit, unless definitive evidence was available that allowed us to break these out as separate units.

Written descriptions accompany the schematic representation of the core sections and include the following:

- a. The leg, site and hole, core, type, and section number (e.g., 197-1203A-15R-3), as well as the top of the core section measured in meters below seafloor.
- b. The unit number (consecutive downhole), the rock name (see below), and the piece numbers. We assigned provisional rock names on the basis of hand specimen observation (hand lens and binocular microscope) and later checked these assignments by examining thin sections. Porphyritic rocks were named by phenocryst type; the term “phenocryst” was used for a crystal that was significantly (typically five times) larger than the average size of the groundmass crystals and/or generally euhedral in shape. This nomenclature is sensitive to changes in the groundmass grain size (e.g., a single cooling unit could have a moderately phyrlic aphanitic margin and an aphyric fine-grained interior without any change in the distribution or size of the early formed crystals). To avoid the problem of describing pillow margins as phyrlic and cogenetic pillow interiors as aphyric, we based our terminology on the aphanitic margins of cooling units. Thus, if aphanitic pillow margins were sparsely olivine-phyric basalt, we described the fine-grained interiors using the same name even though the euhedral olivine phenocrysts in the pillow interiors were similar in size to groundmass plagioclase laths. Many porphyritic basalts recovered during Leg 197 exhibited a range of groundmass crystal sizes, making estimation of phenocryst populations approximate. The phenocryst abundance descriptors (defined above) were further modified by including the names of phenocryst phases, in order of decreasing abundance. Thus, a “highly olivine-plagioclase-phyric basalt” contains >10 vol% phenocrysts, the dominant phenocryst being olivine, with lesser amounts of plagioclase. As long as the total phenocryst content exceeds 1%, the minerals named include all of the phenocryst phases that occur in the rock.
- c. Contact relations and unit boundaries. After we made lithologic descriptions, we attempted to integrate the observations to define unit boundaries. The boundaries often reflect major physical changes in the core (e.g., lobed vs. massive) that were also observed in the physical properties and downhole measurements. Intervals of sediment and/or hyaloclastite, changes in vesicularity, alteration, volume fraction, and type of matrix also define lithologic contacts. Where possible, whole-rock chemical analyses by ICP-AES (see [“ICP-AES Analysis,”](#) p. 20) are used to investigate chemical differences between units. Note that whereas every effort was made to have unit boundaries reflect individual lava packages, the term “unit” should not necessarily be

considered synonymous with “lava flow” in this volume. See [“Physical Volcanology,”](#) p. 10, for further details on contact relations and unit boundaries.

- d. Phenocrysts. This entry describes the types of minerals visible with a hand lens or binocular microscope and their distribution within the unit and, for each phase, their abundance (volume percent), size range (millimeters), shape, and degree of alteration, with further comments if appropriate.
- e. Groundmass texture and grain size: glassy, aphanitic (<1 mm), fine grained (1–2 mm), medium grained (2–5 mm), or coarse grained (>5 mm). Changes in grain size and proportions of crystals and glass within units were also noted.
- f. Vesicles. This entry records vesicle abundance (visual estimates of the volume fraction), size, shape (sphericity), and whether the vesicles are empty or filled and the nature of the filling (Table T5).
- g. Color name and code (for the dry rock surface) according to the Munsell Rock Color Charts (Munsell Color Co., 1991).
- h. Structure. This entry refers to whether the unit is massive, lobed, hyaloclastic, banded, brecciated, scoriaceous, or tuffaceous. We sought to produce an integrated picture of the style of volcanism and environmental setting of each drill site by identifying features that are diagnostic of specific physical processes. Lobed sequences were inferred using the presence of glassy margins, groundmass grain-size variations, and vesicle-rich bands. A section was described as massive if there was no evidence of lobes, even though it may be part of a lobed sequence. Every effort was made to distinguish brecciated lava from volcanoclastic rocks.
- i. Alteration. We graded the degree of alteration (based on percent of alteration products by volume) as follows:

- f = unaltered (<2%).
- s = slight (2%–10%).
- m = moderate (10%–40%).
- h = high (40%–80%).
- vh = very high (80%–95%).
- c = complete (95%–100%).

Changes of alteration through a section or unit were also noted. Additional detailed descriptions of alteration and weathering of igneous units are reported in [“Alteration and Weathering,”](#) p. 22.

- j. Veins and fractures: their abundance, width, and mineral linings and fillings. Additional detailed descriptions of vein materials and orientations are reported in [“Alteration and Weathering,”](#) p. 22.
- k. Any additional comments.

Thin Section Descriptions

We examined thin sections from the core intervals noted on the VCD forms to complement and refine the hand specimen observations. In general, the same terminology was used for thin section descriptions as for the visual core descriptions. The percentages of individual phenocryst, groundmass, and alteration phases were estimated visually,

and textural descriptions are reported in “Thin Sections” for each site (see the “[Core Descriptions](#)” contents list). The textural terms used are defined by MacKenzie et al. (1982). For some porphyritic basalt, the thin section and visual core descriptions may differ slightly, typically because small plagioclase laths in a rock with seriate texture are visible only in thin section. Thus, a rock described visually as olivine-plagioclase-phyric may be plagioclase-olivine-phyric in the thin section description. Similarly, vitric and lithic components may be estimated differently in volcanoclastic hand samples; therefore, thin section examination may result in modification of a rock name. We generally described at least one thin section per defined unit.

ICP-AES Analysis

We selected representative samples of major lithologic units for shipboard ICP-AES analysis. Large whole-rock pieces were first cut with a diamond-impregnated saw blade and ground on a diamond wheel to remove surface contamination. Samples were washed in an ultrasonic bath containing methanol for ~10 min, followed by three consecutive ~10-min washes in an ultrasonic bath containing nanopure deionized water, and then dried for ~12 hr in an oven at 110°C. The cleaned whole-rock samples (~20 g/cm³) were reduced to fragments <1 cm in diameter by crushing between two disks of Delrin plastic in a hydraulic press followed by grinding for ~5 min in a Spex 8510 shatterbox with a tungsten carbide barrel. The sample powders were weighed on a Scientech balance and ignited to determine weight loss on ignition (LOI).

We weighed 0.100 ± 0.002-g aliquots of the ignited whole-rock powders and mixed them with 0.4000 ± 0.0004 g of Li metaborate (LiBO₂) flux that had been preweighed on shore. Standard rock powders and full procedural blanks were included with the unknowns for each sample run. All samples and standards were weighed on the Cahn Electro balance. Weighing errors are conservatively estimated to be ±0.00001 g.

Mixtures of flux and rock powders were fused in Pt-Au crucibles at 1050°C for 10–12 min in a bead sampler NT-2100. A 10-μL aliquot of 0.172-mM aqueous lithium bromide (LiBr) solution was added to the mixture before fusion as an antiwetting agent to prevent the cooled bead from sticking to the crucible. Cooled beads were transferred to 125-mL polypropylene bottles and dissolved in 50 mL of 2.3-M HNO₃ by shaking with a Burrell wrist action bottle shaker for 1 hr. After digestion of the glass bead, all of the solution was filtered to 0.45 μm into a clean 60-mL widemouthed polypropylene bottle. Next, 2.5 mL of this solution was transferred to a plastic vial and diluted with 17.5 mL of 2.3-M HNO₃ to bring the total volume to 20 mL. The solution-to-sample dilution factor for this procedure is ~4000. Dilutions were conducted using a Brinkman Instruments dispensette (0–25 mL).

Major (Si, Ti, Al, Fe, Mn, Mg, Ca, Na, K, and P) and trace (Zr, Y, Sr, Ba, Ni, Cr, Sc, V, Co, Cu, and Zn) element concentrations of powder samples were determined with the JY2000 Ultracore ICP-AES. The JY2000 sequentially measures characteristic emission intensities (with wavelengths between ~100 and 800 nm). ICP-AES protocols for dissolution and analysis of rock powders were developed by Murray et al. (2000; see also Shipboard Scientific Party, 2001). The hard rock analytical procedure was refined during Leg 197. The elements analyzed, emission lines used, and the specific analytical conditions for each sample run during Leg 197 are provided in Table [T6](#).

The JY2000 plasma was ignited 30 min before each run to allow the instrument to warm up and stabilize. After the warm-up period, a zero-order search was performed to check the mechanical zero of the diffraction grating. After the zero-order search, the mechanical step positions of emission lines were tuned by automatically searching with a 0.002-nm window across each emission peak using the University of Massachusetts Kilauea basalt laboratory standard K-1919, prepared in 2.3-M HNO₃. The only exception is P, which was automatically searched by using a single-element standard. During the initial setup, an emission profile was collected for each peak, using the K-1919 standard, to determine peak-to-background intensities and to set the locations of background points for each element. The JY2000 software uses these background locations to calculate the net intensity for each emission line. The photomultiplier voltage was optimized by automatically adjusting the gain for each element using the standard (BHVO-2, JB-1a, BIR-1, or K1919) with the highest concentration for that element. Before each run, a profile of the K-1919 standard was collected to assess the performance of the instrument from day to day. A typical sample run lasted ~12–14 hr, depending on the number of samples and replicate analyses.

All ICP-AES data presented in the site chapter reports were acquired using Mode 2 of the JY2000 software, except for Fe, Mg, Mn, Ba, Cr, Sc, V, and Y data, which were acquired in Mode 5. In Mode 5, the intensity at the peak of an emission line is measured and averaged over a given counting interval, repeated three times sequentially. Mode 2 fits a Gaussian curve to a variable number of points across a peak and then integrates to determine the area under the curve. The parameters for each run are given in Table T6. Each unknown sample was run at least twice, nonsequentially, in all sample runs.

A typical ICP-AES run includes (1) a set of three certified rock standards (BHVO-2, BIR-1, and JB-1a) (Table T7) run at the beginning, middle, and end of the sample run; (2) up to 11 unknown samples; (3) a drift-correcting sample (the K-1919 standard) analyzed every fourth sample position; and (4) a blank solution run near the beginning, middle, and end of each run. A 2.3-M HNO₃ wash solution was run for a minimum of 90 s between each of the samples and standards.

Following each sample run, the raw intensities were transferred to a data file and data reduction was completed using a spreadsheet to ensure proper control over standardization and drift correction. Once transferred, intensities for all samples were corrected for the full procedural blank. A drift correction was then applied to each element by linear interpolation between drift-monitoring solutions run before and after a particular batch of samples. The interpolation was calculated using the lever rule. Following blank subtraction and drift correction, concentrations for each sample were calculated from the average intensity per unit concentration for the U.S. Geological Survey (USGS) standard BHVO-2, which was analyzed twice during the run.

Estimates of accuracy and precision for major and trace element analyses were based on replicate analyses of BHVO-2, BIR-1, and JB-1a standards, the results of which are presented in Table T7. In general, run-to-run relative precision by ICP-AES was better than 2% for the major elements. Run-to-run relative precision for trace elements was generally <5%. Exceptions typically occurred when the element in question was near the detection limit of the instrument (see Table T6 for instrument detection limits).

T7. USGS standards, p. 83.

ALTERATION AND WEATHERING

All igneous rocks recovered during Leg 197 have undergone secondary alteration or weathering in subaerial, shallow subaqueous, or deep marine environments. Many features of low-temperature submarine alteration and subaerial weathering appear similar and are indistinguishable in the cores. In these descriptions, alteration is representative of chemical transformations of mineral assemblages induced by interactions with hydrothermal fluids. Weathered materials are formed at the Earth's surface (ambient temperature and pressure) by interactions with meteoric fluids. Note that the products of subaerial weathering may be further modified through alteration on the seafloor.

On the igneous rock visual core description forms, rocks were graded (based on volume of alteration products) as follows:

- f = unaltered (<2%).
- s = slightly altered (2%–10%).
- m = moderate alteration (10%–40%).
- h = highly altered (40%–80%).
- vh = very highly altered (80%–95%).
- c = complete alteration (95%–100%).

We determined the types, forms, and distribution of secondary alteration/weathering effects as well as abundances of veins and vesicles along with associated secondary minerals. Features related to any changes in the alteration/weathering styles through a section or an igneous unit are reported on the VCD. Alteration and vein core description logs were tabulated to provide a consistent characterization of the rocks and to quantify the different alteration types. Descriptions are based mostly on hand specimen observations of cut, wet surfaces, and specific clay, zeolite, and carbonate minerals are not generally distinguished, except where crystal morphology allows unequivocal identification. As the main objectives of the leg are centered on paleomagnetism, we paid special attention to the occurrence of secondary iron oxide minerals and alteration of primary igneous opaque phases (e.g., titanomagnetite altered to maghemite). Where additional mineralogical evidence is available from either thin section descriptions and/or X-ray diffractograms, these identifications were integrated into the alteration and vein logs and the VCDs. XRD analyses were conducted on board the ship, but instrumental problems were encountered. The data presented in this volume should therefore be used with caution as a general guide for mineral recognition rather than for precise determinations. Table T8 provides a list of abbreviations used in the alteration and vein logs. Colors were taken from Munsell Rock Color Charts or Munsell Soil Color Charts (Munsell Color Co., 1991, 1975, respectively).

We recorded the following information in the alteration and vein logs:

1. The alteration log (Fig. F19) was used to record bulk rock alteration and vesicle filling. Each entry records the igneous unit and identifiers for the core, section, and the depth below seafloor of the top of each piece. Also recorded were visual estimates of the degree of alteration based on a scale ranging from 0 for unaltered samples to 5 for complete alteration, presence of secondary minerals such as Fe oxides and clay, visual estimates of vesicularity

T8. Abbreviations used in alteration and vein logs, p. 84.

F19. Example of the alteration log, p. 67.

based on a scale ranging from 0 for nonvesicular samples to 3 for highly vesicular samples, and mineral fillings of vesicles.

- The vein log (Fig. F20) was used to record the presence, location, apparent orientation, width, and mineral content of veins observed on the cut surface of the cores. Each entry records the igneous unit and identifiers for the core, section, piece, and the depth below seafloor of the top of each piece. For each vein, the depth, location of the top and bottom, vein width (in millimeters), apparent orientation, mineral fillings, and proportions of the feature are recorded. If a related alteration halo is present, its color, half-width (in millimeters), alteration mineralogy, and proportions are described. A column for comments is included.

F20. Example of the vein log, p. 68.

The table is a grid with approximately 15 columns and 25 rows. The columns are labeled with various parameters: 'Core', 'Section', 'Piece', 'Depth (m)', 'Top (m)', 'Bottom (m)', 'Width (mm)', 'Orientation (°)', 'Mineral', 'Proportion (%)', 'Alteration Halo Color', 'Alteration Halo Half-Width (mm)', 'Alteration Halo Mineralogy', 'Alteration Halo Proportion (%)', and 'Comments'. The rows contain numerical and text data corresponding to these parameters for different vein observations.

PALEOMAGNETISM AND ROCK MAGNETISM

Paleomagnetic and rock magnetic investigations during Leg 197 were focused on obtaining inclination data that could be used to derive preliminary estimates of (1) the time intervals recorded by the basaltic sequences drilled, (2) the paleolatitude of the Emperor Seamounts (Detroit, Nintoku, and Koko Seamounts), and (3) the relative contributions of induced and remanent magnetizations in the basement rocks. This was accomplished by the routine measurement of natural remanent magnetization (NRM), detailed alternating-field (AF) demagnetizations and subsequent remanence measurements, and measurements of magnetic susceptibility. These measurements were mainly conducted on discrete samples taken from the working core halves.

Detailed stepwise AF demagnetizations were performed to isolate characteristic remanent magnetization (ChRM) components and to quantify magnetic overprints. Characteristic directions were fit using principal component analysis (Kirschvink, 1980). ChRM inclinations from the samples of each igneous flow unit were averaged following the method of McFadden and Reid (1982). A potential problem in obtaining paleolatitude data from any basalt drill hole is the uncertain time-scale between eruptions. If most flows reflect rapid eruptions, one could easily obtain a biased paleolatitude estimate by giving equal weight to each flow unit. To address this concern, the inclination-only averages derived from each flow unit were checked for serial correlation using geological constraints provided by visual core descriptions, thin section analyses, and geochemical analyses (see “Physical Volcanology and Igneous Petrology,” p. 10).

Independent paleomagnetic inclination groups determined from these analyses were used to estimate the angular dispersion recorded by the data (Tarduno and Sager, 1995; Tarduno and Cottrell, 1997). This was done by transforming the directional angular dispersion, estimated from the inclination groups, into geomagnetic pole space (Cox, 1970). These estimates of angular dispersion were compared to global data syntheses (McFadden et al., 1991) to determine whether a given basement section sampled sufficient time (over several thousand years) to average geomagnetic secular variation. Inclination units were further averaged to calculate mean paleolatitudes and 95% confidence intervals.

In addition to the measurements of discrete basalt samples discussed above, select sediment cores were analyzed. These investigations included pass-through measurements of NRM of both archive-half cores and discrete samples from the working-half cores. Select AF demagneti-

zations were also performed. The measurement technique applied to the sediment cores varied as a function of core recovery and disturbance.

Laboratory Instruments

The remanence of archive-half sections and oriented discrete samples from the working-half sections was primarily measured using a pass-through 2-G Enterprises DC-superconducting quantum interference device (SQUID) rock magnetometer (model 760R). The magnetometer is equipped with an in-line AF demagnetizer (2-G model 2G600), where samples can be demagnetized to peak fields of 80 mT. Both the magnetometer and AF demagnetizer are interfaced with a PC-compatible computer and are controlled by the 2-G Long Core software (Core Logic). Some discrete samples were also measured using a Molspin Minispin spinner magnetometer. A model D-2000 DTech Inc. AF demagnetizer was used for stepwise demagnetization of the discrete samples measured with the Molspin magnetometer. The DTech AF demagnetizer is capable of peak fields up to 200 mT.

Low-field magnetic susceptibility was measured for select sediment whole-core sections using a Bartington Instruments model MS2 susceptibility meter attached to the MST (see [“Physical Properties,”](#) p. 27). The susceptibility sensor for whole-core measurements (MS2C) has an 88-mm coil diameter, and the core passes through the sensor. Magnetic susceptibilities for discrete samples were measured using either a Geofyzika Brno Kappabridge KLY-2 magnetic susceptibility meter or a Bartington Instruments model MS2 susceptibility meter. Select samples were chosen for measurement of anisotropy of magnetic susceptibility with the KLY-2.

Calibration

Test samples with known magnetic directions and intensities from the University of Rochester were used to test the calibration of the 2-G SQUID and Molspin Minispin magnetometers. Calibration samples were available on board for the Molspin magnetometer, the Bartington susceptibility meter, and the Kappabridge magnetic susceptibility meter. Samples that were measured with the 2-G SQUID magnetometer were also measured with the Molspin magnetometer to check for consistency between the two instruments. The base level of the 2-G SQUID magnetometer is measured to be on the order of 0.0001 A/m.

2-G SQUID Magnetometer

The shipboard 2-G SQUID magnetometer is currently configured to measure up to seven discrete samples (each sample was separated from its nearest neighbor by 20 cm) on a 150-cm-long sample tray. However, the magnetometer averages over a 20-cm region. Thus, strongly magnetized samples (such as basalt) can influence adjacent samples measured on the 2-G SQUID if they are not separated by a sufficient space. To test this effect, background measurements were made on the sample pass-through track and compared against empty sample spaces 10, 20, 30, and 40 cm away from a strongly magnetized test sample. We found that a 40-cm space between discrete samples on the pass-through sample tray was required to avoid spurious signals introduced by adjacent samples. This spacing allowed four samples to be measured at a time.

Strongly magnetized samples may also influence the SQUID electronics, causing flux jumps that bias data recording. To avoid flux jumps resulting from samples with very strong magnetizations (>15 A/m intensity), the velocity of the track as it passes through the sensor coils was reduced from 25 to 5 cm/s.

Molspin Minispin Magnetometer

Standard samples of known magnetization from the University of Rochester were used to calibrate the Molspin Minispin magnetometer. Short spins (corresponding to 24 revolutions, for which the output signal is integrated) in four positions were used to obtain one magnetization measurement using the Molspin magnetometer. After calibration, the values of magnetization intensity, declination, and inclination for the standards and several test samples were in good agreement (within 5%) with the values obtained using the 2-G SQUID magnetometer. The background level for the Molspin magnetometer was found to be ~ 0.001 A/m.

Bartington/KLY-2 Kappabridge Susceptibility Meters

Both the Bartington susceptibility meter and the KLY-2 Kappabridge susceptibility meter were used for low-field susceptibility measurements, whereas only the Kappabridge was used for anisotropy of magnetic susceptibility measurements. The KLY-2 Kappabridge was calibrated using a standard sample of known susceptibility. To check the accuracy of the Bartington susceptibility meter, we measured susceptibilities of a few samples using the Kappabridge and compared them to the values given by the Bartington susceptibility meter. We found that the Bartington susceptibility meter gives susceptibility values in fairly good agreement (within 5%–10%) with the values measured using the Kappabridge.

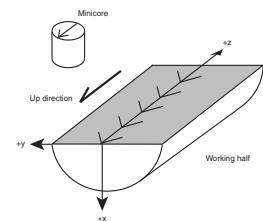
Sampling Coordinates and Sampling

The standard ODP core orientation convention (Shipboard Scientific Party, 1991, fig. 8; Shipboard Scientific Party, 1997a, fig. 8) was applied for paleomagnetic work during Leg 197 (Fig. F21). This convention is as follows: the z-axis of the sample is downhole parallel to the z-axis of the drill core. The split face of the drill core represents the y-z plane. The x-axis is then the line perpendicular to the split face (y-z plane) and is directed into the working half of the core. The x-axis is used as the reference for the relative definition of the remanence vector. Discrete samples were taken from sediment and basalt rocks by drilling cylindrical minicores (10 cm³) with a water-cooled drill bit attached to a standard drill press. Minicores were oriented with an arrow on the split face (y-z plane) pointing in the uphole direction ($-z$).

Measurement and Analysis

Discrete samples were demagnetized using alternating fields ranging from 0 to 80 mT at 5-mT steps for the first 50 mT and then at 10-mT steps for the remaining treatments to isolate stable remanence components in the samples for Sites 1203 and 1204. For Sites 1205 and 1206, samples were demagnetized at 5-mT steps for the first 70 mT and then at 10-mT steps for remaining treatments. The stability of remanence

F21. Magnetic direction convention, p. 69.



was determined using orthogonal vector plots (Zijderveld, 1967) and equal-area projections, and ChRM directions were obtained using principal component analysis (Kirschvink, 1980). Four to six discrete mini-core samples were drilled from each basalt cooling unit to evaluate intraflow directional stability.

ChRM inclinations for each basalt unit were averaged using the method of McFadden and Reid (1982). This approach utilizes a maximum likelihood estimate to limit bias in inclination averages. The general solution for the maximum likelihood estimate is dependent on the assumption that the inclinations examined are drawn from a Fisher distribution (Fisher, 1953) defined by:

$$P(\theta, \phi) d\theta d\phi = (\kappa/4\pi \sin h \kappa) \exp(\kappa \cdot \cos \theta) (\sin \theta) d\theta d\phi,$$

where,

- $P(\theta, \phi) d\theta d\phi$ = Fisher probability density function,
- κ = precision parameter,
- θ = polar angle between an observation and the true mean direction, and
- ϕ = uniformly distributed azimuthal angle about the true mean direction.

ChRM inclination values from each independent inclination group were averaged (McFadden and Reid, 1982) to obtain an overall site inclination. The best estimate of the dispersion parameter (k) was used to estimate directional angular dispersion (s) as follows (Butler, 1992):

$$s^2 = 6561/k.$$

Estimates of directional angular dispersion were further transformed into estimates of pole dispersion (S) using the numerical values of Cox (1970). Values of S allowed us to compare our data with global paleomagnetic data sets derived from lavas to assess the averaging of secular variation in the recovered basalt sequences. We note, however, that we have made no attempt to adjust S for inclination dispersion within each basalt flow in our preliminary analysis. We utilized the reference curves of McFadden et al. (1991), which describe virtual geomagnetic pole scatter in terms of primary (S_p) and secondary (S_s) geodynamo families:

$$S = \text{SQR}(S_p^2 + S_s^2).$$

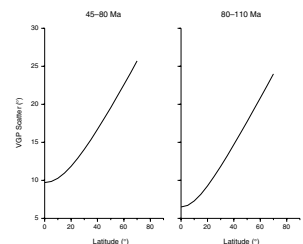
The 43- to 81-Ma time interval was of interest for the drill sites analyzed. For the 45- to 80-Ma interval, $S_s = 9.7^\circ \pm 1.5^\circ$ and $S_p/\lambda = 0.34 \pm 0.03$, where λ is the paleolatitude. For the 80- to 110-Ma interval, $S_s = 6.5^\circ (+2.9^\circ/-4.2^\circ)$ and $S_p/\lambda = 0.33 \pm 0.05$ (Fig. F22). Paleolatitudes for each site were calculated from the geocentric dipole relationship:

$$\tan I = 2 \tan \lambda,$$

where I is the average of the inclination groups.

Bulk magnetic susceptibility data and NRM intensities were used to calculate the ratio of remanent to induced magnetization, or Koenigsberger ratio (Q):

F22. Expected VGP scatter with latitude, p. 70.



$$Q = M_{nr}/K \cdot H,$$

where,

- M_{nr} = NRM intensity,
- K = volume-normalized low-field susceptibility, and
- H = present-day Earth's magnetic field strength at the site studied based on the 1995 International Geomagnetic Reference Field (Barton et al., 1995) (Koko Seamount = ~39.5 mT [31.4 A/m]; Detroit Seamount = ~48.8 mT [38.8 A/m]).

The calculated Koenigsberger ratios provide important input into the interpretation of magnetic logging of the basalt sections (see “**Down-hole Measurements,**” p. 31).

Rock magnetic properties, through the use of Lowrie-Fuller tests (Lowrie and Fuller, 1971) and coercivity of remanence, were also measured to assess magnetic domain state and magnetic hardness. The Lowrie-Fuller test can be used as a rapid determination of domain state in igneous rocks. It is based on the observation that multidomain grains require a larger destructive field to demagnetize a thermoremanent magnetization (TRM) acquired in a strong field. A laboratory-induced saturation remanent magnetization (SIRM) acquired in a 0.8-T field using an IM-10 impulse magnetizer represents the strong-field TRM. The demagnetization of the SIRM is compared with the demagnetization of a weak-field TRM, here represented by an anhysteretic remanent magnetization produced by demagnetizing the sample in a 140-mT alternating field in the presence of a 30-mT direct-current (DC) field. AF demagnetizations were done with the D-2000 AF demagnetizer, and all remanences were measured with the shipboard Molspin Minispin magnetometer.

Isothermal remanent magnetization (IRM) acquisition and backfield IRM acquisition were measured to derive coercivity of remanence, an estimate of magnetic hardness. Stepwise IRMs were imparted in the +x direction (sample coordinates) using an IM-10 impulse magnetizer until the saturation remanence (M_{rs}) was reached. Then the samples were DC demagnetized by giving them a stepwise IRM in the -x direction. The remanence decreases to zero at the coercivity of remanence (H_{cr}) and culminates in $-M_{rs}$, the negative saturation remanence.

In addition to the paleomagnetic and rock magnetic study of basalt, volcanoclastic, and sedimentary minicores, magnetozones were defined on the rotary-cored consolidated sediment units. Polarities of core samples were determined on the basis of consistent ChRM directions obtained from a >10-cm-long portion of core, either using archive halves or discrete samples. The magnetic polarity stratigraphy was then interpreted using constraints from the biostratigraphic data (see “**Biostratigraphy,**” p. 9). The numerical ages of Cande and Kent (1995) were adopted (Table T9; Fig. F23).

PHYSICAL PROPERTIES

Shipboard measurements of physical properties can be used to provide an initial look at variations in the recovered core material that may be used to characterize lithologic units, correlate with downhole geophysical logging data, and interpret seismic reflection data. After the

T9. Ages for normal polarity magnetic chrons, p. 85.

F23. Geomagnetic timescale, p. 71.



cores had attained room temperature, nondestructive tests of the unsplit core sections were made with the MST. Next, whole-round hard rock cores were scanned using the Deutsche Montan Technologie (DMT) Digital Color CoreScan. After splitting the cores, additional measurements were made of *P*-wave velocity on split cores of soft sediment samples and on discrete samples of hard rock. Bulk density, grain density, porosity, and water content were calculated from index properties measurements on discrete samples. Thermal conductivity measurements were also made on unsplit sediment cores and split hard rock cores. The instruments and apparatus used during Leg 197 are discussed in Blum (1997) and are outlined below.

Multisensor Track Measurements

The MST consists of four physical properties sensors on an automated track that measure magnetic susceptibility, bulk density, compressional wave velocity, and natural gamma ray emissions on whole-round core sections. During Leg 197, magnetic susceptibility and gamma ray attenuation (GRA) bulk density were measured on soft sediment cores and natural gamma ray measurements were made on both sediment and hard rock cores; the compressional wave logger was not used, as the rotary core barrel cores did not fill the core liner.

Magnetic Susceptibility

Magnetic susceptibility was measured on most sediment sections at 5-cm intervals using the 1.0 range (1-s integration time) on the Bartington meter (model MS2C), which has an 88-mm coil diameter. Magnetic susceptibility was not measured on hard rock cores. The magnetic susceptibility data aid in detecting variations in magnetic properties caused by lithologic changes or alteration. The quality of the magnetic susceptibility measurement is somewhat limited in sedimentary cores if they are disturbed. However, general trends may still be useful for correlation with geophysical logging data.

Gamma Ray Attenuation

The GRA densitometer estimates bulk densities on unsplit core sections using a sampling period of 5 s every 5 cm. GRA data are most reliable in undisturbed cores and can often be directly correlated with the downhole density logs. In hard rock core sections, GRA acquisition was turned off. In disturbed soft sediment cores, GRA density would be expected to have lower values.

Natural Gamma Ray Emissions

Natural gamma ray (NGR) emissions result from the decay of radioactive atoms and were measured in the laboratory by scintillation detectors as described by Hoppie et al. (1994). During Leg 197, NGR measurements were made at intervals of 10 cm for a period of 20 s on soft sediment and for a period of 60 s on hard rock cores. Results were output in counts per second, which can then be compared qualitatively with the downhole logging data. The NGR was calibrated using a thorium source.

Core Imaging

The whole-round basalt cores were scanned using the DMT Digital Color CoreScan after they had been run through the MST. This had three main objectives:

1. To provide a comprehensive suite of 360° unrolled digital core images,
2. To identify and measure planar features on the unrolled images for comparison with core structural analysis and integration with geographically orientated FMS images, and
3. To correlate and ultimately reorient core images and structural data to true geographic north using the general purpose inclinometer tool (GPIT) data on the FMS tool string.

These data offer the potential to derive paleomagnetic declination data from the otherwise azimuthally unoriented basalt cores. Such declination data could contribute significantly to the tests of hotspot fixity central to Leg 197.

The DMT Color CoreScan system is a portable core imaging device that was previously used on board the *JOIDES Resolution* during Legs 173 (Whitmarsh, Beslier, Wallace, et al., 1998) and 176 (Dick, Natland, Miller, et al., 1999). Images are recorded on whole-round outer core surfaces using a charge coupled device line-scan camera, which has a resolution of 5184 pixels/m and a spectral response of between 400 and 700 nm (DMT, 1996).

The whole-round core is rotated 360° around its cylindrical axis with the line-scan camera positioned parallel to the axis of rotation. The unrolled images are recorded in 33-cm sections that can be integrated into 1-m sections using the DigiCore software. The whole-round cores are scanned at a rate of ~1.20 min/m, creating a ~14-MB bitmap file (DMT, 1996).

During Leg 197, all core pieces that could be rotated cleanly through 360° were scanned in unrolled mode. Pieces that were not fully cylindrical or intervals of drilling breccia were not imaged, but the lengths of these intervals were measured so that allowance could be made for them when integrated into core barrel lengths using the DMT CoreLog software (DMT, 1996). The vertical line marked on the core with a red grease pencil allows an initial reorientation of the core images back to the ODP reference frame. Initial structural analyses were performed; however, the majority of the structural analysis, core-log integration, and core reorientation work was done postcruise.

Thermal Conductivity

Thermal conductivities were measured on unconsolidated sediment and rock samples using the TK04 system as described by Blum (1997). These measurements are used along with temperature measurements to estimate heat flow. The system uses a single-needle probe (von Herzen and Maxwell, 1959) heated continuously in full-space mode for soft sediment samples and in half-space configuration for hard rock samples (Vacquier, 1985). For full-core soft-sediment sections, a hole was drilled in the outer core liner and a 2-mm temperature probe was inserted into the working half of the core section. For hard rock samples, a half-space needle probe was secured on ~10-cm split-core sections that had been immersed in a water bath for at least 15 min. The thermal conductivity

measurement for each sample was the average of three repeat measurements for the full-space method and four repeat measurements for the half-space method. All results are in units of watts per meter per degree Kelvin.

Index Properties Measurements

Samples of ~10 cm³ were collected from the fresh sediment cores at a frequency of one per section to allow for determination of index properties. Samples were taken from undisturbed parts of the core, if possible. Wet sediment mass was measured immediately after the samples were collected. Dry sediment mass and dry sediment volume were determined after the samples had been dried in a convection oven for 24 hr at a temperature of 100°–110°C. Wet and dry masses were measured with two Scientech electronic balances that compensate for the ship's motion; dry volume was determined with a helium-displacement Quantachrome penta-pycnometer. For hard rock sections, rubble fragments and chips left after cutting of paleomagnetism minicore samples were collected at a frequency of approximately one per core. The samples were soaked in seawater for 24 hr, then index properties were measured using the same procedure as for the sediment sections.

Grain density, moisture content, bulk density, and porosity were calculated from wet and dry mass and dry volume as discussed by Blum (1997), who also gives values of seawater density, seawater salt density, and seawater salinity used in the calculation. Grain density (ρ_g) can be calculated from the measurements of dry mass (M_d) and dry volume (V_d). Both of these values need to be corrected to take into account the salt content of the pore fluid:

$$\rho_g = (M_d - M_s) / [V_d - (M_s / \rho_s)],$$

where,

ρ_s = salt density (2.257 g/cm³) and
 M_s = the mass of salt in the pore fluid.

The uncorrected water mass is taken as the difference between the total (water saturated) mass (M_t) and dry mass (M_d). The measured wet and dry masses are corrected for salt content using a pore water salinity (r) of 0.35% (Boyce, 1976). The wet and dry moisture contents are calculated by

$$W_d (\% \text{ dry mass}) = [(M_t - M_d) / (M_d - rM_t)] \times 100, \text{ and}$$

$$W_w (\% \text{ wet mass}) = [(M_t - M_d) / (1 - r)M_t] \times 100.$$

The bulk density (ρ_b) is the density of the saturated sample is

$$\rho_b = M_t / V_t,$$

where V_t = the total sample volume.

Porosity (ϕ) can be calculated from fluid density, grain density, and bulk density of the sample and is the ratio of pore water volume to total volume:

$$\phi = [(\rho_g - \rho_b)/(\rho_g - \rho_w)] \times 100,$$

where ρ_w = the density of the pore fluid (seawater).

Velocity Determinations

For sediment sections, velocity determinations were made by the PWS3 contact probe system. The system was used to measure *P*-wave velocities in the *x*-direction of each sample (i.e., perpendicular to the core axis) (see “Paleomagnetism and Rock Magnetism,” p. 23, for a detailed description of sampling coordinates). In hard rock, velocity determinations in the *x*-direction were made on the minicores drilled for paleomagnetic measurements. *P*-wave velocities in the *y*- and *z*-directions were also measured on selected minicores.

DOWNHOLE MEASUREMENTS

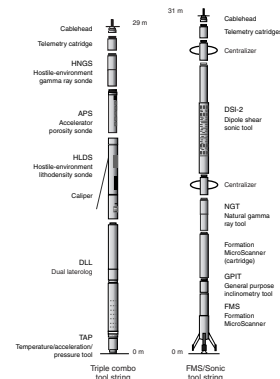
Downhole logs are continuous and in situ records of physical and structural properties of the formation penetrated by a borehole. The logs are made using a variety of probes, combined into several tool strings (Fig. F24). These strings are lowered down the hole on heave-compensated electrical wireline and then pulled up at constant speed to provide continuous measurements as a function of depth of several properties simultaneously.

Downhole logging was used during Leg 197 to address issues concerning core reorientation and volcanic stratigraphy and morphology. Whereas core recovery is often biased and incomplete in variable lithology such as alternating pillows and massive flows, logging data are continuous and therefore provide useful information over intervals of low core recovery. During Leg 197, we were particularly interested in determining the number of flow units, which has implications for how well geomagnetic secular variation has been sampled and, hence, how well paleomagnetic paleolatitudes can be constrained. Logging data were used to create synthetic seismograms, which then led to improved correlation between the seismic records and the lithologic units recovered from the boreholes. Moreover, to achieve these objectives, the logging plans also included a three-component fluxgate magnetometer and magnetic susceptibility tool. In comparison to core analysis, magnetic borehole logging yields a dense vertical profile of magnetic variations. A disadvantage of three-component magnetic logging is the lack of horizontal orientation because the tool spins around its *z*-axis during a log run. Consequently, only the strength of the horizontal magnetic field can be routinely obtained. In a strongly magnetized formation, resolution of the direction of the spinning horizontal components is poor. Therefore, information about the declination at depth remains inaccessible. If the orientation of the horizontal components of the magnetic field during the log run could be referred to a fixed reference system (geographic system or Global Positioning System [GPS]), it would allow us to resolve the horizontal field into its components and to constrain magnetic declination.

Logging Tool Strings

The tool strings planned for Leg 197 were

F24. Triple combo and FMS/sonic tool strings, p. 72.



1. The triple combination (triple combo) tool string (resistivity, density, and porosity) (Fig. F24), which consists of the accelerator porosity sonde (APS), the hostile-environment natural gamma sonde (HNGS), the high-temperature lithodensity tool (HLDT), and the dual laterolog (DLL). The Lamont-Doherty Earth Observatory (LDEO) temperature/acceleration/pressure (TAP) tool was attached to the bottom of the tool string.
2. The FMS/sonic tool string (Figs. F24, F25), which consists of the FMS, the GPIT, a dipole shear sonic imager (DSI), and the natural gamma tool (NGT). This last tool was included between the DSI and part of the FMS.
3. The three-component fluxgate magnetometer: Goettingen Borehole Magnetometer (GBM).
4. The magnetic susceptibility tool: SUSLOG 403-D.

Each tool string includes a telemetry cartridge for communicating through the wireline with the logging laboratory on the drill ship and a natural gamma ray sonde, which is used to identify lithologic markers, providing a common reference for correlation and depth between multiple logging runs.

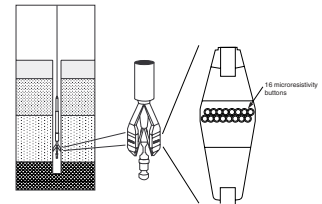
In the following sections, the basic principles of the tools and types of measurements are summarized. The principal data provided by the tools, their physical significance, and units of measure are listed in Table T10. The operating principles, applications, and approximate vertical resolution of the tools are summarized in Table T11. More information on individual tools and their geological applications may be found in Ellis (1987), Goldberg (1997), Rider (1996), Schlumberger (1989, 1994), Serra (1984, 1986, 1989), and on the LDEO Borehole Research Group (BRG) World Wide Web site (<http://www.ldeo.columbia.edu/BRG/>).

Natural Radioactivity

Two spectral gamma ray tools were used to measure and classify natural radioactivity in the formation: the HNGS and the NGT. The NGT uses a sodium iodide scintillation detector and five-window spectroscopy to determine concentrations of K (in weight percent), Th (in parts per million), and U (in parts per million), the three elements whose isotopes dominate the natural radiation spectrum. The HNGS is similar to the NGT, but it uses two bismuth germanate scintillation detectors and 256-window spectroscopy, which significantly improves the tool precision. Spectral analysis in the HNGS filters out gamma ray energies below 500 keV, eliminating sensitivity to bentonite or potassium chloride in the drilling mud and improving measurement accuracy. Because the NGT response is sensitive to borehole diameter and the weight and concentration of bentonite or potassium chloride present in the drilling mud, corrections are routinely made to diminish these effects during processing at LDEO.

For both tools, gamma ray values are measured in American Petroleum Institute (API) units. These units are derived from the primary Schlumberger calibration test facility in Houston, Texas, where a calibration standard is used to normalize each tool.

F25. Schematic diagram of the FMS, p. 73.



T10. Application of logging tools, p. 86.

T11. Acronyms and units of logging tools, p. 87.

Density

Formation density was determined from the density of electrons in the formation, which was measured with the HLDS. The sonde contains a radioactive cesium (^{137}Cs) gamma ray source (622 keV) and far- and near-gamma ray detectors mounted on a shielded skid, which is pressed against the borehole wall by a hydraulically activated eccentricizing arm. Gamma rays emitted by the source experience Compton scattering, which involves the transfer of energy from gamma rays to the electrons in the formation via elastic collision. The number of scattered gamma rays that reach the detectors is directly related to the number of electrons in the formation, which is in turn related to bulk density. Porosity may also be derived from this bulk density if the matrix density is known.

The HLDS also measures the photoelectric effect factor (PEF) caused by absorption of low-energy gamma rays. Photoelectric absorption occurs when gamma rays reach <150 keV after being repeatedly scattered by electrons in the formation. Photoelectric absorption is strongly dependent on the atomic number of the constituents of the formation; it varies according to the chemical composition and is essentially independent of porosity. For example, the PEF of pure calcite = 5.08 b/e⁻, illite = 3.03 b/e⁻, quartz = 1.81 b/e⁻, and kaolinite = 1.49 b/e⁻. PEF values can be used in combination with NGT curves to identify different types of clay minerals. The PEF values, therefore, can give an indication of the chemical composition of the rock. Coupling between the tool and borehole wall is essential for good HLDS logs. Poor contact results in underestimation of density values.

Porosity

Formation porosity was measured with the APS. The sonde incorporates a minitron neutron generator, which produces fast (14.4 MeV) neutrons, and five neutron detectors (four epithermal and one thermal) positioned at different spacings. The tool is pressed against the borehole wall by an eccentricizing bow spring. Emitted neutrons are slowed by collisions. The amount of energy lost per collision depends on the relative mass of the nucleus with which the neutron collides. The greatest energy loss occurs when the neutron strikes a nucleus nearly equal to its own mass, such as hydrogen, which is mainly present in the pore water. The neutron detectors record both the numbers of neutrons arriving at various distances from the source and neutron arrival times, which act as a measure of formation porosity. However, as hydrogen bound in minerals such as clay or in hydrocarbons also contributes to the measurement, the raw porosity value is often an overestimate.

Temperature, Acceleration, and Pressure

Downhole temperature, acceleration, and pressure were measured with the LDEO high-resolution TAP tool. When attached to the bottom of the triple combo string, the TAP tool operates in an autonomous mode, with data stored in built-in memory. A two-component thermistor (for different temperature ranges) is mounted near the bottom of the tool in the slotted protective cover. The time constant of the thermistor assembly in the water is ~ 0.4 s. The tool includes a pressure transducer (0–10,000 psi), which is used to activate the tool at a specified depth and perform pressure measurements. The TAP tool also in-

corporates a high-sensitivity vertical accelerometer, which provides data for analyzing the effects of heave on a deployed tool string, and an internal temperature sensor for monitoring the temperature inside the electronic cartridge. Temperature and pressure data are recorded once per second, and accelerometer data can be recorded at a 4- or 8-Hz sampling rate.

The borehole temperature record provides information on the thermal regime of the surrounding formation. The vertical heat flow can be estimated from the vertical temperature gradient combined with measurements of the thermal conductivity from core samples. The temperature record must be interpreted with caution, as the amount of time elapsed between the end of drilling and the logging operation is generally not sufficient to allow the borehole to recover thermally from the influence of drilling fluid circulation. The data recorded under such circumstances may differ significantly from the thermal equilibrium of that environment. Nevertheless, from the spatial temperature gradient it is possible to identify abrupt temperature changes that may represent localized fluid flow into the borehole, indicative of fluid pathways and fracturing, and/or breaks in the temperature gradient that may correspond to contrasts in permeability at lithologic boundaries.

Acoustic Measurements

Sonic velocities were measured with the DSI tool, which employs a combination of monopole and dipole transducers to make accurate measurements of sonic wave propagation in a wide variety of lithologies (Schlumberger, 1995). The DSI measures the transit times between sonic transmitters and an array of eight receivers. It averages replicate measurements, providing a direct measurement of sound velocity through formation that is relatively free from the effects of formation damage and enlarged borehole (Schlumberger, 1989). Along with the monopole transmitters found on most sonic tools, it also has two crossed dipole transmitters. The DSI excites a flexural mode in the borehole, which can be used to determine shear wave velocity in all types of formations. The configuration of the DSI also allows recording of cross-line dipole waveforms, which can be used to estimate shear wave splitting caused by preferred mineral and/or structural orientations in consolidated formations. A low-frequency source enables Stoneley waveforms to be acquired as well. These "guided" waves are associated with the solid/fluid boundary at the borehole wall, and their amplitude exponentially decays away from the boundary in both the fluid and the formation.

In addition, information such as mode amplitudes, shear wave polarization, and Poisson's ratio can be extracted postcruise to provide information about lithology, porosity, and anisotropy. Amplitude processing and stacking of Stoneley wave reflections may also be used to identify fractures, fracture permeability, and aperture in the vicinity of the borehole. The DSI tool is particularly important for measuring shear wave velocities of the upper parts of the basalt flow units.

Magnetic Field Measurement

Downhole magnetic field measurements were made with the GPIT. The GPIT is used in combination with the FMS. The primary purpose of this sonde, which incorporates a three-component accelerometer and a three-component magnetometer, is to determine the acceleration and

orientation of the FMS/sonic tool string during logging. The acceleration data allow more precise determination of log depths than is possible on the basis of cable length alone, as the wireline is subject to both stretching and ship heave. Acceleration data are also used in processing of FMS data to correct the images for irregular tool motion.

Local magnetic anomalies, generated by high remanent magnetization of the basalt in the basement section of a borehole, can interfere with the determination of tool orientation. However, these magnetic anomalies can be useful for constraining the magnetic stratigraphy of the basement section.

Electrical Resistivity Measurements

The DLL provides two resistivity measurements with different depths of investigation: deep (LLD) and shallow (LLS). In both devices, a 61-cm-thick current beam is forced horizontally into the formation by using focusing (also called bucking) currents. Two monitoring electrodes are part of the loop that adjusts the focusing currents so that no current flows in the borehole between the two electrodes. For the LLD measurements, both measuring and focusing currents return to a remote electrode on the surface; this configuration greatly improves the depth of investigations and reduces the effect of borehole and adjacent formation conductivity. In the LLS, the return electrodes that measure the focusing currents are located on the sonde, and therefore the current sheet retains focus over a shorter distance than the LLD. Because of high resistivity expected in an igneous environment, the DLL is recommended, as the tool response ranges from 0.2 to 40,000 Ωm .

Fracture porosity can be estimated from the separation between the LLD and LLS measurements, based on the observation that the former is sensitive to the presence of horizontal conductive fractures only, whereas the latter responds to both horizontal and vertical conductive structures. Because the solid constituents of rocks are essentially infinitely resistive relative to the pore fluids, resistivity is controlled mainly by the nature of the pore fluids, porosity, and permeability. In most rocks, electrical conduction occurs primarily by ion transport through pore fluids and is strongly dependent on porosity. Electrical resistivity data can therefore be used to estimate formation porosity using Archie's Law (Archie, 1942) if the formation does not contain clay. Archie's Law is expressed as

$$FF = a \cdot f^{-m},$$

where,

FF = formation factor (i.e., the ratio of the formation resistivity to that of the pore fluids),

f = porosity,

m = cementation factor, which is dependent on the tortuosity and connectivity of pore spaces, and

a = a constant that varies with rock type.

Electrical Images: Formation MicroScanner

The FMS provides high-resolution electrical resistivity-based images of borehole walls (Figs. F24, F25). The tool has four orthogonal arms

(pads), each containing 16 microelectrodes, or “buttons,” which are pressed against the borehole wall during the recording. The electrodes are arranged in two diagonally offset rows of eight electrodes each and are spaced ~2.5 mm apart. A focused current is emitted from the four pads into the formation, with a return electrode near the top of the tool. Array buttons on each of the pads measure the current intensity variations. The FMS image is sensitive to structure within ~25 cm of the borehole wall and has a vertical resolution of 5 mm with a coverage of 22% of the borehole wall on a given pass. FMS logging commonly includes two passes, the images of which are merged to improve borehole wall coverage. To produce reliable FMS images, however, the pads must be firmly pressed against the borehole wall. In holes with a diameter >15 in, the pad contact will be inconsistent and the FMS images can be blurred. The maximum borehole deviation where good data can be recorded with this tool is 10°. Irregular borehole walls will also adversely affect the images, as contact with the wall is poor. FMS images are oriented to magnetic north using the GPIT (see “[Magnetic Field Measurement](#),” p. 34). Processing transforms these measurements of the microresistivity variations of the formation into continuous, spatially oriented, and high-resolution images that mimic geologic structures behind the borehole walls. Further processing can provide measurements of dip and direction (azimuth) of planar features in the formation. FMS images are particularly useful for mapping structural features, dip determination, detailed core-log correlation, and positioning of core sections with poor recovery. This allows the dip and azimuth of geological features intersecting the hole to be measured from the processed FMS image. FMS images can be used to visually compare logs with core to ascertain the orientations of bedding, fracture patterns, and sedimentary structures. FMS images have proved to be particularly valuable in the interpretation of sedimentary structures and for constraining volcanic stratigraphy during previous ODP legs (Ayadi et al., 1998; Brewer et al., 1999). Detailed interpretation of FMS images in combination with other log data and core imaging will be carried out postcruise.

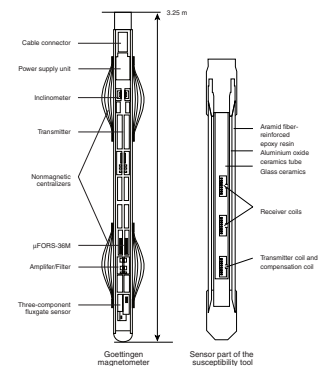
The Goettingen Borehole Magnetometer

The GBM tool was designed and developed in 1989 by the Geophysical Institute of the University of Goettingen, Germany (Fig. F26). The original application was to continuously monitor magnetic field variations in a borehole for several weeks and to compare these with field variations at depth (Steveling et al., 1991). The maximum operation pressure and temperature is 70 MPa and 100°C, respectively. The tool consists of three fluxgate sensors that log the horizontal (x and y) and the vertical (z) components of the magnetic flux density. The tool is equipped with an angular rate sensor to monitor the spin history around the z-axis and variations around the x- and y-axis during a log run. The tool connects directly to the Schlumberger cable head. Centralizers can be optionally applied. The housing is made of low-magnetic monel and is not affected by pressure and temperature up to 70 MPa at 100°C, respectively. Specifications are listed in Table T12.

Angular Rate Sensor

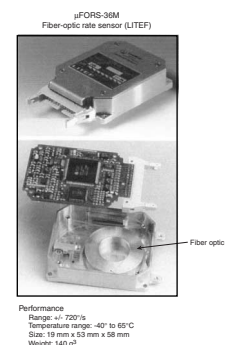
The LITEF miniature fiber-optic rate sensor (μFORS) provides angular rate output. It has a small volume and low weight and requires little power (2 VA) (Fig. F27). Free from gravity-induced errors and with no

F26. The GBM and the sensor of the magnetic susceptibility tool, p. 74.



T12. Goettingen Borehole Magnetometer specifications, p. 88.

F27. Specifications of the fiber-optic rate sensor, p. 75.



moving parts, the sensor is insensitive to shock and vibration. The rate sensor is an unconventional gyro, since it does not have a spinning wheel. It detects and measures angular rates by measuring the frequency difference between two contra-rotating light beams. The light source is a superluminescent diode. Its broad spectrum provides light with short coherence length to keep the undesirable backscattering effects in the optical path to sufficiently low levels. The beam is polarized, split, and phase modulated. The output light travels through a 110-m-long fiber coil. The light travels to the detector, which converts the light into an electronic output signal. When the gyro is at rest, the two beams have identical frequencies. When the gyro is subjected to an angular turning rate around an axis perpendicular to the plane of the two beams, one beam then has a greater optical path length and the other beam has a shorter optical path length (Fig. F27). Therefore, the two resonant frequencies change and the frequency differential is measured by optical means, resulting in a digital output. Readings are output at 1 Hz. The angular rate is a function of time sampled with 5 Hz and the accumulated angle. The angular rate measured by the sensor is influenced by the Earth's rotation, which depends on the latitude (ϕ) and varies from 15.04°/hr at the poles to 0°/hr at the equator (Fig. F28). From equator to pole, Earth's measured rotation increases by $\sin\phi$. To obtain the rotation rate about an inertial system, the effect of Earth's rotation must be eliminated. If the rotation rate around each axis is known, the orientation of the tool can be derived as a function of depth from the rotation history.

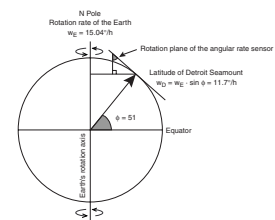
Magnetic Susceptibility: SUSLOG 403-D

The magnetic susceptibility tool (Krammer and Pohl, 1991) was previously deployed during Leg 109 (See Krammer, 1990, for Hole 395A, Mid-Atlantic Ridge). It consists of three vertically oriented coils at the lowermost part of the tool locked inside a nonconductive and nonmagnetic pressure tube (Fig. F26). This housing is made of a pressure-resistant ceramic surrounded by an elastomeric layer of silicon rubber for shock absorption and a fiberglass-reinforced epoxy resin to prevent leakage. The lowermost coil produces and transmits an alternating magnetic field with a frequency of 1000 Hz. In a second coil wound on the transmitter coil, a voltage is induced. This voltage is used to compensate that part of the receiver coil voltage that is induced in free air corresponding to the magnetic permeability (μ_0) (susceptibility = 0). The remaining voltage is preamplified by a factor of 1000 and band-pass filtered to decrease induced noise. The spacing between transmitter and receiver coil is 40 cm. Two phase-sensitive detectors, with 90° phase shift between them, convert the amplified receiver signal to two DC voltages. The in-phase part of the signal is proportional to the electrical conductivity, and the quadrature part is proportional to the magnetic susceptibility of the surrounding formation. Both parts are separated by phase detectors and are displayed separately. Table T13 summarizes the specifications of the tool, which is designed to operate under temperatures and pressures up to 60°C and 40 MPa, respectively.

Log Data Quality

The quality of log data may be seriously degraded by excessively wide sections of the borehole or by rapid changes in hole diameter. Resistivity and velocity measurements are the least sensitive to borehole effects,

F28. Dependence of the rotation rate of the Earth, p. 76.



T13. Susceptibility tool specifications, p. 89.

whereas the nuclear measurements (density, neutron porosity, and both natural and induced spectral gamma rays) are most sensitive because of the large attenuation by borehole fluid. Corrections can be applied to the original data to reduce the effects of these conditions and, generally, any departure from the conditions under which the tool was calibrated.

Logs from different tool strings may have depth mismatches, caused by either cable stretch or ship heave during recording. Small errors in depth matching can distort the logging results in zones of rapidly changing lithology. To minimize the effects of ship heave, a hydraulic wireline heave compensator adjusts for rig motion during logging operations. Distinctive features recorded by the NGT, run on every log tool string, provide calibration points and relative depth offsets among the logging runs and can be correlated with distinctive lithologic contacts observed in the core recovery or drilling penetration (e.g., basement contacts).

Data Recording and Processing

Data for each logging run were recorded, stored digitally, and monitored in real time using the Schlumberger Minimum Configuration Maxis system. On completion of logging at each hole, data were transferred to the downhole measurements laboratory for preliminary interpretation. Basic processing was then carried out to provide scientists with a comprehensive, quality-controlled downhole log data set that can be used for comparison and integration with other data collected during each ODP leg. This processing is usually conducted onshore at LDEO after the data are transmitted by satellite from the ship. It includes depth adjustments to remove depth offsets between data from different logging runs; corrections specific to certain tools and logs; documentation for the logs, with an assessment of log quality; and conversion of the data to a widely accessible format (ASCII for the conventional logs and GIF for the FMS images). Schlumberger GeoQuest's "GeoFrame" software package is used for most of the processing. Further postcruise processing of FMS log data is performed, and data are available 1 month after the cruise.

The magnetic susceptibility data recorded with the SUSLOG 403-D required several corrections. The signal depends on the borehole diameter. Variations of the borehole caliber or breakouts must be corrected. For correction, the recorded apparent susceptibility is multiplied by a factor that takes into account the borehole diameter and the deviation from the borehole axis. This correction is achieved by means of a correction chart (Krammer and Pohl, 1991). The application of the correction transforms the apparent susceptibility into a "true" susceptibility; however, it does not take into account the thickness of the layer. The vertical resolution increases with decreasing distances between transmitter and receiver coil but decreases the depth of investigation simultaneously.

Processed acoustic, caliper, density, gamma ray, magnetic, neutron porosity, resistivity, and temperature data in are available in ASCII format directly from the LDEO-BRG World Wide Web site at <http://www.ldeo.columbia.edu/BRG/ODP/DATABASE>. Access to logging data is restricted to Leg 197 participants for 12 months following the completion of the leg, and a password is required to access data during this period. Thereafter, access to these log data is openly available. A

summary of logging highlights is also posted on the LDEO-BRG web site at the end of each leg.

UNDERWAY AND SITE GEOPHYSICS

During Leg 197, seismic data were collected to refine drill site locations and resolution of the acoustic characteristics and structure of basement rock and overlying sediment. A primary goal was to attempt to acoustically distinguish and map the lateral distribution of eruptive sequences. Underway geophysics also continued to maintain traditional ODP practice by acquiring navigational GPS, magnetometer, and 3.5- and 12-kHz echo sounder data during transits. Navigational and magnetometer data were recorded in WINFROG (version 2.62_21) on a dedicated PC-compatible computer in the underway geophysics laboratory.

Navigation

Precise navigation during Leg 197 was achieved by GPS. An Ashtech GG24 receiver was used as the primary navigation device throughout the leg, and the output was provided to the underway geophysics laboratory. GPS fixes were continuously updated at 1-s intervals and were recorded in WINFROG every 60 s while in transit and on site, except during seismic surveys, when navigational data were recorded at every firing of the water gun, typically every 4–6 s. The Generic Mapping Tools software package (Wessel and Smith, 1995) was used to process and display the navigation data using UNIX workstations.

Seismic Reflection Data

Site survey data (analog records only) from previous ODP legs (Dalrymple et al., 1980; Greene et al., 1980) and a regional marine geological study (Lonsdale et al., 1993) guided initial selection of drilling locations for Leg 197 sites. However, to refine site location and acquire digital recordings, short legs of single-channel seismic data were acquired in the vicinity of the site locations. These data were digitized, processed, and interpreted to characterize the upper 150–200 m of basement and to compare the acoustic fabric with the flow morphology and stratigraphic sequence documented by recovered cores.

The acoustic source consisted of a single 80-in³ water gun developed by Seismic System Inc. (SSI) (Hutchinson and Detrick, 1984). To maximize horizontal resolution, the SSI water gun was fired at a rate faster than typical of ODP cruises. A 60-phone, 100-m-long Teledyne oil-filled streamer recorded the water gun shots. The streamer was towed ~15 m deep, while the water gun was ~4 m deep. The streamer's midpoint was ~225 m behind the water gun. The midpoint between the water gun and the active streamer's midpoint was 188 m astern from the ship's recorded GPS position. Streamer output was split to present as real-time analog displays on EPC and LSR facsimile records and using UNIX Sun Sparc5 workstations for digitizing and recording of SEG-Y files on 4-mm DAT tape and 8-mm EXABYTE tape.

Digital data were subsequently processed using SIOSEIS software for interpretation and subsequent integration with downhole logging data. Integration was planned to include the shore-based production of synthetic seismograms for each site. Generation of the seismograms will

use the velocity and density data collected in the core laboratory by discrete physical properties measurements. Synthetic seismic sections will be band-pass filtered to have a power spectra that approximates the power spectra of the acquired data.

Magnetic Data

Because of equipment maintenance, measurement and recording of the total intensity of the Earth's magnetic field did not begin until the third day at sea at 40°06.4900'N, 149°24.6980'E. However, this unsurveyed region (off central and northern Japan) has been extensively covered by previous magnetic surveys. Measurements were taken with a Geometrics model G-886 proton precession magnetometer towed ~500 m astern. WINFROG navigation software recorded magnetic data at 60-s intervals in the ship's navigation files.

Bathymetry

High-resolution bathymetric measurements did not begin until the third day at sea at 40°06.4900'N, 149°24.6980'E. Two types of bathymetric data were recorded: one with a 3.5-kHz shallow seismic system and the other a 12-kHz echo sounder. Both systems used a Raytheon CESP III correlator echo sounder processor (CESP). The 3.5-kHz CESP was driven by an EDO transceiver with a single-element 10-kW transducer. The 12-kHz CESP was driven by a Raytheon PTR 105B transceiver with an EDO 323B 2-kW transducer. Uncorrected 3.5- and 12-kHz depths were recorded on EPC 8082 analog line-scan recorders. Uncorrected depths were read visually from the recorders every 5 min and entered into a Microsoft Excel spreadsheet by the underway technician. The line-scan recorders automatically annotated the data with ship speed and heading every 5 min and ship position every 30 min. These annotations were also logged by WINFROG. The vessel's sonar dome is located 45.5 m toward the bow from the ship's recorded GPS position.

REFERENCES

- Archie, G.E., 1942. The electrical resistivity log as an aid in determining some reservoir characteristics. *J. Pet. Technol.*, 5:1–8.
- Aubele, J.C., Crumpler, L.S., and Elston, W.E., 1988. Vesicle zonation and vertical structure of basalt flows. *J. Volcanol. Geotherm. Res.*, 35:349–374.
- Ayadi, M., Pezard, P.A., Laverne, C., and Bronner, G., 1998. Multi-scalar structure at DSDP/ODP Site 504, Costa Rica Rift, I: stratigraphy of eruptive products and accretion processes. In Harvey, P.K., and Lovell, M.A. (Eds.), *Core-Log Integration: Spec. Publ.—Geol. Soc. London*, 136:297–310.
- Ballard, R.D., and van Andel, T.H., 1979. The Galapagos Rift at 86°W: 3. Sheet flows, collapse pits and lava lakes of the rift valley. *J. Geophys. Res.*, 84:5407–5422.
- Balsam, W.L., and Damuth, J.E., 2000. Further investigations of shipboard vs. shore-based spectral data: implications for interpreting Leg 164 sediment composition. In Paull, C.K., Matsumoto, R., Wallace, P., and Dillon, W.P. (Eds.), *Proc. ODP, Sci. Results*, 164: College Station, TX (Ocean Drilling Program), 313–324.
- Balsam, W.L., Damuth, J.E., and Schneider, R.R., 1997. Comparison of shipboard vs. shore-based spectral data from Amazon-Fan cores: implications for interpreting sediment composition. In Flood, R.D., Piper, D.J.W., Klaus, A., and Peterson, L.C. (Eds.), *Proc. ODP, Sci. Results*, 155: College Station, TX (Ocean Drilling Program), 193–215.
- Balsam, W.L., Deaton, B.C., and Damuth, J.E., 1998. The effects of water content on diffuse reflectance measurements of deep-sea core samples: an example from ODP Leg 164 sediments. *Mar. Geol.*, 149:177–189.
- Barton, C.E., Baldwin, R.T., Barraclough, D.R., et al., 1995. International Geomagnetic Reference Field, 1995 revision presented by IAGA Division V, Working Group 8. *Phys. Earth Planet. Int.*, 97:23–26.
- Berggren, W.A., Kent, D.V., Swisher, C.C., III, and Aubry, M.-P., 1995. A revised Cenozoic geochronology and chronostratigraphy. In Berggren, W.A., Kent, D.V., Aubry, M.-P., and Hardenbol, J. (Eds.), *Geochronology, Time Scales and Global Stratigraphic Correlation*. Spec. Publ.—Soc. Econ. Paleontol. Mineral., 54:129–212.
- Blum, P., 1997. Physical properties handbook: a guide to the shipboard measurement of physical properties of deep-sea cores. *ODP Tech. Note*, 26 [Online]. Available from World Wide Web: <<http://www-odp.tamu.edu/publications/tnotes/tn26/INDEX.HTM>>. [Cited 2001-06-27]
- Boyce, R.E., 1976. Definitions and laboratory techniques of compressional sound velocity parameters and wet-water content, wet-bulk density, and porosity parameters by gravimetric and gamma-ray attenuation techniques. In Schlanger, S.O., Jackson, E.D., et al., *Init. Repts. DSDP*, 33: Washington (U.S. Govt. Printing Office), 931–958.
- Bralower, T.J., Leckie, R.M., Sliter, W.V., and Thierstein, H.R., 1995. An integrated Cretaceous microfossil biostratigraphy. In Berggren, W.A., Kent, D.V., Aubry, M.-P., and Hardenbol, J., (Eds.), *Geochronology, Time Scales, and Global Stratigraphic Correlation*. Spec. Publ.—Soc. Econ. Paleontol. Mineral., 54:65–79.
- Brewer, T.S., Harvey, P.K., Lovell, M.A., Haggas, S., Pezard, P.A., and Goldberg, D., 1999. Borehole images of the ocean crust: case histories from the Ocean Drilling Program. In Lovell, M.A., Williamson, and Harvey, P.K. (Eds.), *Borehole Images: Application and Case Histories: Spec. Publ.—Geol. Soc. London*, 159:283–294.
- Butler, R.F., 1992. *Paleomagnetism: Magnetic Domains to Geologic Terranes*: Boston (Blackwell).
- Cande, S.C., and Kent, D.V., 1995. Revised calibration of the geomagnetic polarity timescale for the Late Cretaceous and Cenozoic. *J. Geophys. Res.*, 100:6093–6095.
- Coffin, M.F., Frey, F.A., Wallace, P.J., et al., 2000. *Proc. ODP, Init. Repts.*, 183 [CD-ROM]. Available from: Ocean Drilling Program, Texas A&M University, College Station, TX 77845-9547, U.S.A.

- Cox, A.V., 1970. Latitude dependence of the angular dispersion of the geomagnetic field. *Geophys. J. R. Astron. Soc.*, 20:253–269.
- Crisp, J., and Baloga, S.M., 1994. Influence of crystallization and entrainment of cooler material on the emplacement of basaltic a'a flows. *J. Geophys. Res.*, 99:11819–11831.
- Crisp, J., Cashman, K.V., Bonini, J.A., Houghton, S.B., and Pieri, D.C., 1994. Crystallization history of the 1984 Mauna Loa lava flow. *J. Geophys. Res.*, 99:7177–7198.
- Dalrymple, G.B., Green, H.G., Ruppel, B.D., Bear, T.E., and Clague, D.A., 1980. Pre-Leg 55 site survey geophysical data from R/V *S.P. Lee* cruise LEE8-76-NP. In Jackson, E.D., Koizumi, I., et al., *Init Repts. DSDP*, 55: Washington (U.S. Govt. Printing Office), 801–843.
- Dick, H.J.B., Natland, J.H., Miller, D.J., et al., 1999. *Proc. ODP, Init. Repts.*, 176 [CD-ROM]. Available from: Ocean Drilling Program, Texas A&M University, College Station, TX 77845-9547, U.S.A.
- DMT-GeoTec/Geo-Engineering, 1996. *DMT Color CoreScan Users Manual. Acquisition and Evaluation Software.*
- Dunham, R.J., 1962. Classification of carbonate rocks according to depositional texture. In Ham, W.E. (Ed.), *Classification of Carbonate Rocks: AAPG Mem.*, 108–121.
- Ellis, D.V., 1987. *Well Logging for Earth Scientists*: New York (Elsevier).
- Erba, E., Premoli Silva, I., and Watkins, D.K., 1995. Cretaceous calcareous plankton biostratigraphy of Sites 872 through 879. In Haggerty, J.A., Premoli Silva, I., Rack, F., and McNutt, M.K. (Eds.), *Proc. ODP, Sci. Results*, 144: College Station, TX (Ocean Drilling Program), 157–169.
- Fisher, R.A., 1953. Dispersion on a sphere. *Proc. R. Soc. London A*, 217:295–305.
- Fisher, R.V., and Schmincke, H.-U., 1984. *Pyroclastic Rocks*: New York (Springer-Verlag).
- Fuller, R.E., 1931. The geomorphology and volcanic sequence of Steens Mountain in southeastern Oregon. *Geology*, 3:130.
- Goff, F., 1996. Vesicle cylinders in vapor-differentiated basalt flows. *J. Volcanol. Geotherm. Res.*, 97:167–185.
- Goldberg, D., 1997. The role of downhole measurements in marine geology and geophysics. *Rev. Geophys.*, 35:315–342.
- Greene, H.G., Clague, D.A., and Dalrymple, G.B., 1980. Seismic stratigraphy and vertical tectonics of the Emperor Seamounts, DSDP Leg 55. In Jackson, E.D., Koizumi, I., et al., *Init Repts. DSDP*, 55: Washington (U.S. Govt. Printing Office), 759–788.
- Gregg, T.K.P., and Fink, J.H., 1995. Quantification of submarine lava-flow morphology through analog experiments. *Geology*, 23:73–76.
- Hon, K., Kauahikaua, J.P., Denlinger, R., and Mackay, K., 1994. Emplacement and inflation of pahoehoe sheet flows: observations and measurements of active lava flows on Kilauea, Hawaii. *Geol. Soc. Am. Bull.*, 106:351–370.
- Hoppie, B.W., Blum, P., and the Shipboard Scientific Party, 1994. Natural gamma-ray measurements on ODP cores: introduction to procedures with examples from Leg 150. In Mountain, G.S., Miller, K.G., Blum, P., et al., *Proc. ODP, Init. Repts.*, 150: College Station, TX (Ocean Drilling Program), 51–59.
- Hutchinson, D.R., and Detrick, R.S., 1984. Water gun vs. air gun: a comparison. *Mar. Geophys. Res.*, 6:295–310.
- Ingram, R.L., 1954. Terminology for the thickness of stratification and parting units in sedimentary rocks. *Geol. Soc. Am. Bull.*, 65:937–938.
- Keszthelyi, L., 2002. Classification of the mafic lava flows from ODP Leg 183. *Proc. ODP, Sci. Results*, 183.
- Keszthelyi, L., McEwen, A.S., and Thordarson, T., 2000. Terrestrial analogs and thermal models for Martian flood lavas, *J. Geophys. Res.*, 105:15027–15049.
- Keszthelyi, L., and Self, S., 1998. Some physical requirements for the emplacement of long basaltic lava flows. *J. Geophys. Res.*, 103:27447–27464.

- Keszthelyi, L., and Thordarson, T., 2000. Rubbly pahoehoe: a previously undescribed but widespread lava type transitional between a'a and pahoehoe, *Geol. Soc. Am. Abstr. Progr.*, 32:7.
- Kirschvink, J.L., 1980. The least-squares line and plane and the analysis of palaeomagnetic data. *Geophys. J. R. Astron. Soc.*, 62:699–718.
- Krammer, K., 1990. Magnetic susceptibility log measured in Hole 395A, Leg 109. In Detrick, R., Honnorez, J., Bryan, W.B., Juteau, T., et al. *Proc. ODP, Sci. Results*, 106/109: College Station, TX (Ocean Drilling Program), 231–235.
- Krammer, K., and Pohl, J., 1991. New tools for measuring the magnetic susceptibility in deep drillholes. *Sci. Drilling*, 2:188–196.
- Lockwood, J.P., and Lipman, P.W., 1980. Recovery of datable charcoal beneath young lavas: lesson from Hawaii. *Bull. Volcanol.*, 43:609–615.
- Lonsdale, P., Dieu, J., and Natland, J., 1993. Posterosional volcanism in the Cretaceous part of the Hawaiian hotspot trail. *J. Geophys. Res.*, 98:4081–4098.
- Lowrie, W., and Fuller, M., 1971. On the alternating field demagnetization characteristics of multidomain thermoremanent magnetization in magnetite. *J. Geophys. Res.*, 76:6339–6349.
- Macdonald, G.A., 1953. Pahoehoe, a'a, and block lava. *Am. J. Sci.*, 251:169–191.
- , 1967. Forms and structures of extrusive basaltic rocks. *Basalts—The Poldervaart Treatise on Rocks of Basaltic Composition*: New York (Wiley-Interscience Publ.), 1:1–61.
- MacKenzie, W.S., Donaldson, C.H., and Guilford, C., 1982. *Atlas of Igneous Rocks and their Textures*: Harlow, England (Longman).
- Martini, E., 1971. Standard Tertiary and Quaternary calcareous nannoplankton zonation. In Farinacci, A. (Ed.), *Proc. 2nd Int. Conf. Planktonic Microfossils Roma*: Rome (Ed. Tecnosci.), 2:739–785.
- Mattox, T.N., Heliker, C., Kauahikaua, J., and Hon, K., 1993. Development of the 1990 Kalapana flow field, Kilauea Volcano, Hawaii. *Bull. Volcanol.*, 55:407–413.
- Mazzullo, J.M., Meyer, A., and Kidd, R.B., 1988. New sediment classification scheme for the Ocean Drilling Program. In Mazzullo, J., and Graham, A.G. (Eds.), *Handbook for Shipboard Sedimentologists. ODP Tech. Note*, 8:45–67.
- McFadden, P.L., Merrill, R.T., McElhinny, M.W., and Lee, S., 1991. Reversals of the Earth's magnetic field and temporal variations of the dynamo families. *J. Geophys. Res.*, 96:3923–3933.
- McFadden, P.L., and Reid, A.B., 1982. Analysis of paleomagnetic inclination data. *Geophys. J. R. Astron. Soc.*, 69:307–319.
- McKee, E.D., and Weir, G.W., 1953. Terminology for stratification and cross-stratification in sedimentary rocks. *Geol. Soc. Am. Bull.*, 64:381–390.
- Munsell Color Company, Inc., 1975. *Munsell Soil Color Charts*: Baltimore, MD (Munsell).
- , 1991. *Munsell Rock Color Charts*: Baltimore, MD (Munsell).
- Murray, R.W., Miller, D.J., and Kryc, K.A., 2000. Analysis of major and trace elements in rocks, sediments, and interstitial waters by inductively coupled plasma–atomic emission spectrometry (ICP-AES). *ODP Tech. Note*, 29 [Online]. Available from World Wide Web: <<http://www-odp.tamu.edu/publications/tnotes/tn29/INDEX.HTM>>. [Cited 2001-06-27]
- Okada, H., and Bukry, D., 1980. Supplementary modification and introduction of code numbers to the low-latitude coccolith biostratigraphic zonation (Bukry, 1973; 1975). *Mar. Micropaleontol.*, 5:321–325.
- Peterson, D.W., and Tilling, R.I., 1980. Transition of basaltic lava from pahoehoe to a'a, Kilauea Volcano, Hawaii: field observations and key factors. *J. Volcanol. Geotherm. Res.* 7:271–293.
- Rea, D.K., Basov, I.A., Janecek, T.R., Palmer-Julson, A., et al., 1993. *Proc. ODP, Init. Repts.*, 145: College Station, TX (Ocean Drilling Program).
- Rider, M., 1996. *The Geological Interpretation of Well Logs* (2nd ed.): Caithness (Whittles Publishing).

- Rock-Color Chart Committee, 1991. *Rock Color Chart*: Boulder, CO (Geol. Soc. Am.).
- Rothwell, R.G., 1989. *Minerals and Mineraloids in Marine Sediments: An Optical Identification Guide*: Basking, UK (Elsevier Appl. Sci. Publ.).
- Rowland, S.K., and Walker, G.P.L., 1987. Toothpaste lava: characteristics and origin of a lava structural type transitional between pahoehoe and a'a. *Bull. Volcanol.*, 49:631–641.
- Schlumberger, 1989. *Log Interpretation Principles/Applications*: Houston (Schlumberger Educ. Services), SMP-7017.
- , 1994. *IPL Integrated Porosity Lithology*: Houston (Schlumberger Wireline and Testing), SMP-9270.
- , 1995. *DSI—Dipole Sonic Imager*: Houston (Schlumberger Wireline and Testing), SMP-5128.
- Self, S., Keszthelyi, L., and Thordarson, T., 1998. The importance of pahoehoe. *Annu. Rev. Earth Planet. Sci.*, 26:81–110.
- Self, S., Thordarson, T., and Keszthelyi, L., 1997. Emplacement of continental flood basalt lava flows. In Mahoney, J.J., and Coffin, M. (Eds.), *Large Igneous Provinces: Continental, Oceanic, and Planetary Flood Volcanism*. Am. Geophys. Union., Geophys. Monogr., 100:381–410.
- Serra, O., 1984. *Fundamentals of Well-Log Interpretation (Vol. 1): The Acquisition of Logging Data*: Dev. Pet. Sci., 15A.
- , 1986. *Fundamentals of Well-Log Interpretation (Vol. 2): The Interpretation of Logging Data*. Dev. Pet. Sci., 15B.
- , 1989. *Formation MicroScanner Image Interpretation*: Houston (Schlumberger Educ. Services), SMP-7028.
- Shepard, F., 1954. Nomenclature based on sand-silt-clay ratios. *J. Sediment. Petrol.*, 24:151–158.
- Shipboard Scientific Party, 1991. Explanatory notes. In Davies, P.J., McKenzie, J.A., Palmer-Julson, A., et al., *Proc. ODP, Init. Repts.*, 133 (Pt. 1): College Station, TX (Ocean Drilling Program), 31–58.
- , 1995. Explanatory notes. In Curry, W.B., Shackleton, N.J., Richter, C., et al., *Proc. ODP, Init. Repts.*, 154: College Station, TX (Ocean Drilling Program), 11–38.
- , 1997a. Explanatory notes. In Eberli, G.P., Swart, P.K., Malone, M.J., et al., *Proc. ODP, Init. Repts.*, 166: College Station, TX (Ocean Drilling Program), 43–65.
- , 1997b. Explanatory notes. In Sigurdsson, H., Leckie, R.M., Acton, G.D., et al., *Proc. ODP, Init. Repts.*, 165: College Station, TX (Ocean Drilling Program), 15–46.
- , 2000. Explanatory notes. In Coffin, M.F., Frey, F.A., Wallace, P.J., et al., *Proc. ODP, Init. Repts.*, 183, 1–94 [CD-ROM]. Available from: Ocean Drilling Program, Texas A&M University, College Station, TX 77845-9547, U.S.A.
- , 2001. Explanatory notes. In Christie, D.M., Pedersen, R.B., Miller, D.J., et al., *Proc. ODP, Init. Repts.*, 187, 1–42 [CD-ROM]. Available from: Ocean Drilling Program, Texas A&M University, College Station TX 77845-9547, USA.
- Sissingh, W., 1977. Biostratigraphy of Cretaceous calcareous nannoplankton. *Geol. Mijnbouw*, 56:37–65.
- Stevelling, E., Spitzer, K., and Leven, M., 1991. Vertical gradient of horizontal geomagnetic variations—first results with the new Goettingen Borehole Magnetometer in the KTB-VB pilot hole. *Sci. Drilling*, 2:180–187.
- Swanson, D.A., 1973. Pahoehoe flows from the 1969–1971 Mauna Ulu eruption, Kilauea Volcano, Hawaii. *Geol. Soc. Am. Bull.*, 84:615–626.
- Tarduno, J.A., and Cottrell, R.D., 1997. Paleomagnetic evidence for motion of the Hawaiian hotspot during formation of the Emperor Seamounts. *Earth Planet. Sci. Lett.*, 153:171–180.
- Tarduno, J.A., and Sager, W.W., 1995. Polar standstill of the mid-Cretaceous Pacific plate and its geodynamic implications. *Science*, 269:956–959.

- Terry, R.D., and Chilingar, G.V., 1955. Summary of "Concerning some additional aids in studying sedimentary formations" by M. S. Shvetsov. *J. Sediment. Petrol.*, 25:229–234.
- Thordarson, T., 1995. Volatile release and atmospheric effects of basaltic fissure eruptions [Ph.D. thesis]. Univ. of Hawaii at Manoa, Honolulu.
- , 2000. Preliminary report: physical volcanology of lava flows on Surtsey, Iceland. *Surtsey Res. Progr. Rept.*, XI:125–142.
- Thordarson, T., and Self, S., 1993. The Laki (Skaftár Fires) and Grímsvötn eruptions in 1783–85. *Bull. Volcanol.*, 55:233–26.
- , 1998. The Roza Member, Columbia River Basalt Group—a gigantic pahoehoe lava flow field formed by endogenous processes. *J. Geophys. Res.*, 103:27411–27445.
- Vacquier, V., 1985. The measurement of thermal conductivity of solids with a transient linear heat source on the plane surface of a poorly conducting body. *Earth Planet. Sci. Lett.*, 74:275–279.
- von Herzen, R.P., and Maxwell, A.E., 1959. The measurement of thermal conductivity of deep-sea sediments by a needle-probe method. *J. Geophys. Res.*, 64:1557–1563.
- Walker, G.P.L., 1991. Structure, and origin by injection of lava under surface crust, of tumuli, "lava rises," "lava-rise pits," and "lava-inflation clefts" in Hawaii. *Bull. Volcanol.*, 53:546–558.
- Wentworth, C.K., 1922. A scale of grade and class terms of clastic sediments. *J. Geol.*, 30:377–392.
- Wessel, P., and Smith, W.H.F., 1995. New version of the Generic Mapping Tools released. *Eos*, 76:329.
- Whitmarsh, R.B., Beslier, M.-O., Wallace, P.J., et al., 1998. *Proc. ODP, Init. Repts.*, 173: College Station, TX (Ocean Drilling Program).
- Wilmoth, R.A., and Walker, G.P.L., 1993. P-type and S-type pahoehoe: a study of vesicle distribution patterns in Hawaiian lava flows. *J. Volcanol. Geotherm. Res.*, 55:129–142.
- Zijderveld, J.D.A., 1967. A.C. demagnetization of rocks: analysis of results. In Collinson, D.W., Creer, K.N., and Runcorn, S.K. (Eds.), *Methods in Paleomagnetism*: Amsterdam (Elsevier), 254–286.

Figure F1. Schematic examples of numbered core sections.

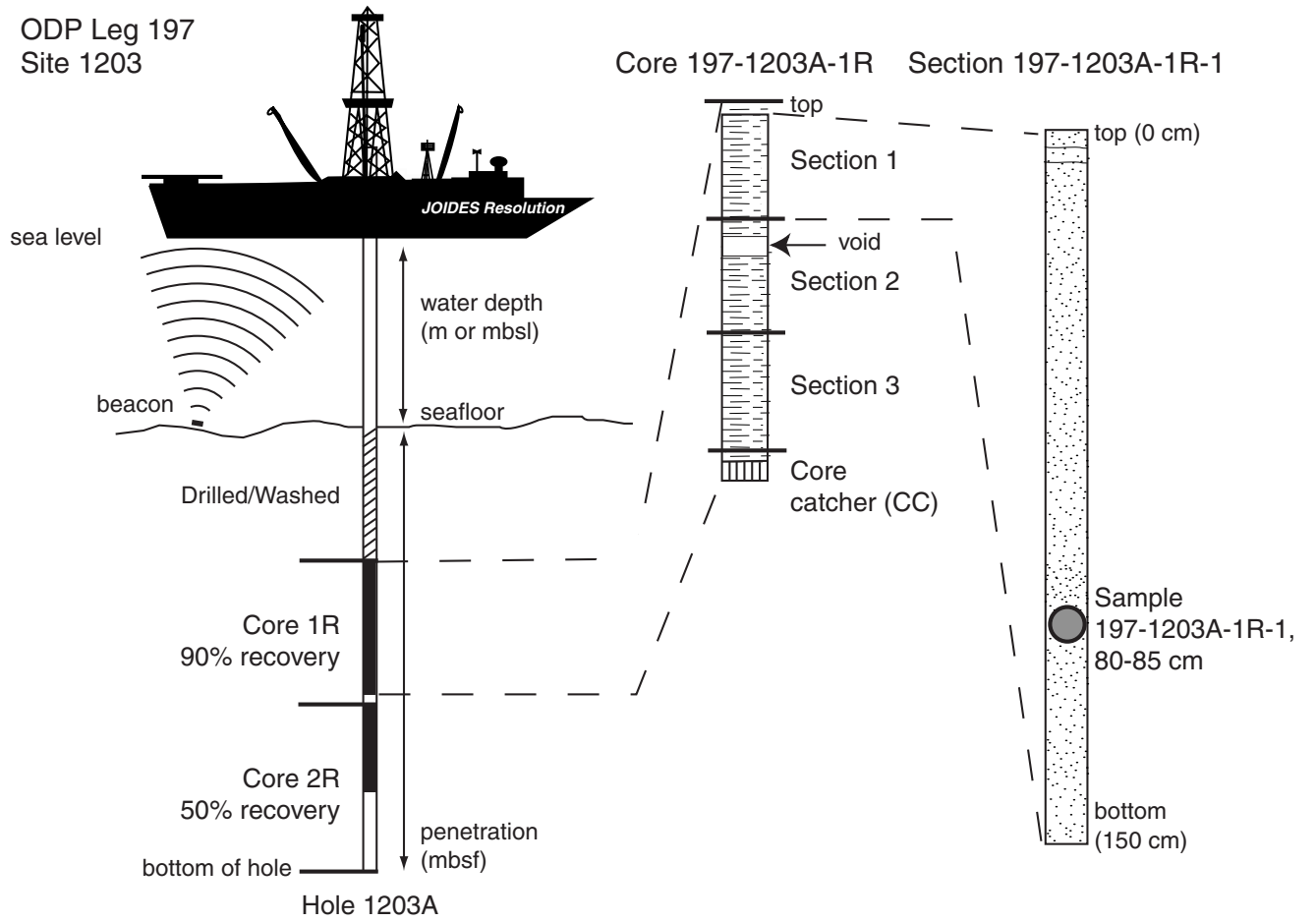


Figure F2. Example of core description form ("barrel sheet") for sediment samples and sedimentary rocks.

Site 1203 Hole A Core 1R Cored 300.0 to 304.65 mbsf								
METERS	GRAPHIC LITH.	BIOTURB.	STRUCTURE	ACCESSORIES	DISTURB.	SAMPLE	COLOR	DESCRIPTION
2						SS	lt GY	<p>NANNOFOSSIL DIATOM OOZE, DIATOM NANNOFOSSIL OOZE, NANNO-DIATOM MIXED OOZE, and DIATOM OOZE</p> <p>This core consists of very slightly disturbed, highly to moderately bioturbated horizontal beds of white DIATOM NANNOFOSSIL, and NANNOFOSSIL DIATOM OOZE. Boundaries are gradational, but at 2, 47, and 3, 25 cm. A mixed lithology (hereinafter referred as NANNO-DIATOM MIXED OOZE) is characterized by more or less equal proportion of calcareous and siliceous microfossils.</p> <p>Sections 1 and 2 consist of alternating cm- to dm-scale beds of massive white DIATOM NANNOFOSSIL OOZE and faintly laminated gray/pinkish gray NANNO-DIATOM MIXED OOZE.</p> <p>Section 2 also contains light olive brown DIATOM OOZE (at 35-45 cm) with underlying undulated and sharp contact.</p> <p>Section 3 contains white to light gray NANNOFOSSIL DIATOM and grayish brown DIATOM OOZE.</p>
						SS	WH	
						SS	..	
						CAR	pk GY	
						XRD	..	
						SS	pk GY	
						SS	GY	
						SS	..	
						SS	..	
						SS	WH	
						SS	lt GY	
						SS	..	
						SS	..	
						SS	..	
						SS	..	
						PAL	..	

Figure F3. Symbols used for description of the sediment lithology/lithologic component used in the “Graphic Lithology” column on the barrel sheet.

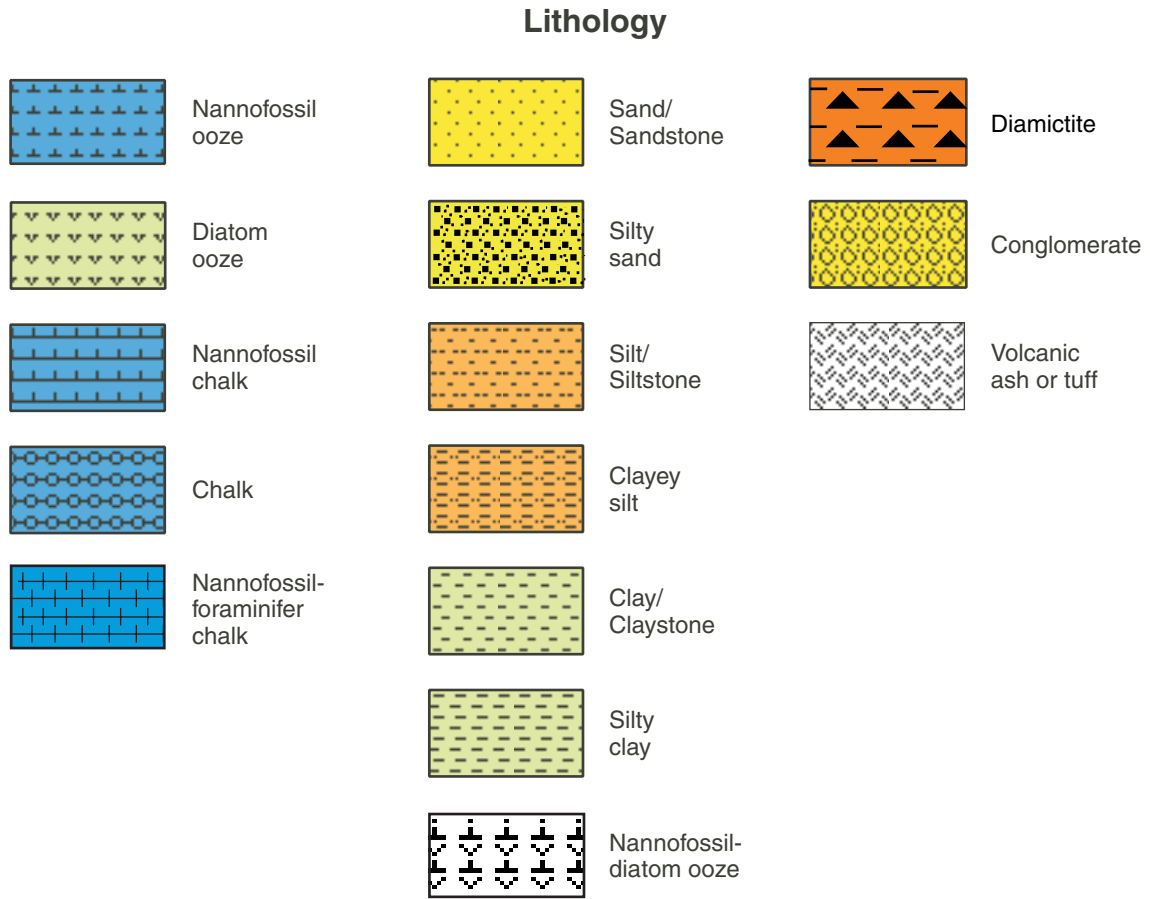


Figure F5. Diagram showing classes of granular sediment (after Mazzullo et al., 1988).

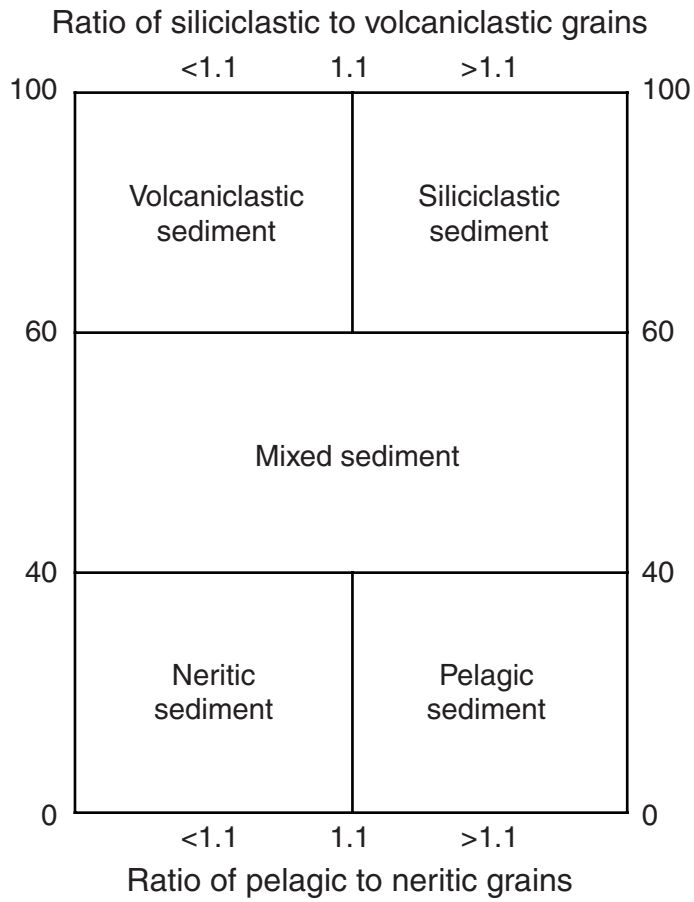


Figure F6. Udden-Wentworth grain-size scale for siliciclastic sediment (Wentworth, 1922).

Millimeters	μm	Phi (ϕ)	Wentworth size class	
4096		-20	Boulder (-8 to -12 ϕ)	Gravel
1024		-12		
256		-10		
64		-8	Pebble (-6 to -8 ϕ)	
16		-6		
4		-4	Pebble (-2 to -6 ϕ)	
3.36		-2		
2.83		-1.75	Gravel	
2.38		-1.50		
2.00		-1.25		
1.68		-1.00		
1.41		-0.75	Very coarse sand	
1.19		-0.50		
1.00		-0.25		
0.84		-0.00	Coarse sand	
0.71		0.25		
0.59		0.50		
1/2		0.75		
0.42	500	1.00		
0.35	420	1.25	Medium sand	Sand
0.30	350	1.50		
1/4	300	1.75		
0.210	250	2.00	Fine sand	
0.177	210	2.25		
0.149	177	2.50		
1/8	149	2.75		
0.105	125	3.00	Very fine sand	
0.088	105	3.25		
0.074	88	3.50		
1/16	74	3.75		
0.0530	63	4.00	Coarse silt	
0.0440	53	4.25		
0.0370	44	4.50		
1/32	37	4.75		
0.0156	31	5	Medium silt	Mud
1/64	15.6	6	Fine silt	
1/128	7.8	7	Very fine silt	
1/256	3.9	8	Clay	
0.0020	2.0	9		
0.00098	0.98	10		
0.00049	0.49	11		
0.00024	0.24	12		
0.00012	0.12	13		
0.00006	0.06	14		

Figure F7. Shepard's ternary diagram including textural fields for naming siliciclastic sediment (after Shepard, 1954).

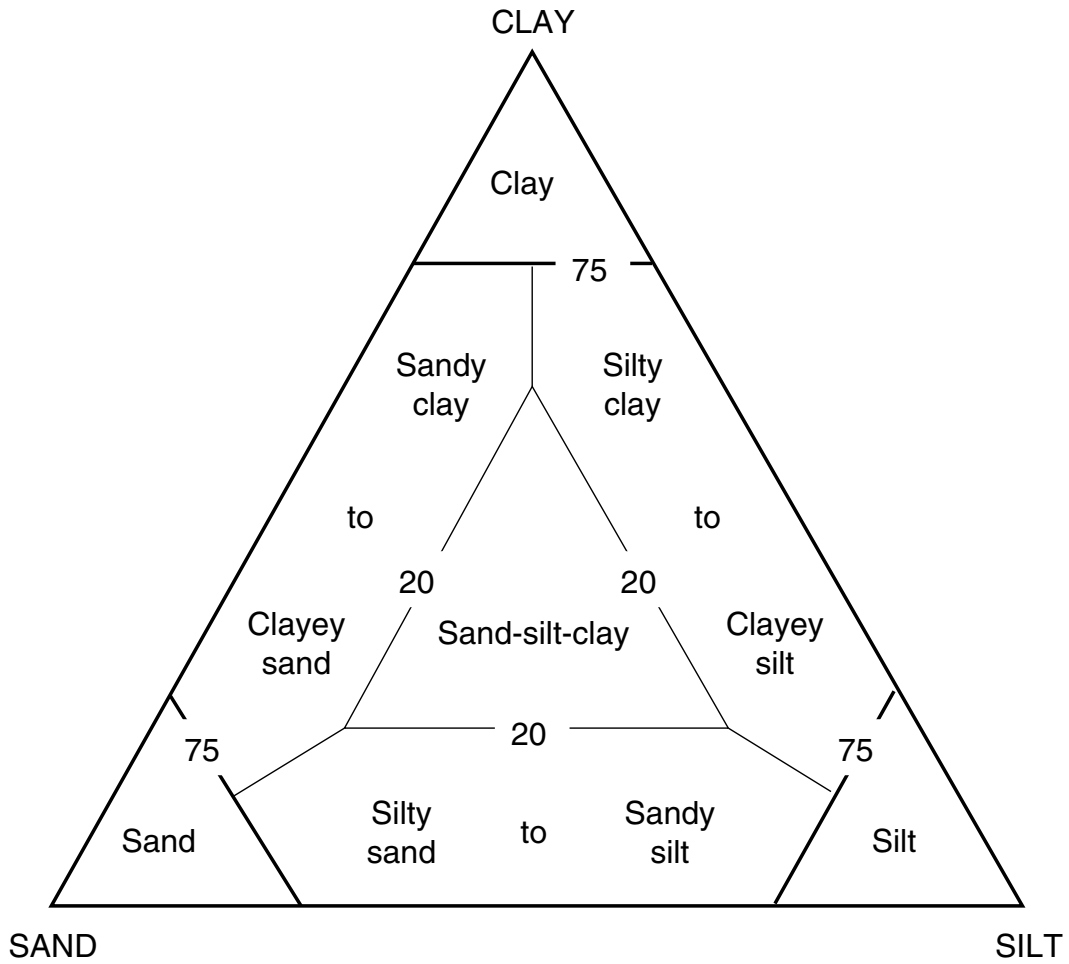


Figure F8. Grain-shape comparator used for coarse-grained sediment components (Mazzullo et al., 1988).

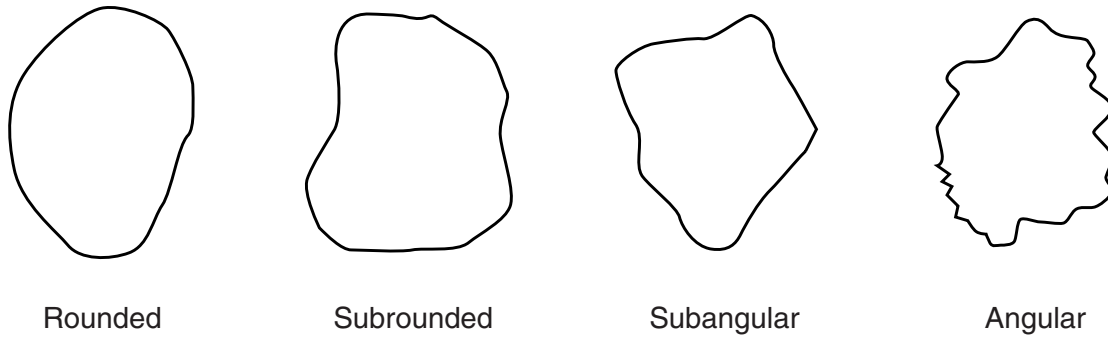


Figure F9. Comparison chart for visual percentage estimation (after Terry and Chilingar, 1955).

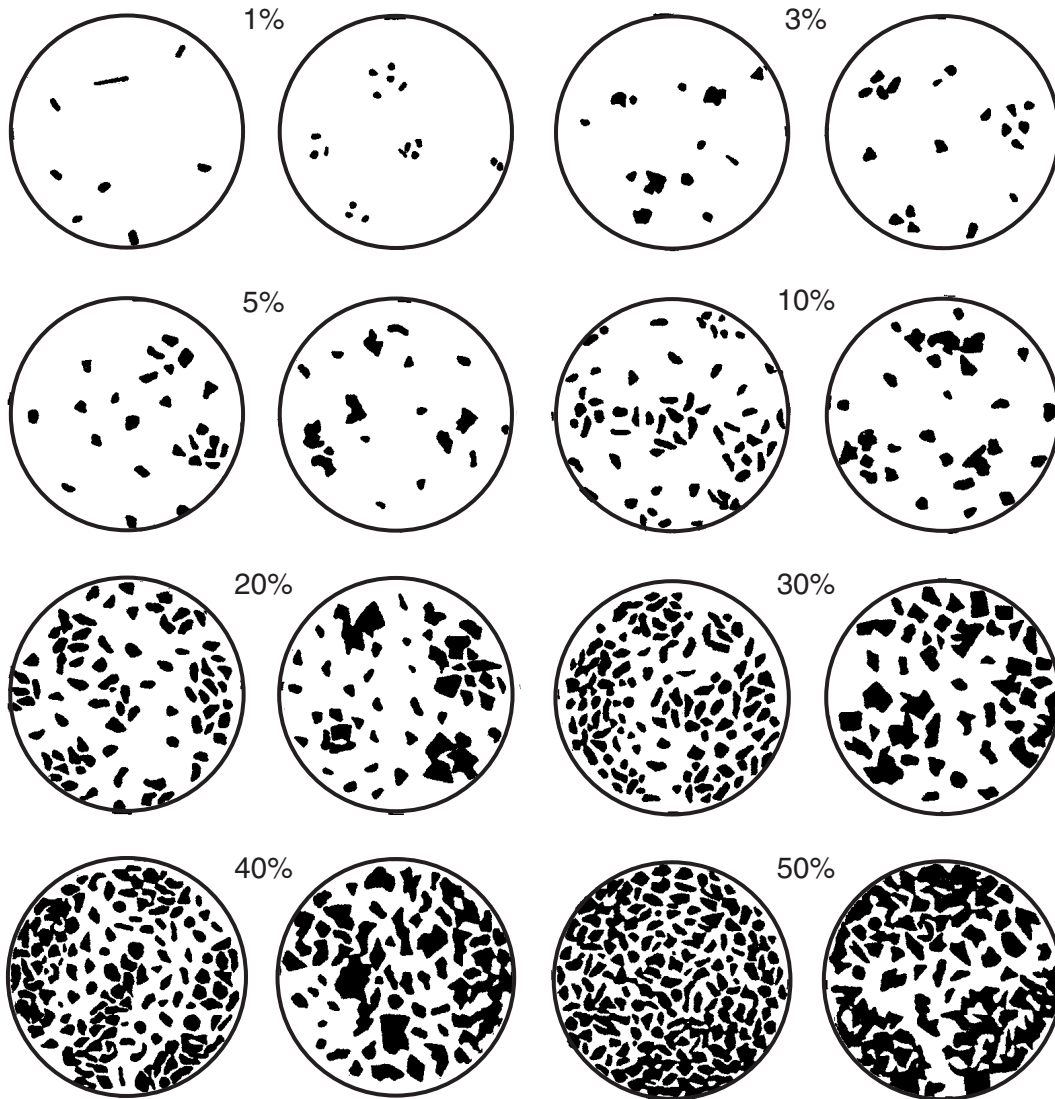


Figure F10. Late Cretaceous–Holocene geochronologic units correlated with calcareous nannofossil zonations and with the magnetic polarity timescale. Figure modified from Shipboard Scientific Party (1997b); see text for data sources. Nannofossil datums indicated are as follows: B (base) = first appearance, T (top) = last appearance. Black bands = normal polarity, white bands = reversed polarity. (Continued on next three pages.)

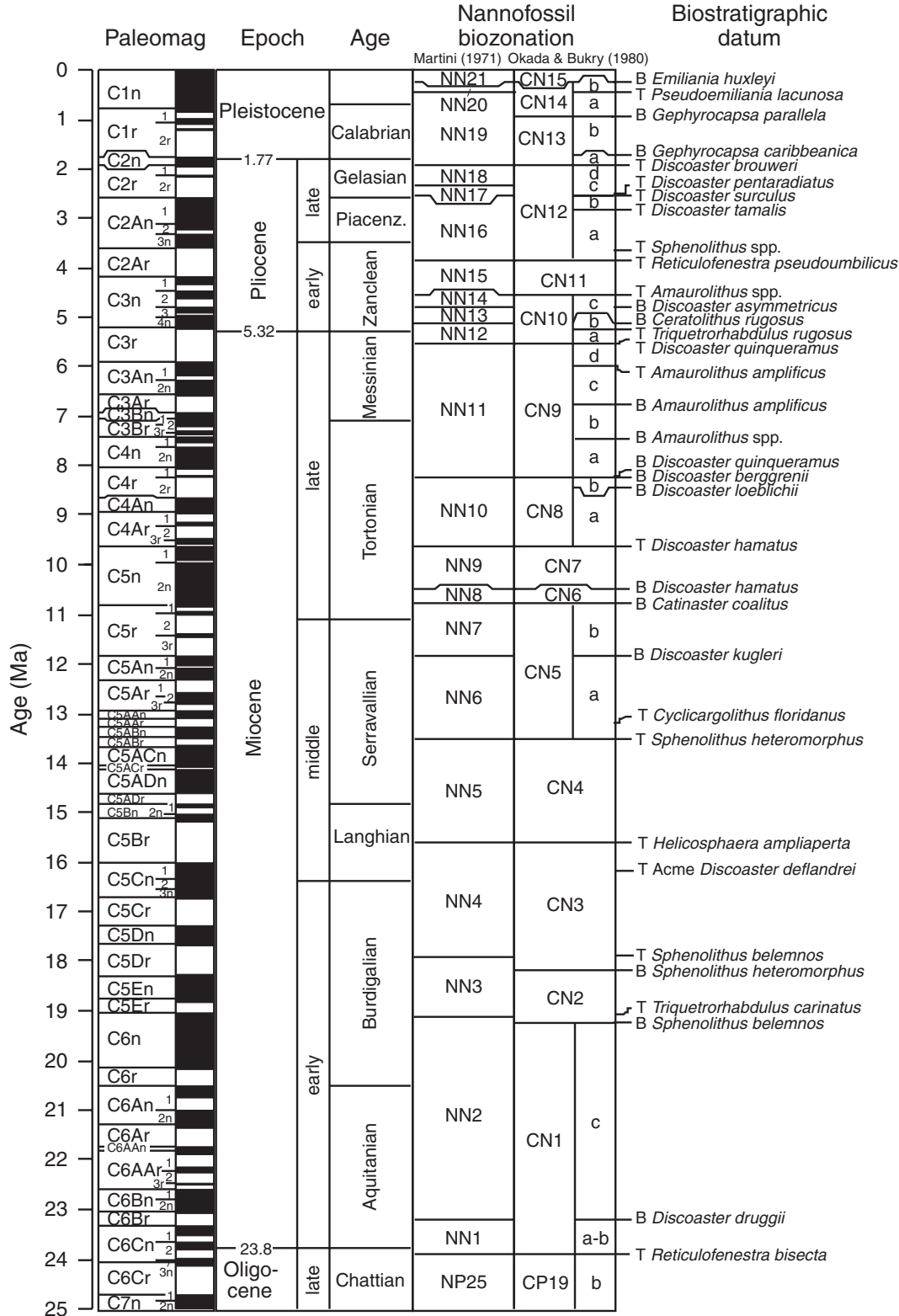


Figure F10 (continued).

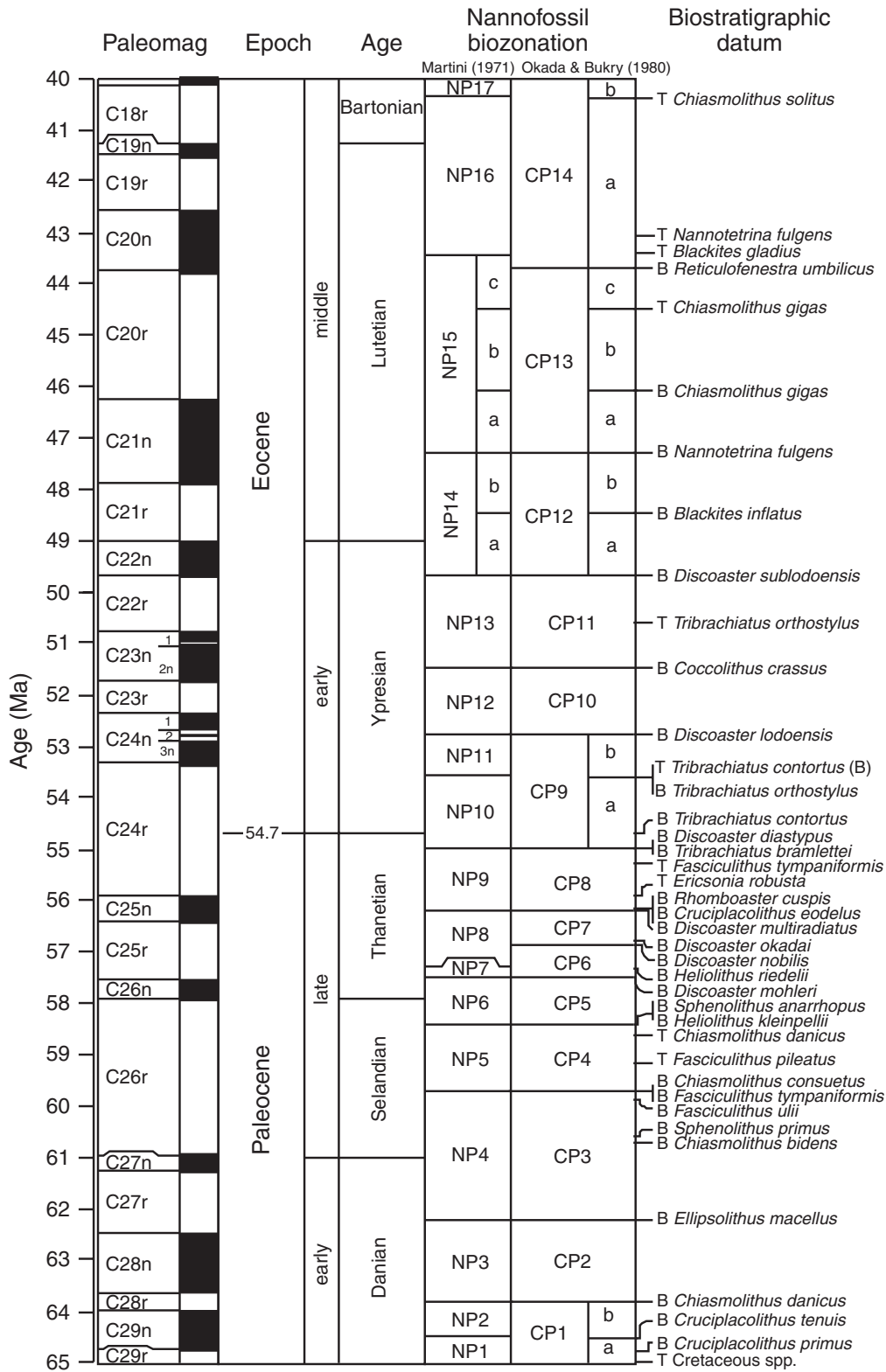


Figure F10 (continued).

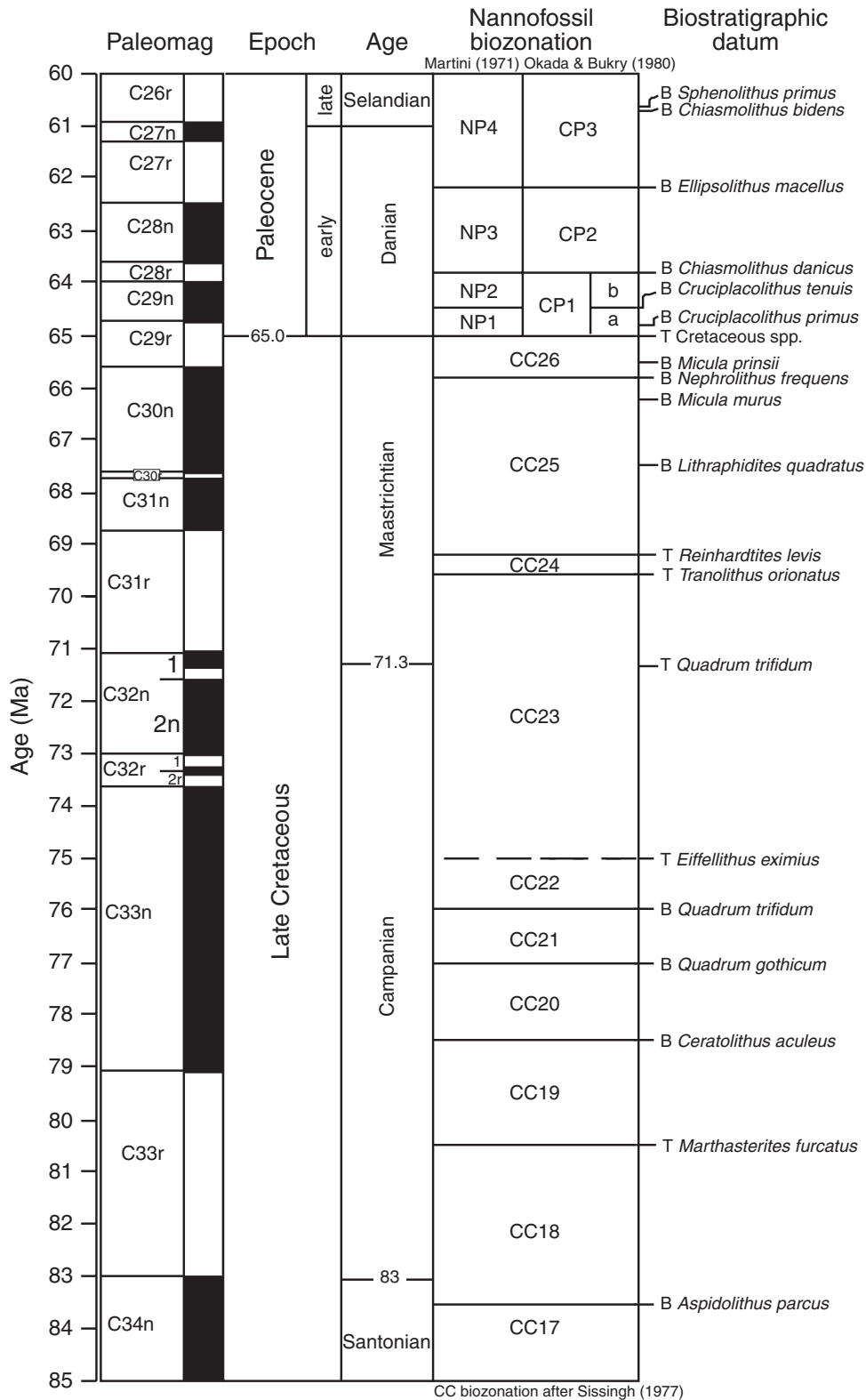


Figure F11. Nongeneric classification of volcanic deposits.

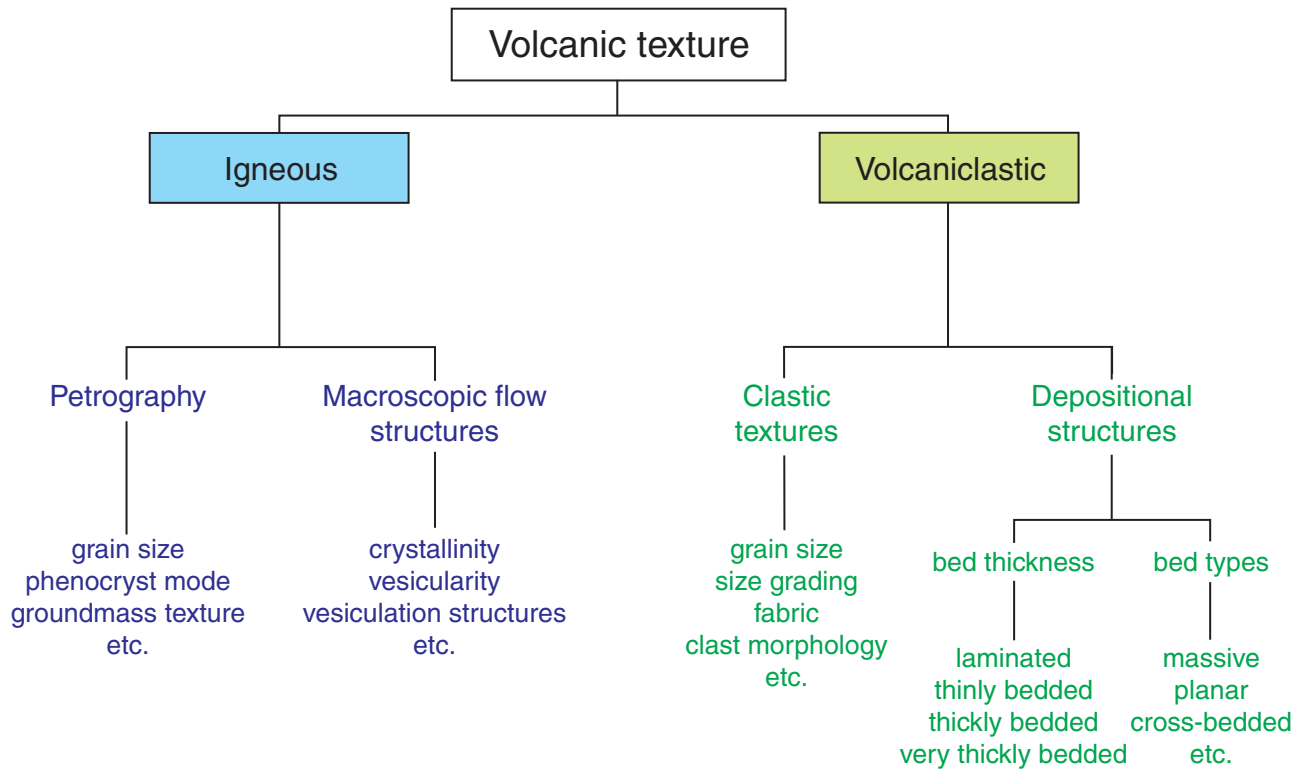


Figure F12. Generic classification of volcanic deposits. Words in *italics* refer to processes.

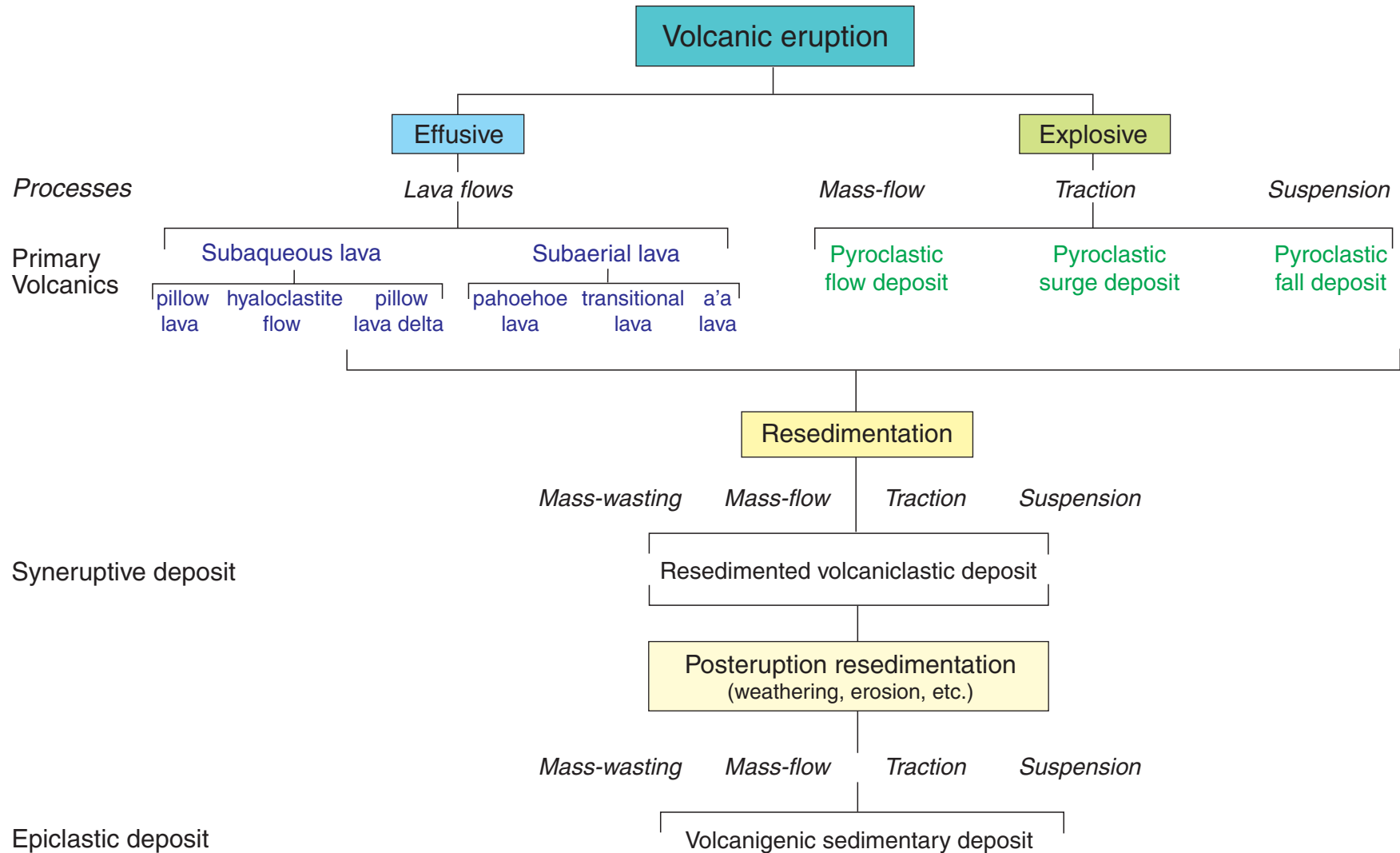


Figure F14. Composite graphic log illustrating characteristic structures of pahoehoe sheet lobes. The left side of the column shows the characteristic three-part division of (A) sheet lobes (CRZ = crustal zone, PLZ = platy zone, CLZ = columnar zone) and (B) jointing styles. The right side of the column shows distribution of (C) vesiculation structures (VZ = vesicular zone, MV = megavesicle, HVS = horizontal vesicle sheet, VC = vesicle cylinder, SV = segregation vesicle, PV = pipe vesicle, BVZ = basal vesicular zone), (D) vesiculation (non- to sparsely vesicular [d = 0–5 vol%], moderately vesicular [m = 10–20 vol%], and vesicular [v = 30–40 vol%]), and (E) degree of crystallinity (G = hyaline, hyh = hypohyaline, hc = hypocrySTALLINE, c = holocrySTALLINE). The scale h/l indicates normalized height above the base of the sheet lobe (h = height in lobe and l = total lobe thickness) (from Thordarson and Self, 1998).

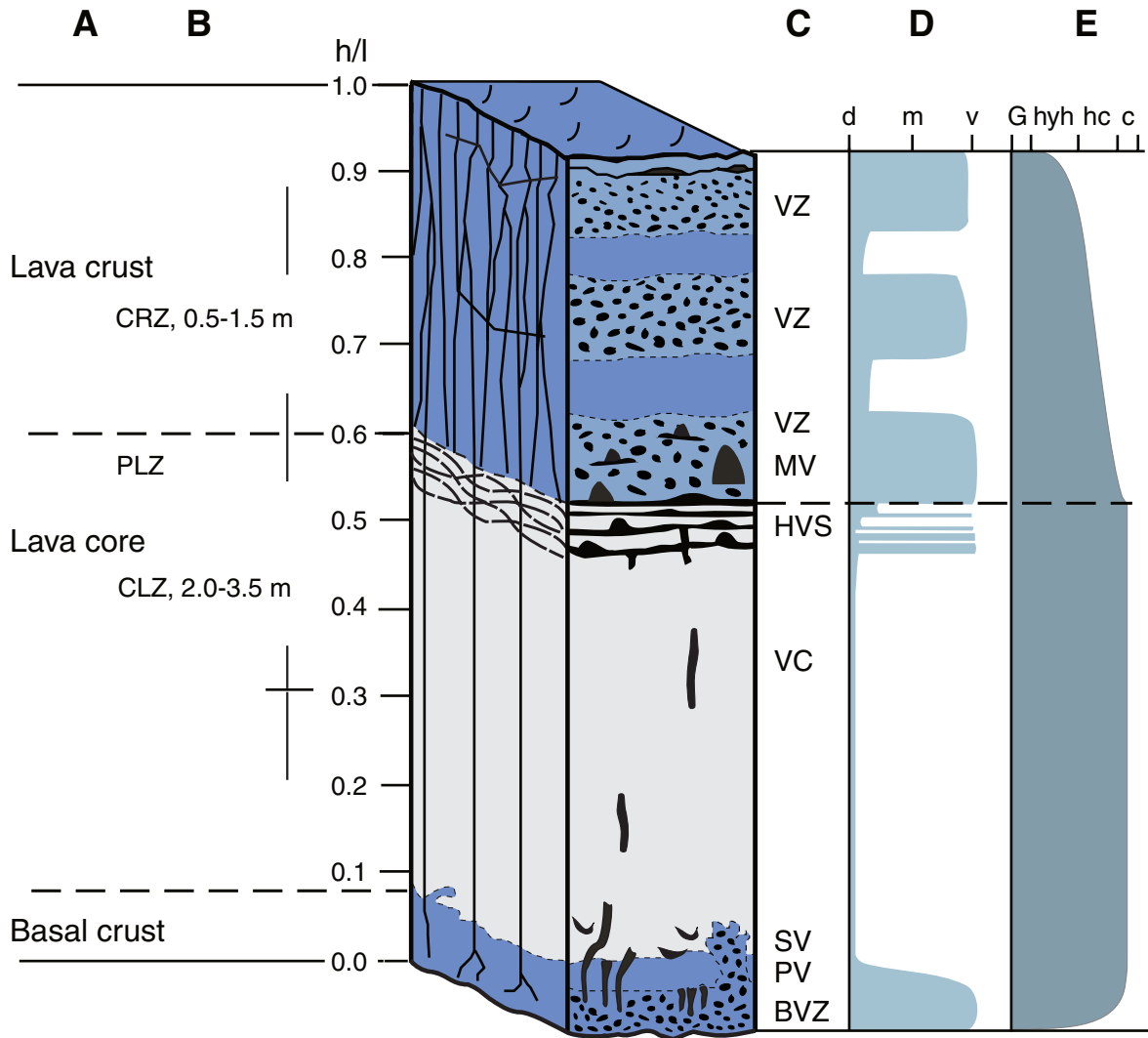


Figure F15. Characteristic structures of a'a flow. **A.** Photograph of an active a'a flow channel, where viscous tearing of the cooling lava is forming scoriaceous rubble on the flow surface. Levees are formed at the channel margins by sideward displacement of the flow top rubble. **B.** Sketch showing the main structural components of an a'a lava flow in a vertical section. Pattern of flow lines in moving lava is also shown. The hammer (lower center) is shown for scale. Modified from Lockwood and Lipman (1980).

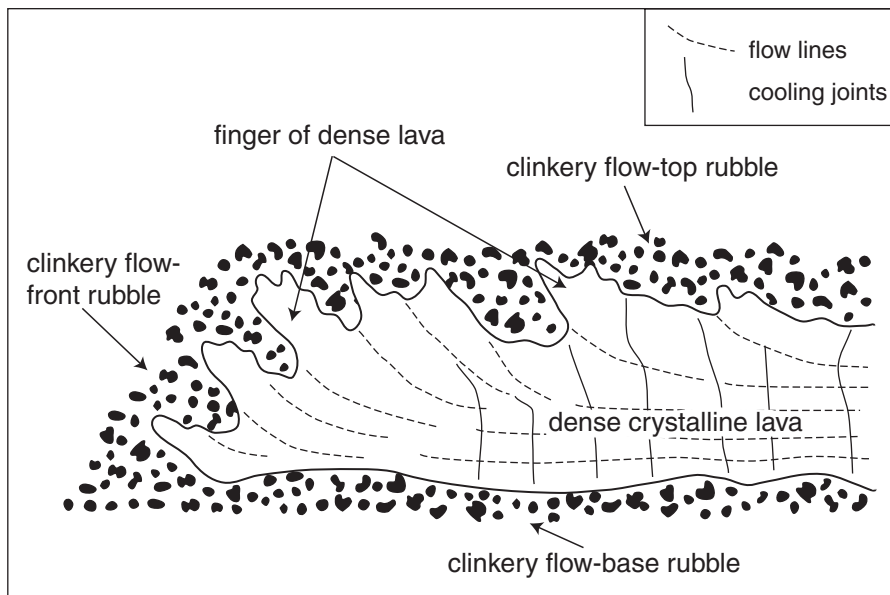
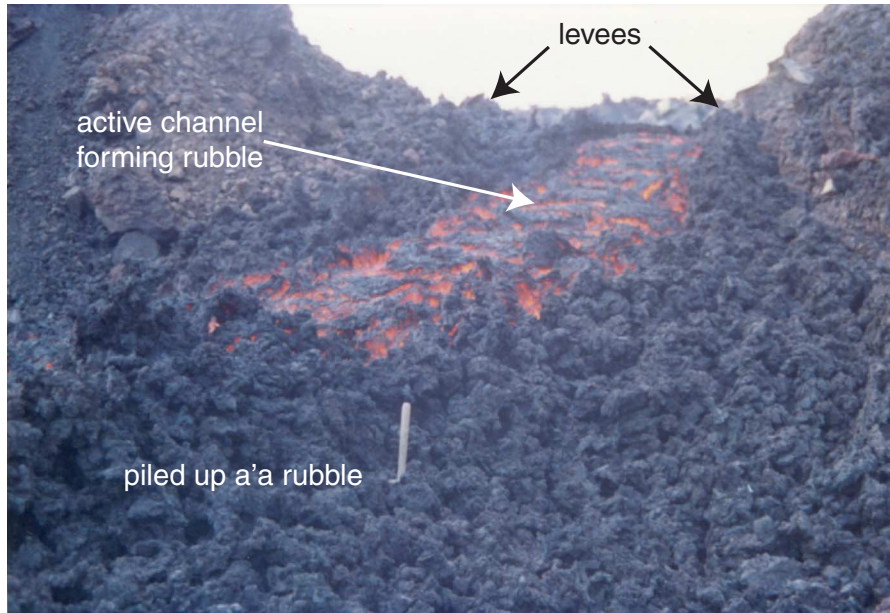


Figure F16. Characteristic structures of rubbly pahoehoe flow. A. Photograph of a rubbly pahoehoe lava with smooth flow base and rubbly flow top consisting of slabs of pahoehoe crust and a'a-like clinker (partly covered by moss [light gray]). The person is shown for scale. B. Sketch showing the main structural components of a rubbly pahoehoe lava flow in a vertical section.

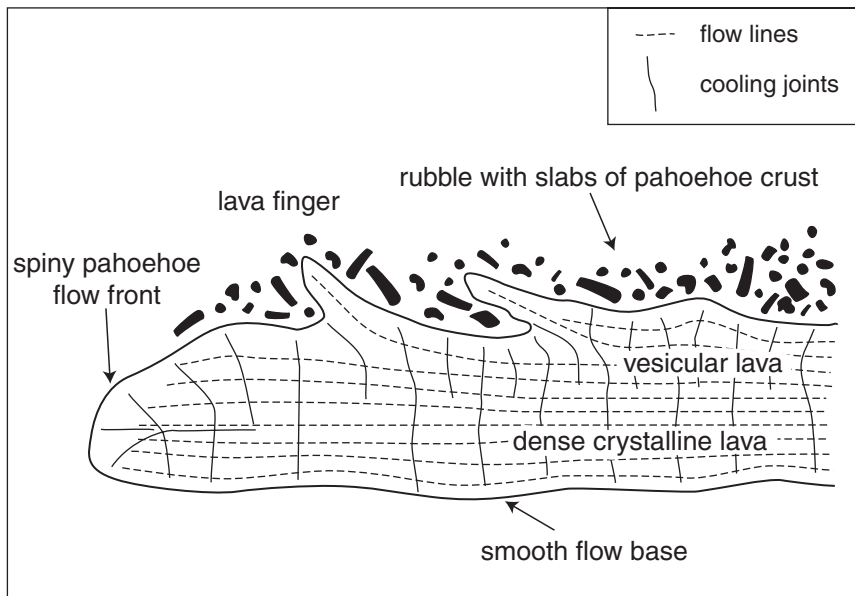
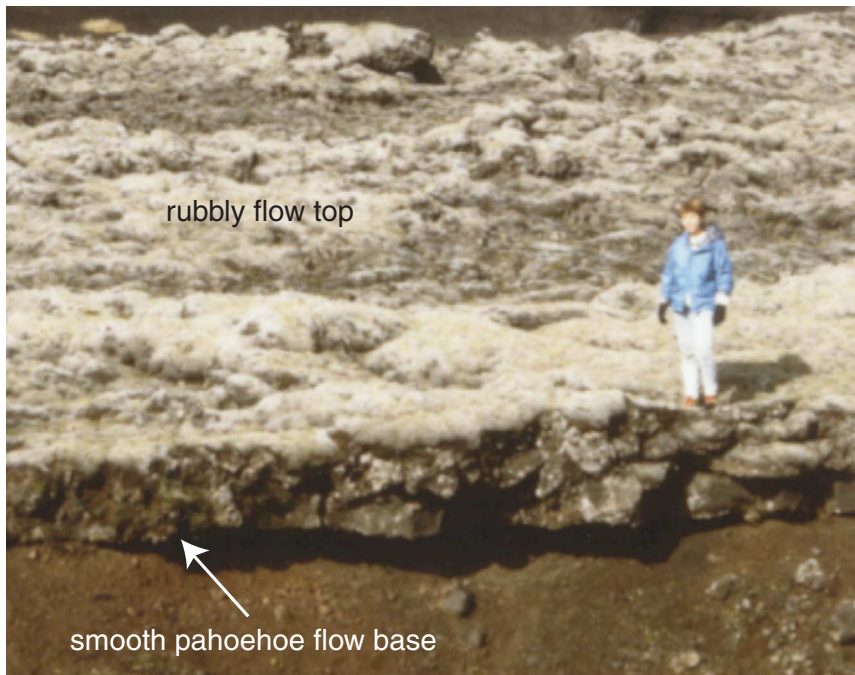


Figure F18. Igneous texture/structure definitions and abbreviations.

Phenocryst		a Aphyric (<1%)	s p Sparsely phyric (1%-2%)	m p Moderately phyric (2%-10%)	h p Highly phyric (>10%)	
Groundmass/ Grain size		G Glass	a p Aphanitic (<1 mm)	f g Fine grained (1-2 mm)	m g Medium grained (2-5 mm)	
Vesicle Structure		p v Pipe vesicles (hollow)	v c Vesicle cylinder (filled)	h v s Horizontal vesicle (= segregation veins)	m v Mega- vesicles	v z Vesicular zone (>10 vol%)
Vesicularity		n v Nonvesicular (<1%)	s p v Sparsely vesicular (1%-5%)	m o v Moderately vesicular (5%-20%)	h i v Highly vesicular (>20%)	
Veins		V Veins present				

Figure F19. Example of the alteration log. Brn C = brown clay, Sap. = saponite, Py = pyrite, Cel = celadonite, Zeol = zeolite, GC = green clay, DkGC = dark green clay.

Leg 197 Alteration Log-1204A																			
Unit	Core	Section	Top (mbsf)	Alteration degree	FeOx	CaCO3	Brn C	Sap.	Py	Cel	Zeol	Vesicularity	CaCO3	Brn C	GC	Py	DkGC	Zeol	FeOx
2	7R	2	820.95	3			x					3	x						
2	7R	3	822.32	2.5	x	x	x	x			x	3	x		x				x
2	7R	4	823.82	2.5			x					3	x						
2	8R	1	829.00	3	x		x					3	x		x				x
2	8R	2	830.50	2.5	x		x					3	x						x
2	9R	1	838.60	3	x	x	x	x			x	2	x					x	x
2	9R	2	840.10	2	x		x					1	x						x
2	9R	3	841.60	2.5	x		x					2	x						x
2	9R	4	842.97	3	x		x					1.5	x						x
2	10R	1	848.30	2	x		x					2	x						x
2	10R	2	849.77	2	x		x	x			x	2	x	x	x			x	x
2	10R	3	850.91	2			x	x	x		x	2	x	x	x	x		x	
2	10R	4	858.36	2			x	x	x			2	x	x	x	x			
2	10R	5	853.82	2			x	x	x			2	x	x	x	x			
2	10R	6	855.06	3	x		x	x	x			2	x	x	x	x			x

Figure F20. Example of the vein log. LBrn = light brown. sv = subvertical, i = inclined, sh = subhorizontal. GC = green clay. Py = pyrite.

Leg 197 Vein Log-1204A																
Identifiers				Position			Vein					Halo				Comments
Unit	Core	Sec	piece	mbsf top section	mbsf m	cm top	cm bot	(mm) Width	App. Orient.	Mineralogy	Proportions %	Color	Width mm	Mineralogy	Proportions %	
2	7R	2	2	820.95	821.15	20	27	1	sv	CaCO3	100	LBrn	1	FeOx	100	Border of piece/CaCO3 well shaped crystals
2	7R	2	3	820.95	821.25	30	34	2	i	CaCO3	100	LBrn	1	FeOx	100	Border of piece/CaCO3 well shaped crystals
2	7R	2	8	820.95	821.88	93	97	5	sv	CaCO3	100					Border of piece/CaCO3 well shaped crystals
2	7R	2	9	820.95	821.96	101	103	3	i	CaCO3	100					Border of piece/CaCO3 well shaped crystals
2	7R	2	11	820.95	822.20	125	128	2	i	CaCO3	100					Border of piece/CaCO3 well shaped crystals
2	7R	3	1	822.32	822.33	1	7	3	i	CaCO3	100	LBrn	1	FeOx	100	Border of piece/CaCO3 well shaped crystals
2	7R	3	2	822.32	822.53	21	24	2	i	CaCO3	100					Border of piece/CaCO3 well shaped crystals
2	7R	3	5	822.32	822.85	53	69	2-3	sv	CaCO3-FeOx	60-40					
2	7R	4	1	823.82	823.83	1	9	3 cm	sv	CaCO3-FeOx	70-30					Brecciated material
2	8R	2	3	830.50	830.74	-	-	5	sv	CaCO3-FeOx	50-50					crystals/Goethite/pervasive FeOx alteration
2	8R	1	19	829.00	830.19	119	121	2		CaCO3-FeOx	50-50					
2	9R	2	11	840.1	841.51	141	142	5	sh	CaCO3	100					
2	9R	3	15	841.6	842.90	130	131	1		CaCO3-FeOx	50-50					Border of piece, LBrn color in the vein
2	10R	3	1	850.91	851.32	41	47	2	i	CaCO3-Py	95-5					Vesicles filled with GC-Py
2	10R	3	2	850.91	851.81	90	106	1	i	CaCO3-Py	80-20					
2	10R	4	1	852.36	852.61	25	30	2	i	CaCO3-GC	80-20					
2	10R	4	3a	852.36	853.02	66	78	5	i	CaCO3-FeOx-GC	50-30-20					
2	10R	4	3b	852.36	853.48	112	114	2-5	sh	CaCO3-FeOx-GC	50-30-20					
2	10R	5	1abc	853.82	853.93	11	40		sv	CaCO3-GC	60-40	LBrn	5	FeOx		Close up photo

Figure F21. ODP magnetic direction convention, following the convention of the Shipboard Scientific Parties for Legs 133 and 166. The arrow on the split face of the working half of the core is parallel to the negative z-axis of the drill core. By the right-hand rule, the positive x-axis is directed into the working half perpendicular to the y-z plane on the split face.

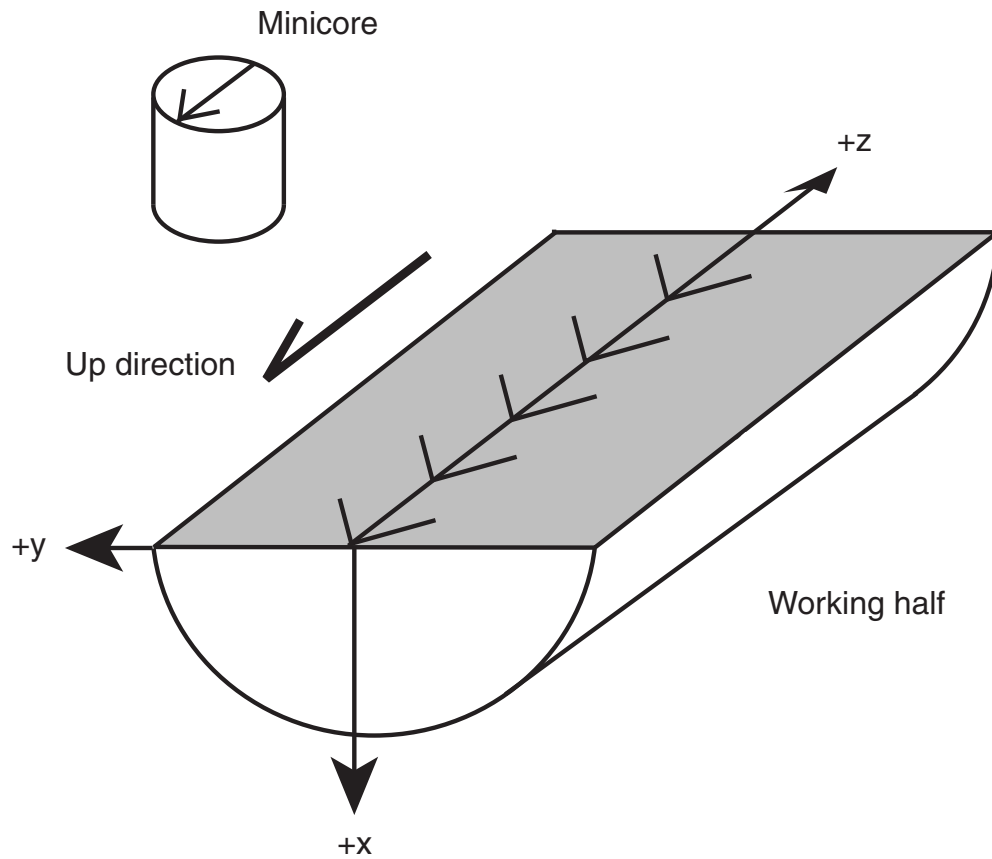


Figure F22. Expected virtual geomagnetic pole (VGP) scatter with latitude based on a global data synthesis collected by McFadden et al. (1991) for two time periods, 45–80 and 80–110 Ma.

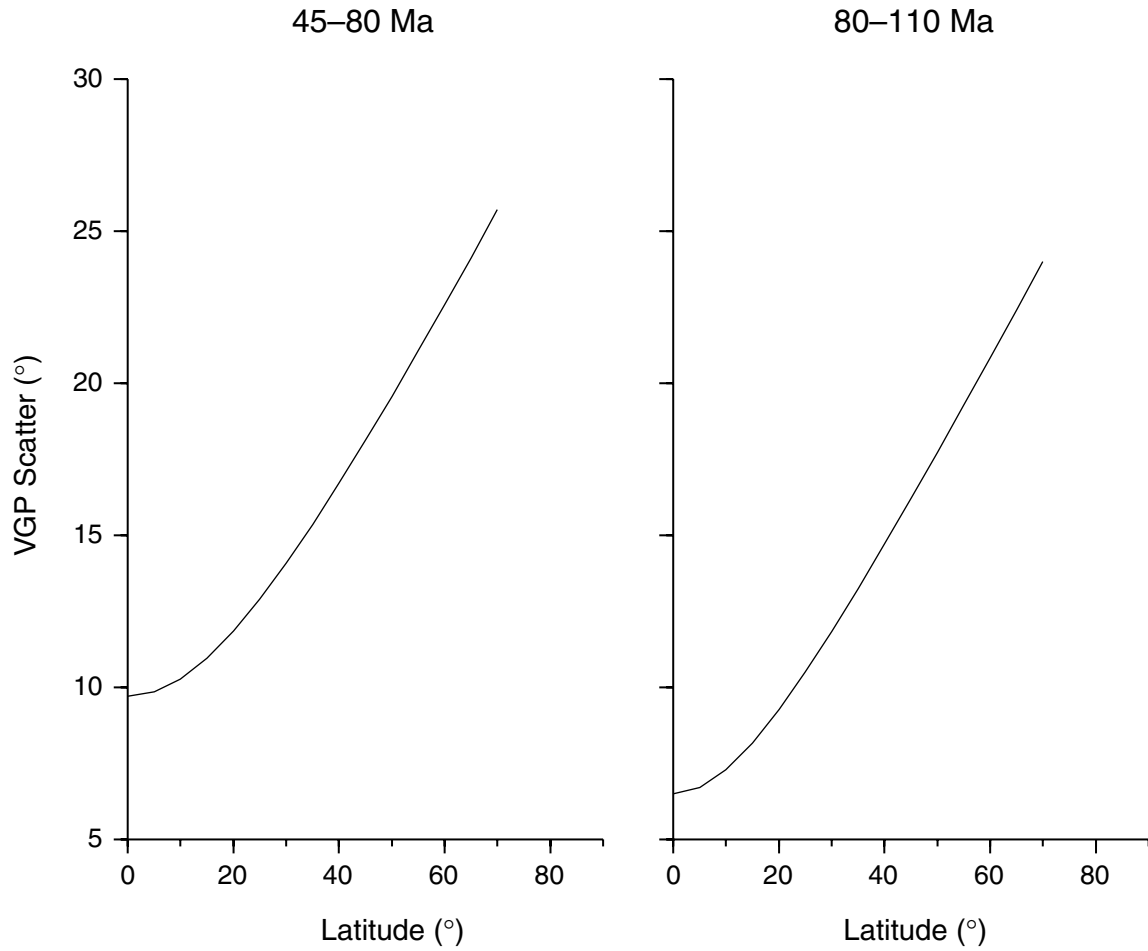


Figure F23. Geomagnetic timescale (from Cande and Kent, 1995).

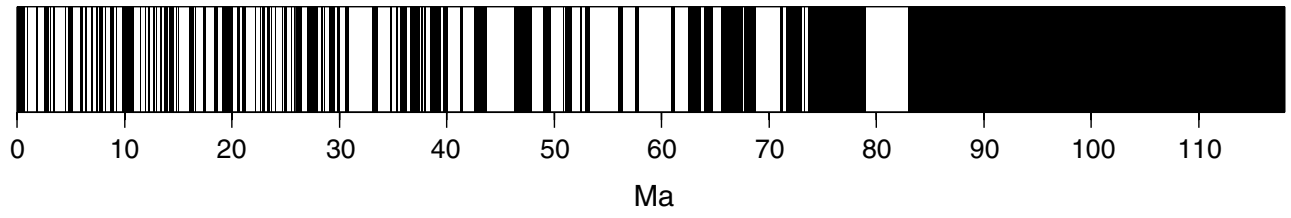


Figure F24. The triple combo and Formation MicroScanner/sonic tool strings used during Leg 197.

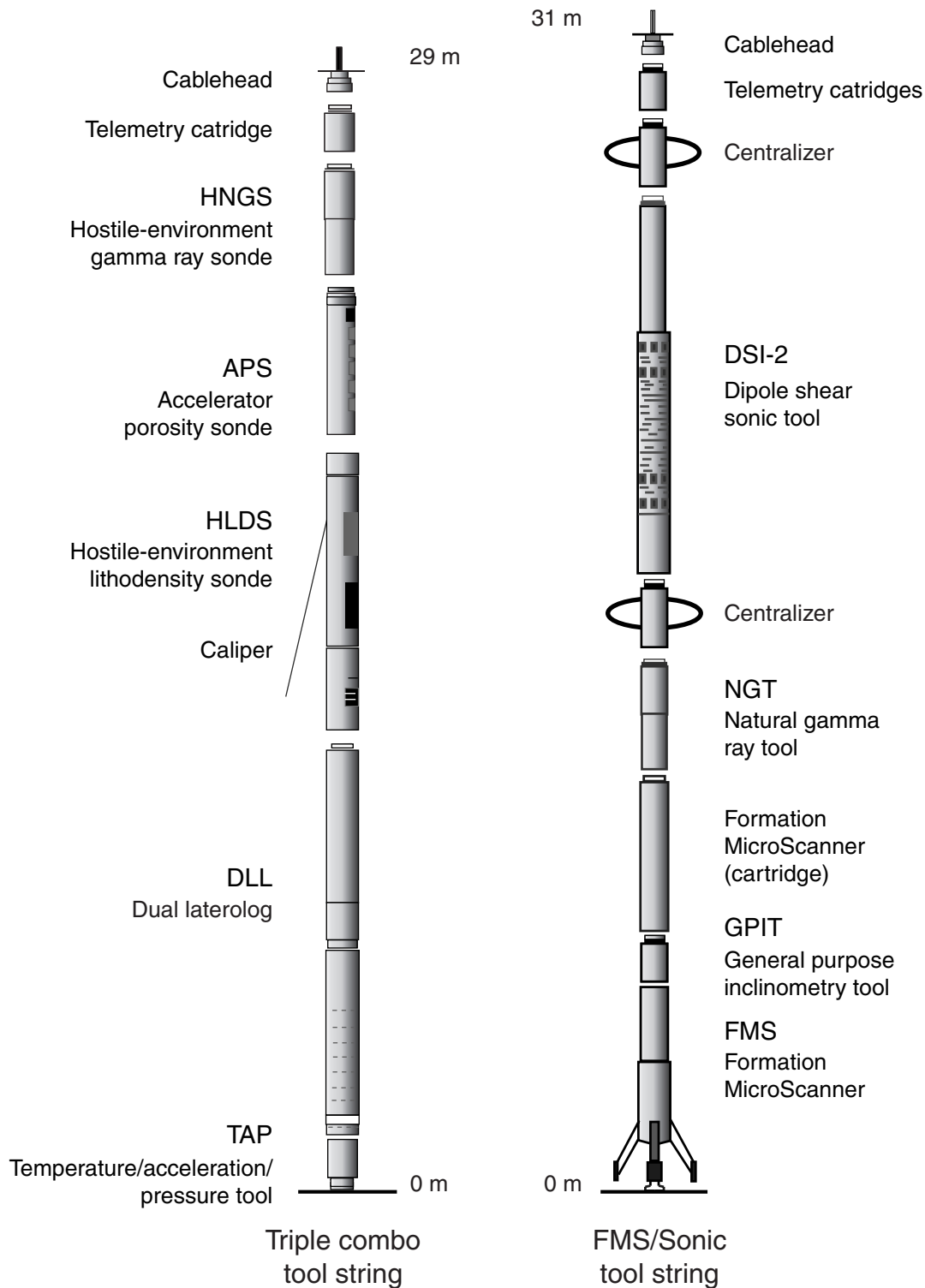


Figure F25. Schematic diagram of the Formation MicroScanner.

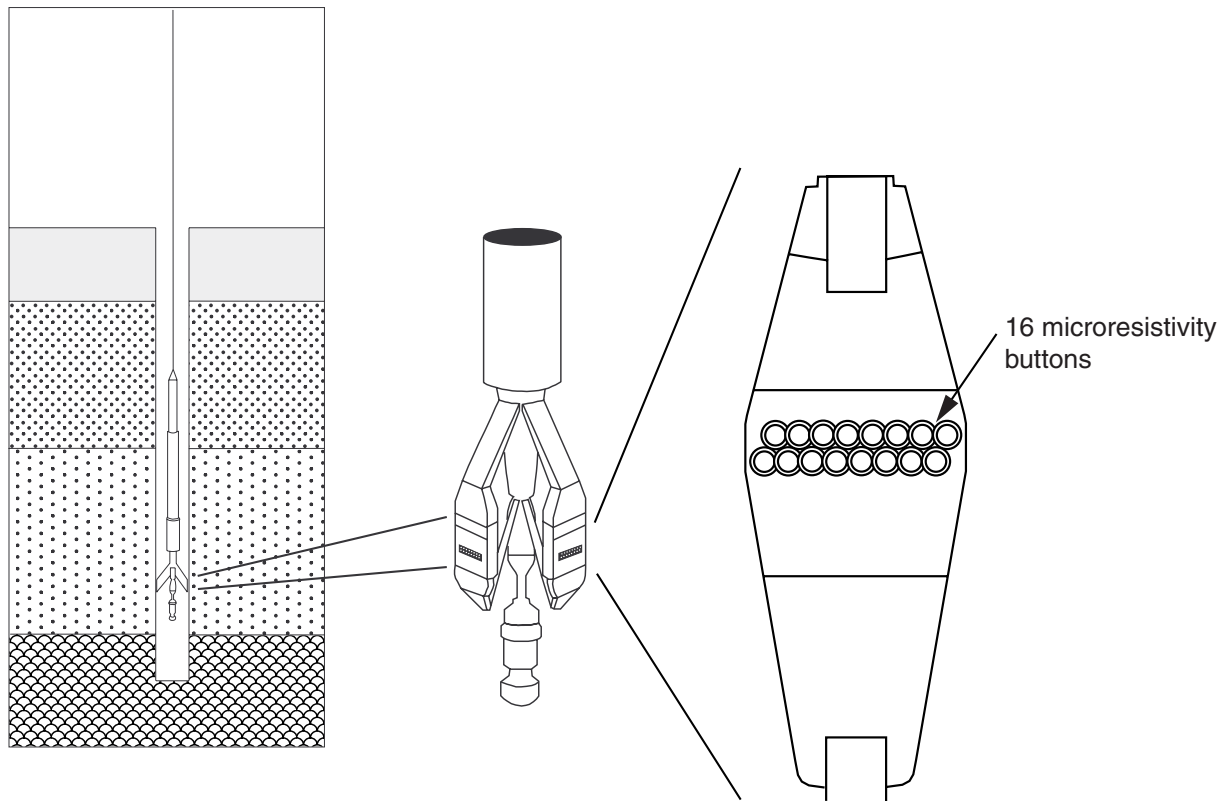


Figure F26. Schematic diagram of the Goettingen Borehole Magnetometer (GBM) and the sensor part of the magnetic susceptibility tool SUSLOG 403-D.

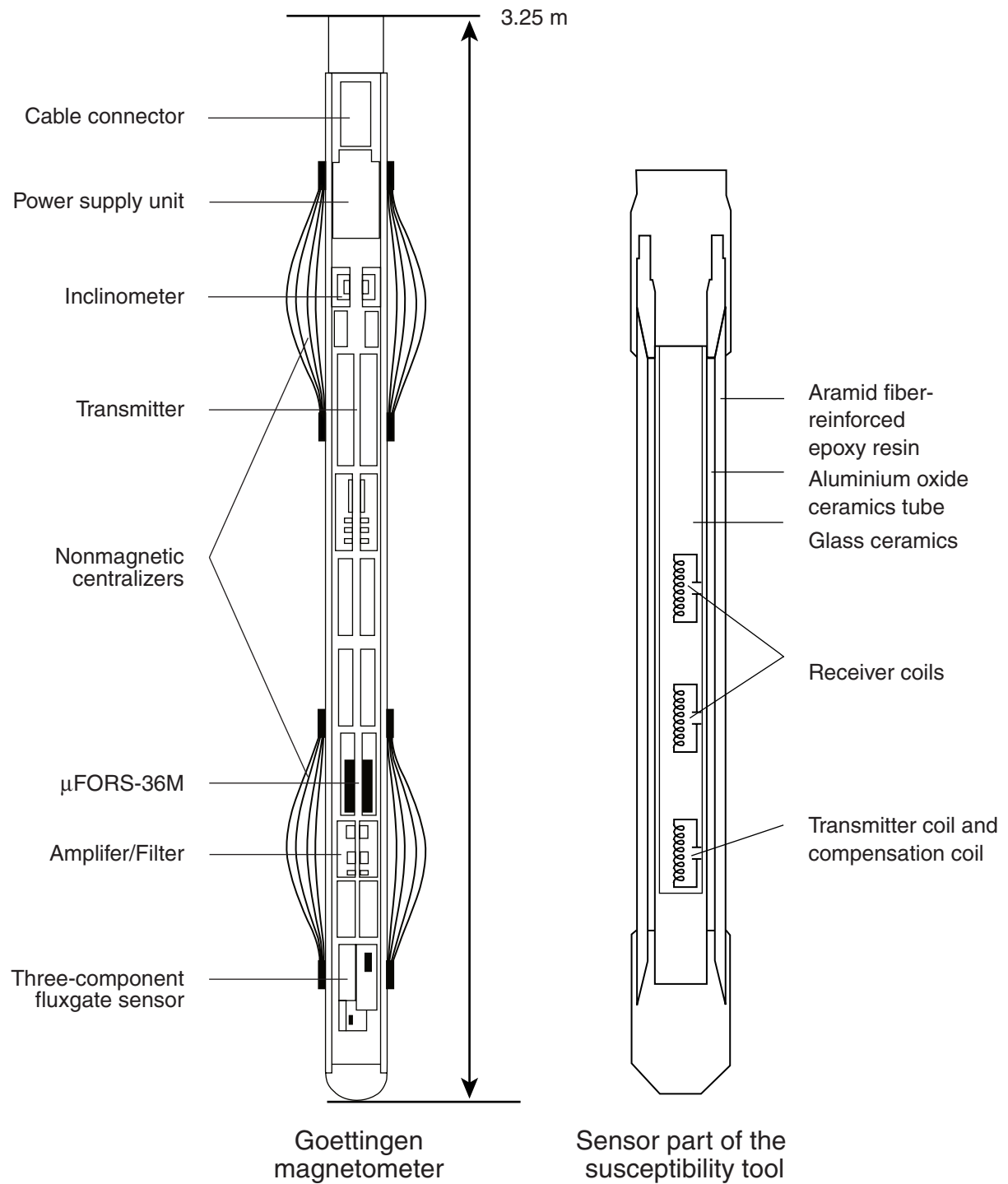
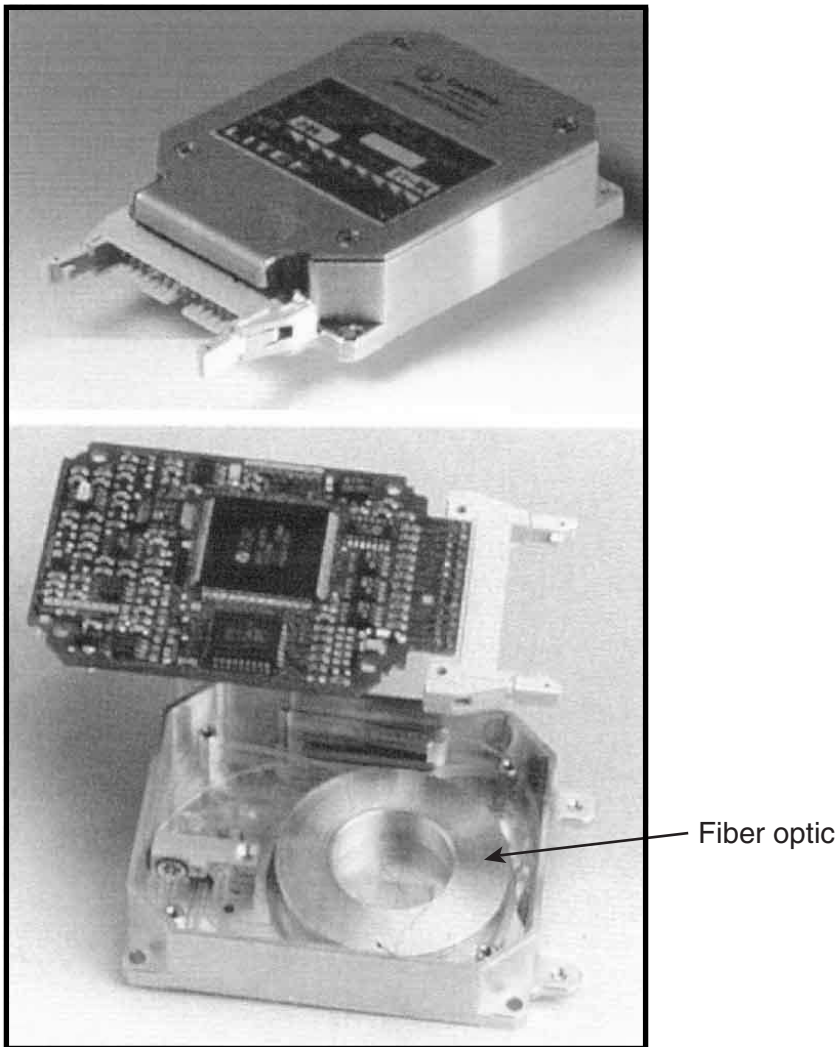


Figure F27. Specifications of the μ FORS-36M fiber-optic rate sensor (LITEF).

μ FORS-36M
Fiber-optic rate sensor (LITEF)



Performance

Range: $\pm 720^\circ/\text{s}$

Temperature range: -40° to 65°C

Size: 19 mm x 53 mm x 58 mm

Weight: 140 g³

Figure F28. Dependence of the rotation rate of the Earth from latitude (ϕ) measured with the fiber-optic rate sensors.

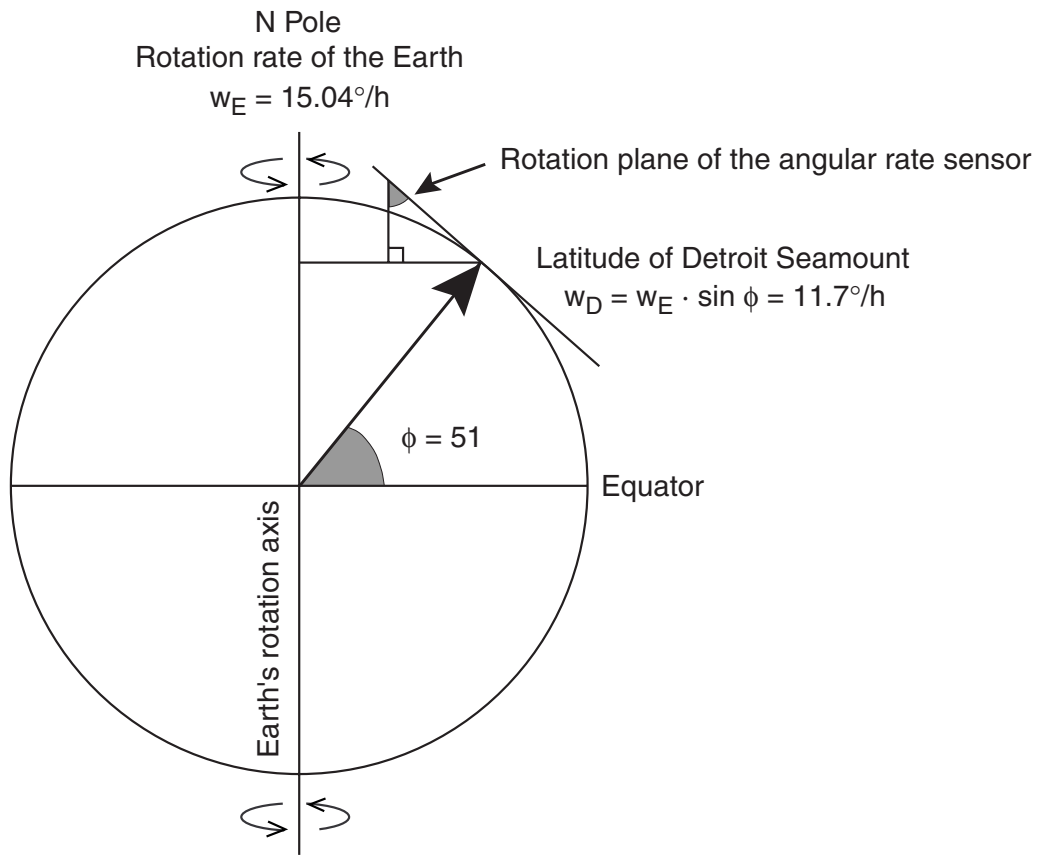


Table T1. Estimated ages of Late Cretaceous to early Miocene calcareous nannofossil datums.

Datum events	Species	Age (Ma)
LAD	<i>Reticulofenestra bisecta</i>	23.9
LAD	<i>Sphenolithus delphix</i>	24.3
LAD	<i>Zygrhablithus bijugatus</i>	24.5
LAD	<i>Sphenolithus ciperoensis</i>	25.5
LAD	<i>Sphenolithus distentus</i>	27.5
FAD	<i>Sphenolithus ciperoensis</i>	29.9
FAD	<i>Sphenolithus distentus</i>	31.5
LAD	<i>Reticulofenestra umbilicus</i>	32.3
LAD	<i>Ericsonia formosa</i>	32.8
LAD	<i>Discoaster saipanensis</i>	34.2
LAD	<i>Discoaster barbadiensis</i>	34.3
FAD	<i>Isthmolithus recurvus</i>	36.0
FAD	<i>Chiasmolithus oamaruensis</i>	37.0
LAD	<i>Chiasmolithus grandis</i>	37.1
FAD	<i>Reticulofenestra bisecta</i>	38.0
LAD	<i>Chiasmolithus solitus</i>	40.4
FAD	<i>Criboecentrum reticulatum</i>	42.0
LAD	<i>Nannotetrina fulgens</i>	43.1
FAD	<i>Reticulofenestra umbilicus</i>	43.7
LAD	<i>Chiasmolithus gigas</i>	44.5
FAD	<i>Chiasmolithus gigas</i>	46.1
FAD	<i>Nannotetrina fulgens</i>	47.3
FAD	<i>Blackites inflatus</i>	48.5
FAD	<i>Discoaster sublodoensis</i>	49.7
LAD	<i>Tribrachiatius orthostylus</i>	50.6
FAD	<i>Coccolithus crassus</i>	51.5
FAD	<i>Discoaster lodoensis</i>	52.8
LAD	<i>Tribrachiatius contortus</i>	53.6
FAD	<i>Tribrachiatius orthostylus</i>	53.6
FAD	<i>Tribrachiatius contortus</i>	54.7
FAD	<i>Discoaster diastypus</i>	55.0
FAD	<i>Tribrachiatius bramlettei</i>	55.0
LAD	<i>Fasciculithus tympaniformis</i>	55.3
LAD	<i>Ericsonia robusta</i>	55.9
FAD	<i>Rhomboaster cuspis</i>	56.2
FAD	<i>Crucioplacolithus edelus</i>	56.2
FAD	<i>Discoaster multiradiatus</i>	56.2
FAD	<i>Discoaster nobilis</i>	56.9
FAD	<i>Helolithus riedelii</i>	57.3
FAD	<i>Discoaster mohleri</i>	57.5
FAD	<i>Helolithus kleinpellii</i>	58.4
LAD	<i>Chiasmolithus danicus</i>	58.6
LAD	<i>Fasciculithus pileatus</i>	59.1
FAD	<i>Chiasmolithus consuetus</i>	59.7
FAD	<i>Fasciculithus tympaniformis</i>	59.7
FAD	<i>Sphenolithus primus</i>	60.6
FAD	<i>Chiasmolithus bidens</i>	60.7
FAD	<i>Ellipsolithus macellus</i>	62.2
FAD	<i>Chiasmolithus danicus</i>	63.8
FAD	<i>Crucioplacolithus tenuis</i>	64.5
FAD	<i>Crucioplacolithus primus</i>	64.8
FAD	<i>Micula prinsii</i>	65.4
FAD	<i>Nephrolithus frequens</i>	65.8
FAD	<i>Micula murus</i>	66.2
FAD	<i>Lithraphidites quadratus</i>	67.5
LAD	<i>Reinhardtites levis</i>	69.2
LAD	<i>Tranolithus orionatus</i>	69.6
LAD	<i>Quadrum trifidum</i>	71.3
LAD	<i>Eiffelithus eximius</i>	75.0
FAD	<i>Quadrum trifidum</i>	76.0
FAD	<i>Quadrum gothicum</i>	77.0
FAD	<i>Ceratolithus aculeus</i>	78.5
LAD	<i>Marthasterites furcatus</i>	80.5
FAD	<i>Aspidolithus parvus</i>	83.5

Notes: LAD = last appearance datum, FAD = first appearance datum.
 Nannofossil datum ages taken from compilation by Shipboard Scientific Party (1997b).

Table T2. Distinguishing characteristics of basalt lava types.

Lava type	Must have	Commonly has	Commonly lacks	Must not have
Pahoehoe subtypes: p-type pahoehoe, spongy pahoehoe	Smooth (continuous) flow top and base; glassy marginal selvage (0.2–1.5 cm thick); vesicular upper crust (15%–60% vesicles); lower vesicular crust (10%–50% vesicles)	0.3- to 80-m flow thicknesses; inflation features (e.g., tumuli); thick massive interior (0%–5% vesicles); compound flow lobes; segregation structures (e.g., vesicle cylinders)	Angular and stretched vesicles	Autobrecciation
Pillow lava	Smooth (continuous) flow top and base; glassy marginal selvage (0.2–1.5 cm thick)	Concentric microvesicular zones; pipe vesicles; compound flow lobes; intercalated with hyaloclastite	Macroscopic vesicular zones	
Slab pahoehoe	Autobrecciated flow top; slabs of broken pahoehoe surfaces	A'a and pahoehoe clasts in breccia; thin basal breccia		Autobrecciation
Spiny pahoehoe	Continuous top and bottom spinose surface	High degree of crystallinity		Basal breccia
Rubbly pahoehoe	Autobrecciated flow top; broken and intact pahoehoe lobes; coherent vesicular crust below breccia; lower vesicular crust	Massive interior; distorted by rounded vesicles; smooth pahoehoe base	Well-defined vesicular zones	
A'a	Autobrecciated flow top; slabs of broken pahoehoe surfaces	2- to 5-m flow thickness; clasts entrained within the core; core pushing into the flow-top breccia; 5%–20% vesicularity of clasts and core; minor eolian sediment infill	Round vesicles; inflation features; segregation structures	Smooth pahoehoe surfaces

Note: Modified from Keszthelyi (2002).

Table T3. General terminology for basaltic lavas and their explanations.

Terminology	Explanation
Lava flow field	A body of lava identified on the basis of field relations and chemistry as the product of one eruption. It may consist of several lava flows.
Lava flow	A regional subunit formed as a continuous event and may correspond to a single eruption episode. A flow may consist of many flow lobes.
Flow lobe	A single unit of lava that is surrounded by a chilled crust and can vary in size from tens of centimeters to several kilometers. This definition applies to both subaerial and subaqueous lavas.
Sheet lobe	A lobe with flat or gently undulating flow surfaces and is produced by one continuous outpouring of lava. It is much wider than it is thick and can be tens to thousands of meters wide.
Breakout	A small lobe originating as an outbreak of lava from the molten interior of a previously formed lobe. Lobe margin and surface breakouts refer to lobes formed as breakouts through the front (or sides) and the upper surface of the feeding lobe, respectively.

Table T4. Lobe structures: terminology, definitions, and abbreviations.

Terminology	Abbreviation	Definition
Contact:		
Distinct	cg	Contact featuring clearly separated glassy pahoehoe surfaces
Annealed, fused	ca	Contact between lobes is marked by a centimeter-thick glassy band formed by fusion of the original lobe surfaces
Discontinuous	cd	Contact between lobes dissipates or disappears when followed in outcrop
Vesiculation structure:		
Vesicles	ve	Molds of gas-filled voids frozen in the lava and are referred to as microscopic (<2 mm diameter) or macroscopic (>2 mm diameter)
Diktytaxitic texture	vd	Microscopic (<2.0 mm), irregular intercrystalline voids and outlined by crystal faces of adjacent groundmass minerals (Fuller, 1931)
Segregation vesicle	sv	Vesicles lined by segregated material
Pipe vesicles and vesicle cylinders	pv vc	Roughly cylindrical pipes of near-vertical orientation that are hollow (pv) or filled with vesicular segregated material (vc)
Horizontal vesicle sheets	hvs	Sheets of vesicular segregated material, centimeters to tens of centimeters thick, that are continuous (>50 m long) and discontinuous (1–10 m long) on an outcrop scale; these sheets were previously identified as segregation veins or vesicle sheets (e.g. Goff, 1996)
Megavesicles	mv	Dome-shaped voids with flat floors and arched to dome-shaped roofs; their dimensions range from several to tens of centimeters; they are floored by moderately vesicular to nonvesicular segregated material and occur in close association with horizontal vesicle sheets
Vesicular zone	hvz	Decimeter- to meters-thick horizons with high concentrations (>10 vol%) of macroscopic vesicles
Petrographic texture:		
Crystallinity	c, hc, hyh, G	Relative abundance of crystals vs. glassy mesostasis is indicated by holocrystalline (c [crystallinity = 90%–100%]), hypocrytalline (hc [50%–90%]), hypohyaline (hyh [10%–50%]), or holohyaline (G [0%–10%])
Granularity		Crystal size of the lava groundmass (See Table T5, p. 81)

Table T5. Igneous texture/structure definitions and abbreviations.

Abbreviation	Texture/structure	Definition
	Phenocryst percent:	
a	Aphyric	<1%
sp	Sparsely phyric	1%–2%
mp	Moderately phyric	2%–10%
hp	Highly phyric	>10%
	Groundmass crystallinity:	
c	Holocrystalline	90%–100% crystals
hc	Hypocrystalline	50%–90% crystals
hyh	Hypohyaline	10%–50% crystals
G	Hyaline	0%–10% crystals
	Grain size:	
pc	Phanerocrystalline	Phaneritic
cg	Coarse grained	>5 mm
mg	Medium grained	2–5 mm
fg	Fine grained	1–2 mm
ap	Aphanitic	<1 mm
mc	Microcrystalline	<0.5 mm (= aphanitic)
cc	Cryptocrystalline	Not visible under binocular microscope (= aphanitic)
	Vesicularity:	
nov	Nonvesicular	<1%
spv	Sparsely vesicular	1%–5%
mov	Moderately vesicular	5%–20%
hiv	Highly vesicular	>20%
	Alteration log:	
v	Veins	
f	Unaltered	<2%
s	Slight	2%–10%
m	Moderate	10%–40%
h	High	60%–80%
vh	Very high	80%–95%
co	Complete	95%–100%
	Mineral form:	
e	Equant	
t	Tabular	
b	Bladelike or lathlike	
	Vesicle type and vesiculation structure:	
ve	Vesicles	
vd	Diktytaxitic texture	
pv	Pipe vesicles	Hollow
sv	Segregation vesicles	
vc	Vesicle cylinder	Filled with vesicular segregation material
hvs	Horizontal vesicle sheets	Segregation veins; filled with vesicular segregation material
mv	Megavesicles	Domed roof and flat floors, may have segregation material at their base
vz	Vesicular zone	>10 vol% macroscopic vesicles

Table T6. ICP-AES run parameters, Leg 197.

Element	Instrument detection limit (ppb)	Wavelength (nm)	Slit width (nm)*	Integration time per calculation point (s)	Voltage (V)	Mode	Increment between points (nm)†	Calculation (points)
Al	2.8	396.152	20/16	0.5	731	2	0.0270	5
Ca	0.2	393.366	20/16	0.5	351	2	0.0180	5
Fe	6.2	259.940	20/16	4.0	732	5	0.0020	1
K	60	766.490	20/16 Alk	0.5	993	2	0.0022	5
Mg	1.6	285.213	20/16	4.0	553	5	0.0022	1
Mn	1.4	257.610	20/16	4.0	643	5	0.0020	1
Na	69	589.592	20/16 Alk	0.5	632	2	0.0021	5
P	272	178.229	20/16	0.5	933	2	0.0018	5
Si	12	251.611	20/16	0.5	612	2	0.0028	5
Si	16	212.412	20/16	0.5	652	2	0.0030	5
Si	27	288.158	20/16	0.5	623	2	0.0029	5
Ti	3.8	334.941	20/16	0.5	651	2	0.0018	5
Ba	1.3	455.403	20/16	4.0	622	5	0.0250	1
Co	6	213.856	20/16	0.5	625	2	0.0021	5
Cr	7	267.716	20/16	4.0	993	5	0.0190	1
Cu	5.4	324.754	20/16	0.5	625	2	0.0019	5
Nb	36	309.418	20/16	0.5	625	2	0.0030	5
Nb	71	322.548	20/16	0.5	625	2	0.0028	5
Ni	15	231.604	20/16	0.5	990	2	0.0021	1
Sc	1.5	361.384	20/16	4.0	753	5	0.0018	1
Sr	0.4	407.771	20/16	0.5	572	2	0.0026	5
V	7.5	292.402	20/16	4.0	993	5	0.0021	1
Y	3.5	371.030	20/16	4.0	693	5	0.0027	1
Zn	1.8	213.856	20/16	0.5	625	2	0.0030	5
Zr	71	343.823	20/16	0.5	673	2	0.0018	5

Notes: * = the widths of the entrance and exit slits. † = the interval in nanometers between each of the calculation points in Mode 2, or the calculation window (in nanometers) that constitutes the single "point" in Mode 5. Alk = the sheath gas flow is increased from 0.15–0.2 to 0.8 L/min for analysis of these elements.

Table T7. Typical values for USGS standards analyzed by ICP-AES, Leg 197.

	BHVO-2				BIR-1				JB-1A			
	A	B	Average	Certified value	A	B	Average	Certified value	A	B	Average	Certified value
Element oxide (wt%):												
SiO ₂	49.15	49.39	49.27	49.85	47.11	47.18	47.14	47.95	52.24	52.08	52.16	52.16
TiO ₂	2.79	2.77	2.78	2.69	0.96	0.96	0.96	0.96	1.3	1.3	1.3	1.3
Al ₂ O ₃	13.37	13.03	13.20	13.85	15.7	15.5	15.6	15.5	14.51	14.51	14.51	14.51
Fe ₂ O ₃	12.35	12.55	12.45	12.23	12.2	11.9	12.1	11.3	8.7	9.5	9.1	9.1
MnO	0.16	0.17	0.16	0.17	0.18	0.18	0.18	0.175	0.14	0.16	0.15	0.15
MgO	7.07	6.97	7.02	7.31	9.7	9.4	9.5	9.7	7.87	7.63	7.75	7.75
CaO	11.18	10.99	11.09	11.33	13.2	13.0	13.1	13.3	9.29	9.17	9.23	9.23
Na ₂ O	2.16	0.73	1.44	2.29	1.82	1.72	1.77	1.82	2.74	2.63	2.68	2.74
K ₂ O	0.55	-0.01	0.27	0.54	BDL	BDL	BDL	0.03	1.46	1.45	1.46	1.46
P ₂ O ₅	0.28	0.28	0.28	0.27	BDL	BDL	BDL	0.021	0.26	0.26	0.26	0.26
Totals:	99.06	96.87	97.96	100.53	100.86	99.84	100.35	100.756	98.53	98.67	98.60	98.66
Trace element (ppm):												
Ni	121	120	120	121	189	184	187	166	143	137	140	140
Cr	266	254	260	289	407	393	400	382	401	429	415	415
V	317	343	330	317	375	365	370	313	198	242	220	220
Zr	180	192	186	179	12	13	13	15.5	144	148	146	146
Sc	32	33	32	32	48	47	47	44	29	29	29	29
Y	30	29	30	28	13	16	15	16	28	20	24	24
Sr	382	389	385	403	107	107	107	108	441	445	443	443
Ba	133	135	134	139	5	6	6	7	565	429	497	497
Co	56	55	55	45	50	52	51	52	38.2	40.8	39.5	39.5
Cu	225	224	225	136	176	181	179	126	70.1	40.9	55.5	55.5
Zn	108	110	109	105	79	67	73	71	76	88	82	82

Notes: Values in italics indicate that the machine software crashed during the analysis of these elements. Iron is represented as Fe³⁺. BHVO-2 was used as the calibration standard. BDL = below detection limit.

Table T8. Abbreviations used in the alteration and vein logs.

Color		Primary and secondary minerals		Apparent vein orientation	
Color	Abbreviation	Mineral	Abbreviation	Orientation	Abbreviation
Black	Blk	Olivine	Ol	Inclined	i
White	Wht	Plagioclase	Pl	Curved	c
Brown	Brn	Pyroxene	Px	Horizontal	h
Yellow	Y	Calcium carbonate	CaCO ₃	Vertical	v
Gray	Gr	Iron oxyhydroxides	FeOx	Subhorizontal	sh
Red	R	Pyrite	Py	Subvertical	sv
Green	G	Clay	C		
Blue	Bl	Zeolite	Zeol		
Light	L	Chlorite	Chl		
Dark	Dk	Saponite	Sap		
		Celadonite	Cel		

Note: Other mineral names and colors are written out in full.

Table T9. Ages for normal polarity magnetic chrons, Leg 197.

Normal polarity interval (Ma)	Polarity chron	Normal polarity interval (Ma)	Polarity chron
0.000–0.780	C1n	22.588–22.750	C6Bn.1n
0.990–1.070	C1r.1n	22.804–23.069	C6Bn.2n
1.770–1.950	C2n	23.353–23.535	C6Cn.1n
2.140–2.150	C2r.1n	23.677–23.800	C6Cn.2n
2.581–3.040	C2An.1n	23.999–24.118	C6Cn.3n
3.110–3.220	C2An.2n	24.730–24.781	C7n.1n
3.330–3.580	C2An.3n	24.835–25.183	C7n.2n
4.180–4.290	C3n.1n	25.496–25.648	C7An
4.480–4.620	C3n.2n	25.823–25.951	C8n.1n
4.800–4.890	C3n.3n	25.992–26.554	C8n.2n
4.984–5.230	C3n.4n	27.027–27.972	C9n
5.894–6.137	C3An.1n	28.283–28.512	C10n.1n
6.269–6.567	C3An.2n	28.578–28.745	C10n.2n
6.935–7.091	C3Bn	29.041–29.662	C11n.1n
7.135–7.170	C3Br.1n	29.765–30.098	C11n.2n
7.341–7.375	C3Br.2n	30.479–30.939	C12n
7.432–7.562	C4n.1n	33.058–33.545	C13n
7.650–8.072	C4n.2n	34.655–34.940	C15n
8.225–8.257	C4r.1n	35.343–35.526	C16n.1n
8.699–9.025	C4An	35.685–36.341	C16n.2n
9.230–9.308	C4Ar.1n	36.618–37.473	C17n.1n
9.580–9.642	C4Ar.2n	37.604–37.848	C17n.2n
9.740–9.880	C5n.1n	37.920–38.113	C17n.3n
9.920–10.949	C5n.2n	38.426–39.552	C18n.1n
11.052–11.099	C5r.1n	39.631–40.130	C18n.2n
11.476–11.531	C5r.2n	41.257–41.521	C19n
11.935–12.078	C5An.1n	42.536–43.789	C20n
12.184–12.401	C5An.2n	46.264–47.906	C21n
12.678–12.708	C5Ar.1n	49.037–49.714	C22n
12.775–12.819	C5Ar.2n	50.778–50.946	C23n.1n
12.991–13.139	C5AAn	51.047–51.743	C23n.2n
13.302–13.510	C5ABn	52.364–52.663	C24n.1n
13.703–14.076	C5ACn	52.757–52.801	C24n.2n
14.178–14.612	C5ADn	52.903–53.347	C24n.3n
14.800–14.888	C5Bn.1n	55.904–56.391	C25n
15.034–15.155	C5Bn.2n	57.554–57.911	C26n
16.014–16.293	C5Cn.1n	60.920–61.276	C27n
16.327–16.488	C5Cn.2n	62.499–63.634	C28n
16.556–16.726	C5Cn.3n	63.976–64.745	C29n
17.277–17.615	C5Dn	65.578–67.610	C30n
18.281–18.781	C5En	67.735–68.737	C31n
19.048–20.131	C6n	71.071–71.338	C32n.1n
20.518–20.725	C6An.1n	71.587–73.004	C32n.2n
20.996–21.320	C6An.2n	73.291–73.374	C32r.1n
21.768–21.859	C6AAn	73.619–79.075	C33n
22.151–22.248	C6AAr.1n	83.000–118.000	C34n
22.459–22.493	C6AAr.2n		

Note: From Cande and Kent, 1995.

Table T10. Application, sampling interval, and vertical resolution of logging tools, Leg 197.

Tool string	Tool	Measurement	Sampling interval (cm)	Approximate vertical resolution (cm)
Triple combination	HNGS	Spectral gamma ray	15	51
	APS	Porosity	5 and 15	43
	HLDS/HLDT	Bulk density	2.5 and 15	38/46
	DLL	Resistivity	15	61
	TAP	Temperature	1 per s	NA
		Tool acceleration	4 per s	NA
		Pressure	1 per s	NA
Formation MicroScanner (FMS)/sonic combination	NGT	Spectral gamma ray	15	46
	GPIT	Tool orientation	0.25 and 15	NA
	FMS	Microresistivity	0.25	0.5
	DSI	Acoustic velocity	15	107

Notes: All tool and tool string names (except the TAP) are trademarks of Schlumberger. For additional information about tool physics and use consult ODP Logging Services at <http://www.ideo.columbia.edu/BRG/ODP>. HNGS = hostile environment natural gamma ray sonde, APS = accelerator porosity sonde, HLDS = hostile environment lithodensity sonde, HLDR = hostile environment lithodensity logging tool, DLL = dual laterolog, TAP = temperature/acceleration/pressure tool, NGT = natural gamma ray spectrometry tool, GPIT = general purpose inclinometer tool, FMS = Formation MicroScanner, DSI = dipole sonic imager. NA = not applicable.

Table T11. Acronyms and units used for wireline logging tools, Leg 197.

Tool	Output	Explanation	Units
APS		Accelerator porosity sonde	
	APLC	Near array porosity (limestone calibrated)	%
	SIGF	Formation capture cross section (Σ_f)	Capture units
	STOF	Tool standoff (computed distance from borehole wall)	in
DLL		Dual laterolog	
	LLD	Deep resistivity	Ω m
	LLS	Shallow resistivity	Ω m
DSI		Dipole sonic imager	
	DTCO	Compressional wave delay time (Δ_t)	ms/ft
	DTSM	Shear wave delay time (Δ_t)	ms/ft
	DTST	Stoneley wave delay time (Δ_t)	ms/ft
FMS		Formation MicroScanner	
	C1, C2	Orthogonal hole diameters	in
	P1AZ	Pad 1 azimuth	Degrees
		Spatially oriented resistivity images of borehole wall	
GPIT		General purpose inclinometer tool	
	DEVI	Hole deviation	Degrees
	HAZI	Hole azimuth	Degrees
	Fx, Fy, Fz	Earth's magnetic field (three orthogonal components)	Degrees
	Ax, Ay, Az	Acceleration (three orthogonal components)	m/s ²
HLDS		Hostile environment lithodensity sonde	
	RHOM	Bulk density	g/cm ³
	PEFL	Photoelectric effect	b/e ⁻
	LCAL	Caliper (measure of borehole diameter)	in
	DRH	Bulk density correction	g/cm ³
HNGS		Hostile environment gamma ray sonde	
	HSGR	Standard (total) gamma ray	gAPI
	HCGR	Computed gamma ray (HSGR minus uranium contribution)	gAPI
	HFK	Potassium	wt%
	HTHO	Thorium	ppm
	HURA	Uranium	ppm
NGT		Natural gamma ray spectrometry tool	
	SGR	Standard total gamma ray	gAPI
	CGR	Computed gamma ray (SGR minus uranium contribution)	gAPI
	POTA	Potassium	wt%
	THOR	Thorium	ppm
	URAN	Uranium	ppm
TAP		Temperature/acceleration/pressure tool	°C, m/s ² , psi

Table T12. Specifications of the Goettingen borehole magnetometer.

Component	Specification
Borehole magnetometer	Three-component fluxgate
Power supply	50 V/0.25 A (12 W)
Random walk of fluxgate sensors	<0.1 nT
Range	±50 µT
Resolution	6.1 nT
Data transmission	Digital two-wire Manchester encoded
Sample rate	Eight readings from 8 channels/s
Data acquisition system	Personal computer (DOS)
Tool weight	68 kg
Tool length	3.5 m
Tool diameter	86 mm (3.375 in)
Housing	Low magnetic monel
Nonmagnetic bronze centralizers (2)	16.3 kg each
Maximum operation temperature	0°–700°C (limited by FOG)
Maximum operation pressure	70 MPa
Recommended logging speed	360 m/hr
Maximum logging speed	3600 m/hr (limited by hole diameter)
Tool navigation system	Three FOG µFORS-36 m (LITEF)

Note: FOG = fiber-optic gyro, µFORS = miniature fiber-optic rate sensor.

Table T13. Specifications of the susceptibility tool SUSLOG 403-D.

Component	Specification
Measuring range	10 ⁻⁵ –0.2 SI
Range for measuring conductivity	0.01–10 S/m
Output voltage	0 to 10 V DC
Baud rate	2400 baud
Coil spacing	400 mm
Operating frequency	1000 Hz
Recommended logging speed	0.3–0.5 m/s
Power supply	12 V DC, 7.5 W, or 240 V AC
Number of conductors used in the wireline cable	Minimum 3 (2 for power, 1 for data transmission)
Length	2.5 m
Outer diameter	75 mm
Maximum operation temperature	600°C
Maximum pressure	40 MPa (400 bar)
Random walk and resolution	2 × 10 ⁻⁵ SI
Data transmission	Digital
Sample rate	5 cm
Tool weight	~25 kg
Vertical resolution	40 cm

Note: DC = direct current, AC = alternating current.